Modelling of Polymer Seal Strength: Response Surface Methodology Approach

by

Ivan van Jaarsveld

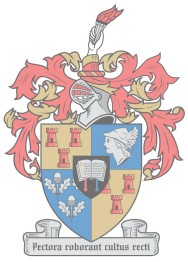

Thesis presented in partial fulfilment of the requirements for the degree of Master of Engineering (Mechanical) in the Faculty of Engineering at Stellenbosch University

Supervisor: Dr M.P. Venter

March 2018

Declaration

By submitting this thesis electronically, I declare that the entirety of the work contained therein is my own, original work, that I am the sole author thereof (save to the extent explicitly otherwise stated), that reproduction and publication thereof by Stellenbosch University will not infringe any third party rights and that I have not previously in its entirety or in part submitted it for obtaining any qualification.

Date: March 2018

UNIVERSITEIT·STELLENBOSCH·UNIVERSITY
jou kennisvennoot • your knowledge partner

Plagiaatverklaring / Plagiarism *Declaration*

1 Plagiaat is die oorneem en gebruik van die idees, materiaal en ander intellektuele eiendom van ander persone asof dit jou eie werk is.
Plagiarism is the use of ideas, material and other intellectual property of another's work and to present is as my own.

2 Ek erken dat die pleeg van plagiaat 'n strafbare oortreding is aangesien dit 'n vorm van diefstal is.
I agree that plagiarism is a punishable offence because it constitutes theft.

3 Ek verstaan ook dat direkte vertalings plagiaat is.
I also understand that direct translations are plagiarism.

4 Dienooreenkomstig is alle aanhalings en bydraes vanuit enige bron (ingesluit die internet) volledig verwys (erken). Ek erken dat die woordelikse aanhaal van teks sonder aanhalingstekens (selfs al word die bron volledig erken) plagiaat is.
Accordingly all quotations and contributions from any source whatsoever (including the internet) have been cited fully. I understand that the reproduction of text without quotation marks (even when the source is cited) is plagiarism.

5 Ek verklaar dat die werk in hierdie skryfstuk vervat, behalwe waar anders aangedui, my eie oorspronklike werk is en dat ek dit nie vantevore in die geheel of gedeeltelik ingehandig het vir bepunting in hierdie module/werkstuk of 'n ander module/werkstuk nie.
I declare that the work contained in this assignment, except where otherwise stated, is my original work and that I have not previously (in its entirety or in part) submitted it for grading in this module/assignment or another module/assignment.

Studentenommer / *Student number*	**Handtekening / *Signature***
Voorletters en van / *Initials and surname*	**Datum / *Date***

Abstract

Modelling of Polymer Seal Strength: Response Surface Methodology Approach

I. van Jaarsveld

Department of Mechanical and Mechatronic Engineering,
University of Stellenbosch,
Private Bag X1, Matieland 7602, South Africa.

Thesis: MEng (Mech)

March 2018

The response surface methodology (RSM) approach was followed to construct a predictive model concerning the seal strength between film to gland fitments. The proposed method provides a replacement for the current trial and error approach followed by the industry partner. With the new approach, the manufacturer can tailor specific solutions to comply with changing requirements, allowing them to adapt in limited time to manufacture gland seals that comply with specific requirements. The final constructed model was able to account for 90 % of the total observed variance of the training set, 3.6 % of the 10 % unaccounted variance was due to lack of fit, and 6.4 % was due to the variability between replicates. Independent validation tests were conducted to verify the use of the model. The predicted optimum corresponded to a seal strength of 21.9 MPa, and process variables of temperature = 320 °C, pressure = 4.4 bar and dwell time = 5.5 sec. The results obtained were within the constructed 95 % confidence interval, and the mean approximated the true response. As a result, the model accounted for 89 % of the observed variance of the validation set.

Uittreksel

Modellering van Polimeerseëlsterkte: 'n Reaksievlakmetodologie Benadering

I. van Jaarsveld

Departement van Meganiese en Megatroniese Ingenieurswese,
Universiteit van Stellenbosch,
Privaatsak X1, Matieland 7602, Suid Afrika.

Tesis: MIng (Meg)

Maart 2018

Die reaksievlakmetodologie (RVM) benadering is gevolg om statistiese modelle te genereer met betrekking tot die seëlsterkte tussen film en plastiese klierpassings. Die prosedures gevolg in hierdie projek word voorgestel aan die bedryfs vennoot om hul huidige benadering te vervang. Met die nuwe benadering kan die vervaardiger spesifieke oplossings vind wat voldoen aan vereistes wat moontlik kan verander. Dit sal hul toelaat om in 'n beperkte tydperk te reageer en voldoende seëls te vervaardig. Die finale model kon 90 % van die totale variasie verklaar; 3.6 % van die ongedefinieerde 10 % was die gevolg van modelpassing en 6.4 % was as gevolg van die geraas tussen opeenvolgende toetse. Die model het voorgestel dat die proses optimum 'n seëlsterkte van $21,9$ MPa sal hê vir die vervaardigingsveranderlikes van temperatuur = 320 °C, druk = 4.4 bar en verwerkingstyd = 5.5 sek. Onafhanklike validiteitstoetse is uitgevoer om die gebruik van die model te verifieer. Die resultate was binne die 95 % sekerheidsinterval, en die gemiddelde hiervan het die ware reaksie weerspieël. Die model het dus 89 % van die totale variasie van die onafhanklike validiteitstoetse verklaar.

Acknowledgements

I would like to thank our Lord Jesus Christ for He has brought me from death into life. His protection and grace surround me, and without Him, I will merely be dry bones. John 14:6 - Jesus answered, "I am the way and the truth and the life. No one comes to the Father except through me."

All of my family and friends have been of great support to me and I am thankful for them all. Then, I would like to thank Dr M.P. Venter for his supervision and guidance concerning this project and finally, Anderson Lid Company for funding the project.

Contents

List of Figures

List of Tables

Chapter 1

Introduction

1.1 Introduction to Liquid Liners

Liquid liners are gaining popularity over rigid containers for transporting bulk liquids in the food packaging industry. According to Anderson Lid Company (ALC), the transporting cost involved with rigid containers is double the expense of using liquid liners, since rigid containers require extensive cleaning before being reused in the next transporting cycle. Liquid liners are placed in intermediate bulk containers (IBCs) during transportation. The liners are disposed of after use, while the IBCs are collapsed and sent back to the local pool for reuse. This eliminates the extensive cleaning cost involved with rigid containers. The IBCs provide structural support for the liquid liners during transportation. Upon filling, the liners expand into the form of the container. This is displayed in Fig. 1.1, where Fig. 1.1a shows a filled liner, and Fig. 1.1b displays a liner being filled in an IBC.

Different bag layouts can be tailored to accommodate different applications. The deciding factors include fluid viscosity and film permeability requirements. Emptying viscous fluids from liners are notoriously difficult. To ease this process, ALC makes use of bladder bags. The bladder squeezes the liquid product out when inflated with air, which reduces the product residual.

Siracusa (2012) presented a review article concerning food packaging permeability behaviour. The article states that the degree of permeation is controlled to preserve the aroma and flavour, and also to extend the shelf life of the food content. ALC also considers the permeability requirements for each product application and specifies the adequate liner design for the customer.

It is important to ensure that the liners are capable of withstanding transport abuse. Since failure normally occurs at the seal interface of the film to gland fitment, the manufacturer is concerned with producing high-quality seals. The seals are produced with a sealing heat head. The head is actuated at a given pressure, temperature and dwell time. These variables can be altered to achieve the adequate seal strength for different product layouts. However,

ALC follows a trial and error approach at this stage to obtain the adequate process variables, where multiple gland seals are produced before the adequate process variables are obtained to achieve the minimum required seal strength of 15 MPa. Although this approach can be easily applied, it does not provide insight into the influence a variety of variables has on the sealing strength. Also, it is not regarded as robust technique. As a result, ALC has set out a research project to address this problem.

(a) Expanded Liner (b) Liner in IBC

Figure 1.1: The figure respectively displays a liquid liner, Fig. 1.1a and IBC with inserted liquid liner, Fig. 1.1b. The liner is filled at the top through the gland fitment, see Fig. 1.1b, where the liner expands into the form of the IBC upon filling.

1.2 Project Description

A research project was proposed to Anderson Lid Company (ALC) to characterise the film to gland sealing process. Currently, the manufacturer goes through a tedious process of altering the process variables until an adequate seal strength of 15 MPa is achieved. A proposal for replacing the current trial and error approach is required, where the nature of the solution should provide the adequate process variables to produce high strength seals. The research project is set out to establish a predictive model consisting of the significant variables at play, which is able to predict the seal strength accordingly. This will provide the manufacturer with the adequate process conditions to produce gland seals complying with the company's requirements without going through a tedious process.

1.3 Project Objectives

Three main objectives were identified based on the project requirements. Firstly a summary of each is given and then a description of each is provided in the proceeding subsections.

- Establish the significant variables.
- Predict sealing envelope.
- Predict adequate process variables that will result in high strength seals, exceeding 15 MPa.

1.3.1 Establish Significant Parameters

The sealing process can be influenced by a number of variables. Some are obvious, e.g. the process variables, which are the heat head temperature, dwell time and pneumatic pressure. However, additional variables might exist that significantly influence the seal strength. The first objective only seeks to find the most significant variables at play.

1.3.2 Predict Sealing Envelope

The sealing envelope represents the response of the seal strength based upon the significant variables at play. The constructed response curve should approximate the true response of the system. This can be represented by a model equation that describes the seal strength based upon the significant variables, within the define space of process variables. The sealing envelope captures the main effects of the significant variables. These effects may be linear, non-linear or even a combination of both.

1.3.3 Predict Optimised Process Parameters

From practice, ALC has discovered that weak seals result at the extreme ends of the process variables. The process variables include the heat head temperature, actuated pneumatic pressure of the head and process dwell time. This indicates that higher order terms will be present in the model; as a result, an optimum exists. Once the sealing envelope is known, an optimum within the given boundaries can be obtained. The optimum seal strength can then be related back to the process variables through the model, which can be used during production.

Chapter 2

Literature Study

This chapter will cover a literature study on polymer characteristics, in particular, the behaviour of semicrystalline polymers. This information will provide insight into the mechanical behaviour of the materials used during the course of this project. Since the material's micro properties relate to the mechanical behaviour of the polymer, the appropriate polymer science topics will be discussed followed by a discussion on the mechanical behaviour of semicrystalline polymers, in particular, the uniaxial response.

2.1 Background on Polymers

The word polymer indicates that a substance's molecular structure consists of multiple repeat units, called monomers. The molecules of polymers tend to be long; as a result, polymers have a high molecular weight (Sperling, 2005, p. 1). A few examples of such substances are proteins, cotton, starch and, for the interest of this document, plastics, in particular polyethylene. Polyethylene's chemical structure consists of ethylene monomers, which is a hydrocarbon molecule that has a structure of, $CH_2 = CH_2$ (Sperling, 2005, p. 3). These units are repeated in the thousands to form polyethylene. Polyethylene has no side groups and can typically contain 1000 to 3000 carbon atoms (Sperling, 2005, p. 3).

2.1.1 Molecular Weight and Molecular Weight Distribution

The molecular weight distribution (MWD) of polymers are sensitive to the kinetics of polymerisation. Consequently, the MWD can vary significantly in a single polymer sample (Sperling, 2005, p. 7). This means that polymers are polydisperse, where a single sample contains a distribution of chain lengths, or species (Sperling, 2005, p. 72).

Kretschmer *et al.* (2006) have studied the influence of polymerisation kinetics on the MWD, among which was the temperature dependency of the polymerisation of organoyttrium-catalysed ethylene. The effect of four temperatures was investigated. These were 30 °C, 50 °C, 80 °C and 100 °C where the respective molecular weights obtained were 67 900 g.mol^{-1}, 76 400 g.mol^{-1}, 66 500 g.mol^{-1} and 15 600 g.mol^{-1}. The polydispersity indexes thereof were 43, 19.1, 3.2 and 4.4. These results are displayed in Fig. 2.1, where the molecular weight distributions obtained for each temperature are plotted. The variance between the results indicates that the molecular weight and distribution thereof are sensitive to the kinetics of polymerisation, although all distributions are of polyethylene; this confirms with Sperling (2005).

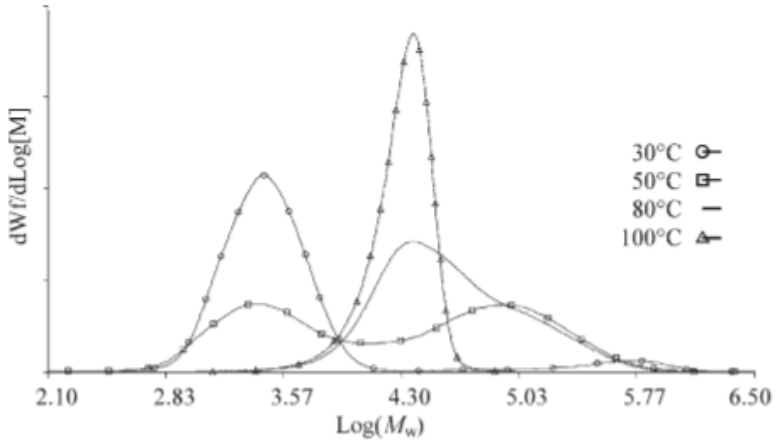

Figure 2.1: Molecular weight distribution dependency on temperature of organoyttrium-catalysed ethylene polymerisation (Kretschmer *et al.*, 2006, p. 8972, Fig. 3).

2.1.2 Semicrystalline State

Polyethylene is regarded as a tough plastic (Sperling, 2005, p. 4). It is a semicrystalline material where polymer chains are able to fold onto one another to form lamellae crystallites and disordered amorphous regions between crystallites (Sperling, 2005, p. 4). The long chains entangle in the amorphous state and this imparts strength in the material when stressed (Sperling, 2005, p. 4). Since polyethylene is isostatic, meaning that the molecules consist of stereochemical configurations, it is able to crystallise (Sperling, 2005, p. 239). However, since the molecules are long, they tend to entangle and thus form the disordered amorphous regions. One of the simplest models to illustrate a semicrystalline polymer is the Fringed Micelle model. This schematic representation is depicted in Fig. 2.2, where disordered amorphous state and ordered crystallites can be clearly distinguished.

Figure 2.2: Disorder and ordered regions respectively represent the crystallites and amorphous regions illustrated by the Fringed Micelle model (Sperling, 2005, p. 257, Fig. 6.9).

2.1.3 Melting and Crystallisation

The melting process of semicrystalline material is a first order transition (Sperling, 2005, p. 299). When the crystallites are melted, the resulted melt becomes amorphous. The melting temperature of polymers is dependant on its molecule weight; for most linear polyethylenes melting temperature is close to $T_f = 140\,°C$ (Sperling, 2005, p. 3).

Early studies such as Chiang and Flory (1961), have looked at crystallisation and melting of linear polyethylenes. Crystallisation can be achieved by under-cooling the material from the melt. Under-cooling constitutes the temperature difference between the fusion temperature, or melting temperature (T_f) and cooling temperature (Chiang and Flory, 1961, p. 2850). As the under-cooling increases the rate of crystallisation increases. However, since the molecular motions become sluggish at lower temperatures, a limit exists to which the crystallisation rate can be increased (Sperling, 2005, p. 274). The kinetics of crystallisation are then driven by the temperature gradient of cooling and are limited by molecular motion.

Chiang and Flory (1961) prepared polyethylene samples which were crystallised at, 131.3 °C, and studied the melting transition thereof. The first order transition of melt obtained by Chiang and Flory (1961) of high molecular weight polyethylene is displayed in Fig. 2.3. The graph displays the specific volume change as the temperature increases. At just below 140 °C a sudden change in specific volume is observed; this is described by Chiang and Flory (1961) as the melting temperature. Therefore, the melting temperature obtained was, $T_f = 138.5\,°C$. This value is just below what Sperling (2005) suggested as the theoretical maximum melting temperature of polyethylene, being 145 °C. It is also important to note that melting has started at 118 °C and completed melt was obtained at $T_f = 138.5\,°C$. The transition of melting occurs due to polydispersity since different species melt at different temperatures.

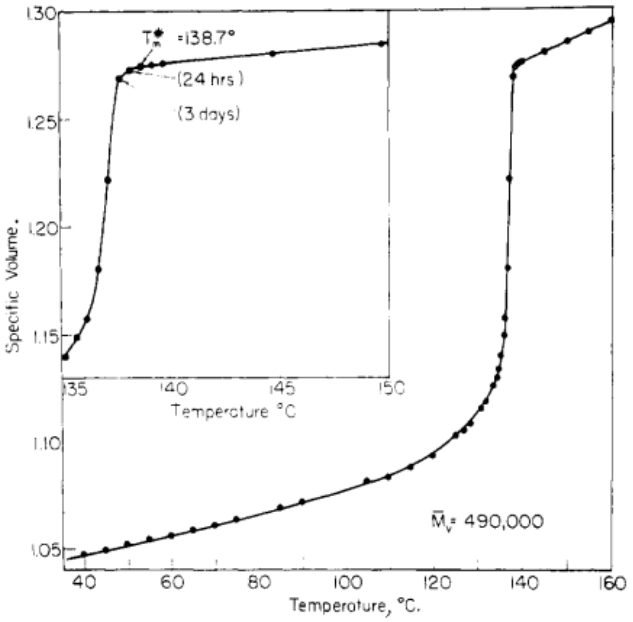

Figure 2.3: First order melt of crystallites of polyethylene (Chiang and Flory, 1961, p. 2860, Fig. 1).

2.1.4 Viscoelasticity: Glass-Rubber Transition

Since semicrystalline materials consist of a dispersion of amorphous and crystalline regions, intriguing behavioural properties can be observed. These are stress relaxation, creep, and glass-rubber transitional behaviour. Viscoelasticity is the combined effect of elastic and viscous behaviour (Sperling, 2005, p. 507). In semicrystalline polymers, the crystalline and amorphous regions are respectively responsible for the elastic and viscous properties. Creep is a phenomenon when a material extends over a period of time while being held at a constant load (Sperling, 2005, p. 507). Stress relaxation, however, is when a specimen is stretched to a constant length and the required stress to keep the deformation constant decreases over time (Sperling, 2005, p. 507).

The stiffness of semicrystalline materials is time and temperature dependent. This means Young's modulus of a semicrystalline polymer is a function of time and temperature (Sperling, 2005, p. 349). Fig. 2.4 shows a generalised modulus-temperature master curve of a semicrystalline material (Sperling, 2005, p. 8). This transitional behaviour is known as the glass-rubber transition.

Sperling (2005) provides five regions of viscoelasticity. These are the glassy region, glass transition region, rubber plateau region, rubber flow region and liquid flow region. These were subsequently numbered accordingly in Fig. 2.4. For low-temperature values, in the glassy region, the material is brittle.

Although not displayed in this schematic, Young's modulus is fairly constant for temperature values lower than point one (Sperling, 2005, p. 356).

At point two, during the glass transition process, the material starts to soften as the temperature increases. This transition starts to occur at the glass transition temperature, $T = T_g$. Polyethylene has a glass transition temperature of, $T_g = -80\,^{\circ}\mathrm{C}$ (Sperling, 2005, p. 239). At this point, the material becomes leathery in behaviour and is highly sensitive to temperature change. Typically the modulus can drop by a factor of 1000, before reaching point three, in the viscoelastic region, where $T_g < T < T_f$ (Sperling, 2005, p. 358).

The next region is defined as the rubbery plateau region; this is between point three and four. Here the modulus stays fairly constant over the temperature range. The width of this region is governed by the molecular weight of the material, where longer molecular chains will result in a longer plateau region (Sperling, 2005, p. 259). Sperling (2005) defines the material to behave highly elastic in this region. Some of the chains start to flow, and a transition occurs at point four. Total flow is achieved when the temperature value exceeds point five and thus the whole material is now melted.

Although not provided, the time effect on the modulus is indirectly proportional to what the temperature effect is. This means that the relationship between time and modulus are an inversion of the graph provided in Fig. 2.4, e.g. high temperatures and low time periods will have a similar effect on the modulus response curve.

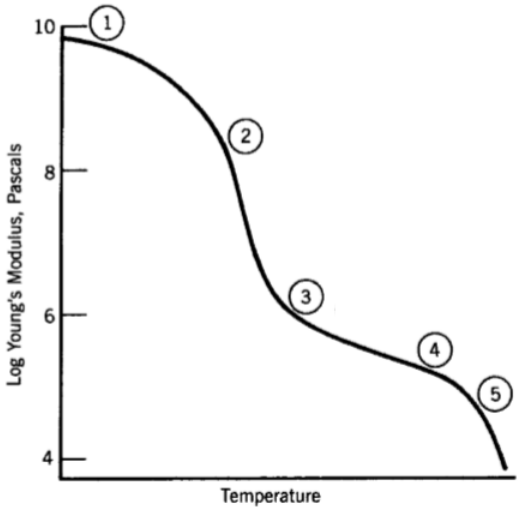

Figure 2.4: General modulus temperature dependency of semicrystalline polymer (Sperling, 2005, p. 8).

2.2 Polymer Mechanical Behaviour: Uniaxial Response

This section discusses the mechanical properties of polymers, in particular, studying their tensile properties. These are Young's modulus, yielding, cold drawing and failure. The study will also include the variables that affect these properties in general.

2.2.1 Time Temperature Dependency of Modulus

As discussed in the previous section, the modulus of polymers is time and temperature dependent. This is especially the case when working with polymers in the viscoelastic region where the material's temperature is, $T_g < T < T_f$. The ambient conditions for polyethylene are always well within this region, where $T_g = -80\,°\text{C}$, and $T_f = 138.5\,°\text{C}$. This implies that the material's modulus is highly sensitive to temperature change and draw rate.

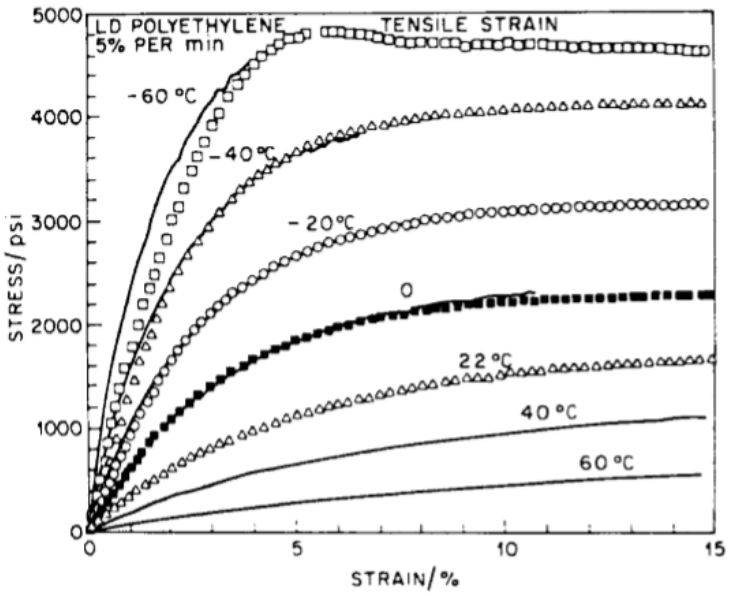

Figure 2.5: Temperature effect on modulus of low density polyethylene (LDP) at 5 %/min strain rate (Sperling, 2005, p. 568, Fig. 11.7).

Sperling (2005) provides a temperature dependency study on uniaxial tests of low-density polyethylene. The strain rate was constantly kept at 5 %/min, and the draw temperature was varied to study the effect thereof on Young's modulus. The tensile test results are displayed in Fig. 2.5. Recall that Young's modulus is obtained by the gradient in the linear elastic region of a stress-strain curve. Then, one can observe from Fig. 2.5 that the elastic modulus

reduces greatly as the temperature increases. This complies with Fig. 2.4 where the modulus reduces between points two and three with an increase in temperature.

2.2.2 Anisotropic Behaviour: Modulus

An anisotropic material has different properties in different material directions (Landel and Nielsen, 1993, p. 34). A few examples of these materials are, oriented amorphous polymers, injection moulded parts, fibre-filled composites, single crystals and crystalline polymers (Landel and Nielsen, 1993, p. 34).

Manufacturing processes can dictate the crystallisation direction of polymers, which can induce anisotropic material properties, e.g. polyethylene films are blown from the melt, which crystallises in the blow direction. As a result, the crystallites are predominately aligned with the blow direction, which induces anisotropic material properties. The highly aligned crystals provide a plane of symmetry, which becomes a special case of anisotropy, being orthotropic or transversely isotropic (Ward and Hadley, 1993, p. 112).

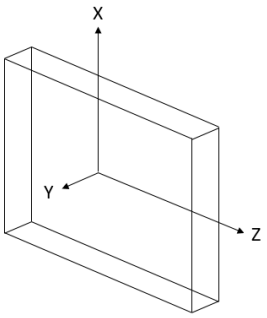

Figure 2.6: Orthotropic axes definition for polymer films (Ward and Hadley, 1993, p. 567, Fig. 7.2).

Ward and Hadley (1993) provided the conditioning of the compliance matrix of an orthotropic material, which will be provided in the following discussion where Fig. 2.6 provides the defined axes. The z-axis is in the machine direction or blow direction, the x-axis lies in-plane orthogonal with the z-axis, and the y-axis is normal to the plane. Hooke's law describes the stress-strain response in the linear elastic region (Ward and Hadley, 1993, p. 110):

$$\sigma = E\,\epsilon \tag{2.1}$$

where σ is the uniaxial stress, E is Young's Modulus and ϵ is the strain. Then for convenience, the elastic compliance is defined as (Ward and Hadley, 1993, p. 110):

$$S_{jj} = 1/E_j, \tag{2.2}$$

for entries j=1,2,3. The shear compliance is defined by:

$$S_{jj} = 1/G_{j-3}, \tag{2.3}$$

for entries $j = 4, 5, 6$, e.g $S_{55} = 1/G_2$. The following compliance matrix can be constructed for orthotropic materials (Ward and Hadley, 1993, p. 111):

$$S_{pq} = \begin{bmatrix} S_{11} & S_{12} & S_{13} & 0 & 0 & 0 \\ S_{12} & S_{22} & S_{13} & 0 & 0 & 0 \\ S_{13} & S_{13} & S_{33} & 0 & 0 & 0 \\ 0 & 0 & 0 & S_{44} & 0 & 0 \\ 0 & 0 & 0 & 0 & S_{55} & 0 \\ 0 & 0 & 0 & 0 & 0 & 2(S_{11} - S_{12}) \end{bmatrix} \tag{2.4}$$

where the subscripts 1, 2 and 3, refer respectively to axes y, x and z. Poison's ratio is obtained by, $\nu_{ij} = -S_{ij}/S_{jj}$ and $S_{ij} = S_{ji}$. Also, $S_{55} = S_{44}$, $S_{22} = S_{11}$ and $S_{66} = 2(S_{11} - S_{12})$. Ward and Hadley (1993) provide an approach to characterise the compliance matrix by testing samples cut at 0°, 45° and 90° from the machine direction, z. Then the following relationships, in addition with Poison's relationship, can be used to characterise the compliance matrix (Ward and Hadley, 1993, p. 114):

$$E_0 = \frac{1}{S_{33}}, \quad E_{90} = \frac{1}{S_{11}}, \quad \textit{and} \quad \frac{1}{E_{45}} = \frac{1}{4}[S_{11} + S_{33} + (2S_{13} + S_{55})]. \tag{2.5}$$

Early studies of Raumann and Saunders (1961) have looked at Young's modulus at different material directions for anisotropic polymers. Uniaxially stretched isotropic sheets of low density polyethylene were prepared, samples were cut at different material directions and tested at room temperature (Raumann and Saunders, 1961). From this Raumann and Saunders (1961) constructed the compliance matrix and calculated the modulus in different material directions with (Raumann and Saunders, 1961):

$$S_\theta = S_{11}\sin^4\theta + S_{33}\cos^4\theta + (2S_{13} + S_{44})\sin^2\theta\cos^2\theta. \tag{2.6}$$

The results are displayed in Fig. 2.7. The tested and calculated modulus correlates well with the change in material direction, thus approving the compliance equation for transverse isotropic material.

Ward and Hadley (1993) have considered three possible interpretations concerning mechanical anisotropy. These are the molecular chain and crystal structure, the molecular orientation and morphology in a crystal structure, and lastly the thermally activated relaxation processes in both crystal and amorphous regions (Ward and Hadley, 1993, p. 126). A discussion of each will follow.

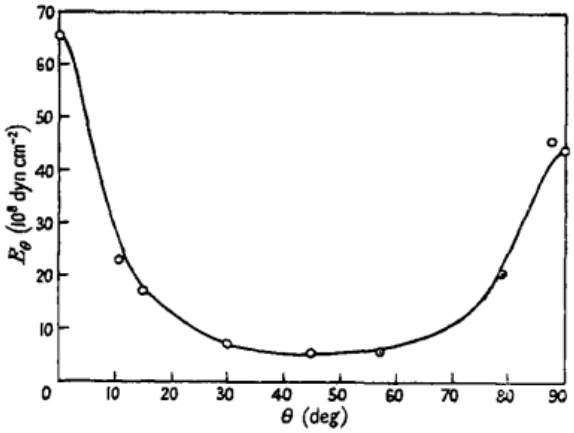

Figure 2.7: Comparison between calculated and observed modulus for an anisotropic polymer, obtained from (Raumann and Saunders, 1961, p. 1033, Fig. 1).

Polyethylene molecules are able to take a planar zigzag form when they crystallise. This is mainly possible due to the small hydrogen side groups of the molecule chain (Ward and Hadley, 1993, p. 126). This is schematically depicted in Fig. 2.8, where the backbone structure consists of carbon atoms. Anisotropy behaviour arises due to chain direction (Ward and Hadley, 1993, p. 126). When axially loaded, the crystals are stiff since covalent bending and stretching are involved. However, the stiffness decreases perpendicularly to chain direction, since only van der Waals forces are active. The effect of this can be clearly seen in the study of Tashiro *et al.* (1978).

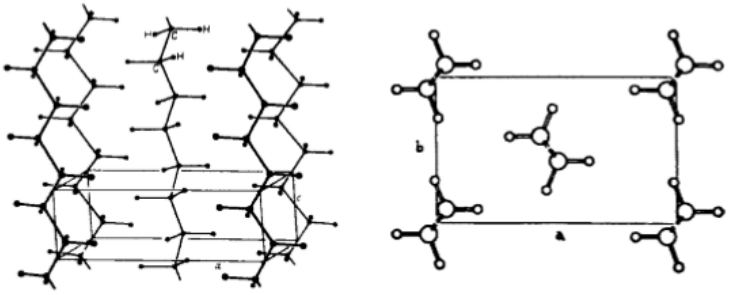

Figure 2.8: Planar zigzag structure of polyethylene crystal (Sperling, 2005, p. 8, Fig. 6.5). The illustration on the right is a top view of the crystal structure.

Tashiro *et al.* (1978) has shown three dimensional elastic constants estimation of polyethylene by means of eq. 2.4 and eq. 2.5. The results have led to the compliance matrix provided in eq. 2.7 (Tashiro *et al.*, 1978, p. 913). Recall eq.

2.5 that $E_0 = {S_{33}}^{-1}$ and $E_{90} = {S_{11}}^{-1}$, then $E_0 \simeq 315\,\text{GPa}$ and $E_{90} \simeq 7\,\text{GPa}$. These results comply with what Ward and Hadley (1993) suggested that the axial stiffness E_0 is significantly larger then the perpendicular stiffness E_{90} due to the molecular planar zigzag alignment of polyethylene provided in Fig. 2.8.

$$S_{pq} = \begin{bmatrix} 14.5 & -4.78 & -0.019 & 0 & 0 & 0 \\ -4.78 & 11.7 & -0.062 & 0 & 0 & 0 \\ -0.019 & -0.062 & 0.317 & 0 & 0 & 0 \\ 0 & 0 & 0 & 31.4 & 0 & 0 \\ 0 & 0 & 0 & 0 & 61.7 & 0 \\ 0 & 0 & 0 & 0 & 0 & 27.6 \end{bmatrix} \times 100\ \text{GPa}^{-1} \quad (2.7)$$

However, since semicrystalline polymers consist of a dispersion of amorphous and crystalline regions (see Fig. 2.2), the mechanical anisotropy is less than expected, especially along the axial direction (Ward and Hadley, 1993, p. 128). Because of the alternating regions of amorphous and crystalline phases, where the molecules in the amorphous regions are randomly orientated, less stiffness in the axial direction is achieved, since less covalent bending and stretching is present (Ward and Hadley, 1993, p. 128). Thus the morphology plays a vital role as Ward and Hadley (1993) suggest.

Thermal relaxation is another cause of mechanical anisotropy as discussed by Ward and Hadley (1993). This occurs mainly due to the viscoelastic behaviour of semicrystalline polymers (Ward and Hadley, 1993, p. 128). Since creep and stress relaxation is an ongoing process, rearranging of molecules occurs continually. As a result, the stiffness changes.

Ward and Hadley (1993) have also looked at the development of a uniform stress model, assuming aggregates are in series, and a uniform strain model, assuming aggregates are in parallel (Ward and Hadley, 1993, p. 130). The measured results proved to be between the extreme bounds predicted by the series aggregate and parallel aggregate models, implying that true systems are a combination of both (Ward and Hadley, 1993, p. 131). By adding an optical property such as birefringence to the model, an estimation of the true aggregate layout can be achieved, resulting in accurate results (Ward and Hadley, 1993, p. 133). Birefringence is an optical property, which depends on the propagation of light through a medium and reflection thereof. This property provides insight into the molecular arrangement of a semicrystalline polymer (Ward and Hadley, 1993, p. 133).

2.2.3 Yielding and Cold Drawing of Polymers

Yielding of polymers is temperature and strain rate dependent, as seen from the previous sections on viscoelasticity (Ward and Hadley, 1993, p. 212) and Fig. 2.5. Polymers can exhibit four main types of responses during uniaxial loading; see Fig. 2.9. These are brittle fracture, ductile failure, necking and

cold drawing, and homogeneous deformation, which is also referred as quasi-rubber-like behaviour (Ward and Hadley, 1993, p. 246).

For the respective responses, Young's modulus and yielding values decrease as the temperature increases. These responses respectively comply with the mechanical regions outlined in Fig. 2.4 as described by section 2.1.4. The proceeding discussion will focus on ductile behaviour with necking and cold drawing, as depicted in Fig. 2.9 (c). This response complies with semicrystalline polymers where the amorphous state is above the glass transition temperature, $T > T_g$ (Sperling, 2005, p. 569).

Richeton *et al.* (2006) have studied the effect of temperature and strain rate on the mechanical properties of three amorphous polymers. These were, polycarbonate (PC), polymethyl methacrylate (PMMA), and polyamide-imide (PAI). The temperature range for the experiments was set from $-40\,^{\circ}\mathrm{C}$ to $180\,^{\circ}\mathrm{C}$, and the strain rate was set from $0.0001\,\mathrm{s}^{-1}$ to $5000\,\mathrm{s}^{-1}$. Richeton *et al.* (2006) have found that Young's modulus and the yield stress of each polymer decrease as the temperature increases. However, Young's modulus and the yield stress increase as the strain rate increases. These results comply with what was discussed before.

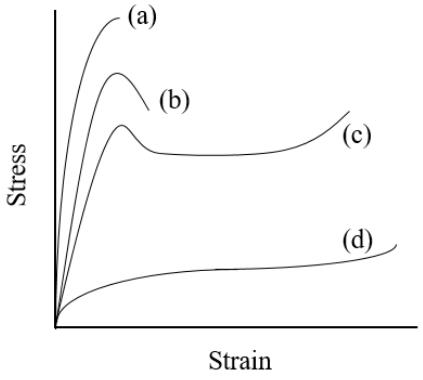

Figure 2.9: Semicrystalline polymer responses to axial loading (Ward and Hadley, 1993, p. 246, Fig. 12.1). These are (a) Brittle behaviour, (b) ductile behaviour, (c) necking and cold drawing, and (d) rubber-like behaviour. The temperature increases for consecutive responses and strain rate are kept constant. Responses (b) to (d) are above T_g.

2.2.4 Yield Stress Definitions and Necking

Yielding is defined as the minimum stress at which permanent deformation occurs (Ward and Hadley, 1993, p. 221). The exact yield point can be somewhat obscure for polymers, therefore a variety of yield stress definitions exist. Ward and Hadley (1993) provide three of these definitions which are outlined in Fig. 2.10.

The upper yield point is depicted in Fig 2.10a as point A, which is the peak before the onset of necking occurs during uniaxial tensile testing (Ward and Hadley, 1993, p. 221). From Fig 2.10b, the yield is defined by the intersection of two tangent lines as shown by point B (Ward and Hadley, 1993, p. 221). Another definition of the yield is depicted in Fig. 2.10c. A construction line with an offset of 2 % is drawn parallel with the elastic region. The intersection with the response curve depicted by point C becomes the proof strength (Ward and Hadley, 1993, p. 221).

The onset of necking occurs when the cross sectional area of the specimen decreases with increasing extension (Ward and Hadley, 1993, p. 215). This is visually observed in Fig. 2.10a, where the engineering stress decreases with increasing strain after the linear elastic region.

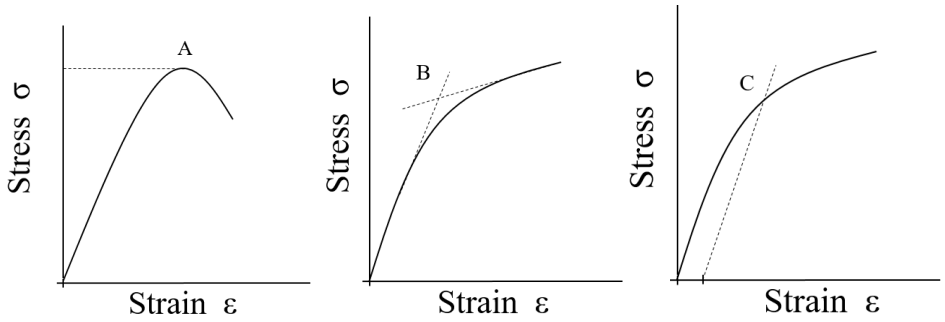

(a) Upper Yield Point (b) Intersection Yield (c) Proof Stress

Figure 2.10: Definitions of the yield stress are illustrated(Ward and Hadley, 1993, p. 221, Fig. 11.8). The three consecutive definitions outlined are the upper yield stress, tangent intersect yield and proof stress.

2.2.5 Cold Drawing

After the neck has stabilised, cold drawing starts to occur where molecule chains are aligned and elongated in the neck region. The realignment occurs in the stretching direction (Sperling, 2005, p. 569); see Fig 2.11, which causes the drawing stress to increase and crystallisation to occur (Ward and Hadley, 1993, p. 242). As a result, strain hardening occurs and a second linear response is observed beyond point C in Fig. 2.12.

Orthotropic polymers will undergo more stretching in the cross direction than in the machine direction since more molecules have to realign before failure can occur. The Van der Waals forces associated with the cross direction are much weaker than the covalent bonds predominately in the machine direction. As a result realignment of the molecule chains occurs when the load exceeds the Van der Waals forces; see Fig. 2.11. Once alignment becomes saturated the loading is predominantly on the covalent bonds; when exceeded, the material fails.

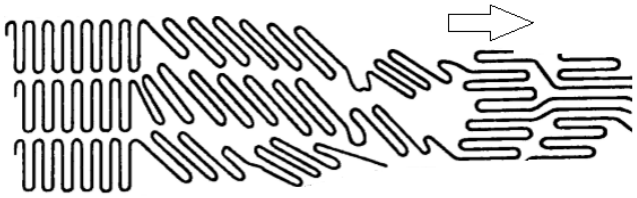

Figure 2.11: The mechanism for chain alignment during cold drawing (Sperling, 2005, p. 570, Fig. 11.8). The arrow indicates the direction of stretch where crystals break and reorder in the direction of stretch.

2.2.6 Considère's Construction

The following section discusses Considère's construction provided by Ward and Hadley (1993), which is an analytical method to obtain the yield point and stiffening point of uniaxial tensile results for polymers. Firstly, engineering stress is defined as the tensile load divided by the initial cross sectional area during tensile testing (Ward and Hadley, 1993, p. 215). This is:

$$\sigma_e = P\,/A_0 \tag{2.8}$$

where P is the uniaxial load and A_0 is the initial cross sectional area. However, the cross sectional area changes during a tensile test, thus the true stress is defined as the load divided by the actual cross section at any time period (Ward and Hadley, 1993, p. 215). This is:

$$\sigma_a = P\,/A \tag{2.9}$$

where A is the actual cross sectional area. Although the actual cross sectional area is difficult to measure during testing, a numerical approximation exists that relates engineering stress to true stress. Firstly, it is assumed that deformation takes place at a constant volume during plastic deformation (Ward and Hadley, 1993, p. 216); this is:

$$A\,l = A_0\,l_0 \tag{2.10}$$

where l and l_0 are respectively the actual and initial sample length. Also:

$$l = l_0 + \Delta\,l \tag{2.11}$$

and engineering strain is defined as

$$\epsilon = \Delta\,l/l_0 \tag{2.12}$$

where $\Delta\,l$ is the change in specimen length due to loading, and ϵ is the engineering strain during uniaxial loading (Ward and Hadley, 1993, p. 216). Then e.q. 2.10 becomes (Ward and Hadley, 1993, p. 215):

$$A = \frac{A_0\,l_0}{l} = \frac{A_0\,l_0}{l_0 + \Delta\,l} = \frac{A_0}{1+\epsilon}. \tag{2.13}$$

From eq. 2.9 and eq. 2.13 the true stress can be related to the engineering stress (Ward and Hadley, 1993, p. 215) as:

$$\sigma_a = \frac{P}{A} = \frac{(1+\epsilon)\,P}{A_0} = (1+\epsilon)\,\sigma_e. \tag{2.14}$$

For a turning point $\mathrm{d}P/\mathrm{d}\epsilon = 0$, thus:

$$\frac{\mathrm{d}P}{\mathrm{d}\epsilon} = \frac{A_0}{(1+\epsilon)^2}\left[(1+\epsilon)\,\frac{\mathrm{d}\sigma}{\mathrm{d}\epsilon} - \sigma\right] = 0, \tag{2.15}$$

which simplifies to:

$$\frac{\mathrm{d}\sigma_a}{\mathrm{d}\epsilon} = \frac{\sigma_a}{1+\epsilon} = \frac{\sigma_a}{\lambda} \tag{2.16}$$

where $\lambda = 1 + \epsilon$, is the draw ratio (Ward and Hadley, 1993, p. 217). This formulation is known as Considère's construction. This implies that the tangent point on the true stress-strain curve, where the tangent line is extended and intersects $\epsilon = -1$ or $\lambda = 0$, is a local maximum or minimum (Ward and Hadley, 1993, p. 217). This is schematically displayed in Fig. 2.12.

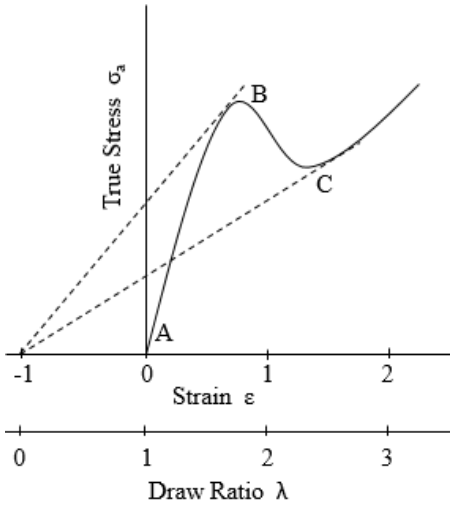

Figure 2.12: Considère's construction is illustrated (Ward and Hadley, 1993, p. 219, Fig. 11.6). At the turning points (points B and C), the extended tangent line of the true stress-strain curve crosses the strain axis at, $\epsilon = -1$ or draw ratio axis at, $\lambda = 0$. Region A-B represents the linear elastic region, afterwards yielding starts to occur at point B. At this stage a neck will start to form and will stabilise before the onset of cold drawing at point C.

2.2.7 Mechanical Failure: Temperature Dependency

The temperature effect and strain rate dependency on polymethyl methacrylate (PMMA) are depicted in Fig. 2.13. Note that the general representation of Fig. 2.9 complies with the results given in Fig. 2.13a. The uniaxial tensile tests on PMMA at different temperatures are displayed in Fig. 2.13a. Ductility increases as the temperature increases. As a result, the yield stress σ_y and failure stress σ_B decrease with increasing temperature; see Fig. 2.13b.

Brittle behaviour is normally observed at low temperatures, $T < T_g$ where the strain at failure is relatively low, being less than 10 % and failure occurs without yielding (Ward and Hadley, 1993, p. 219). The yield point starts to appear near the glass transition temperature, T_g, as amorphous region transforms from glass-like to ductile (Landel and Nielsen, 1993, p. 253).

The dash lines in Fig. 2.13b represent the effect of higher strain rates. Thus, for a given temperature, the failure stress σ_B and yield stress σ_y will increase when the strain rate is increased. These results comply with the viscoelastic nature of the material as discussed in section 2.1.4.

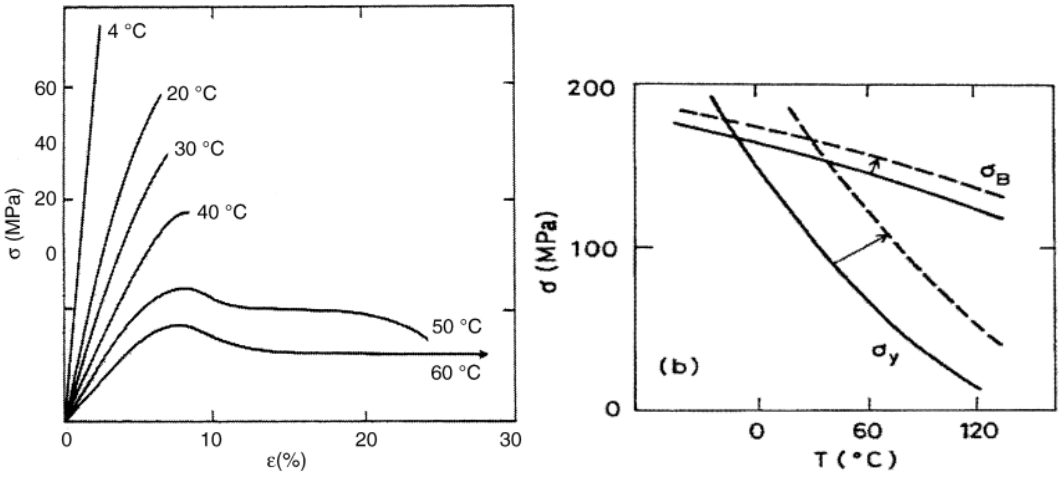

(a) Tempeature Effect: Uniaxial Tests

(b) Yield and Failure Temperature and Strain Rate Effect

Figure 2.13: The temperature and strain rate effect on polymethyl methacrylate (PMMA) is displayed where Fig. 2.13a (Jardret and Morel, 2003, p. 323, Fig. 1) illustrates that PMMA behaves more ductile as the temperature increases. In Fig. 2.13b (Jardret and Morel, 2003, p. 323, Fig. 2) the effect of strain rate is illustrated through the dashed lines where higher strain rates induce brittle-like behaviour.

2.2.8 Modelling Mechanical Failure

Well-explored mechanical failure theories exist for brittle failure of polymers, e.g. the Griffith fracture theory considers the balanced energy required to produce two surfaces with the release of elastic stored energy (Ward and Hadley, 1993, p. 248). The theory further explores the discrepancy between theoretical analyses and measured results stating that elastic energy is not distributed uniformly throughout a body, but is concentrated at the surrounding of small cracks (Ward and Hadley, 1993, p. 248). These defects result in fracture after crack propagation has reached a critical state (Ward and Hadley, 1993, p. 248). The theory was later updated by Irwin, where the new formulation also looked at the dissipation of surface energy about the tip of an ideal crack length due to plastic deformation (Ward and Hadley, 1993, p. 249).

However, these theories are applicable for highly brittle materials, where the polymers used during the course of this project are ductile. Due to the complex nature of semicrystalline polymers, it is difficult to derive accurate theories describing ductile failure from first principles. Therefore, an indirect approach will be followed during the course of this project, where a metamodel will be constructed to describe the seal strength of the film to gland fitments.

Metamodelling seeks to find the relationship between the generated outputs and inputs of the specific system. A number of techniques exist to solve such problems, among which are response surface methodology (RSM), support vector regression and artificial neural networks. The technique of choice concerning this project is RSM since it provides valuable insight into the respective variables at play; provides confidence intervals on future predictions, which are valuable information concerning the nature of the problem, and it is a well-documented approach for relatively small data sets. The methods and materials will be discussed in the proceeding chapter, where response surface methodology will be discussed in section 3.6.

Chapter 3

Materials and Methods

This chapter will look into the materials and methods used during the course of this project. It provides the procedures followed; from the initial stage of constructing the design of experiments until the development of statistical models based upon the response surface methodology (RSM) approach.

3.1 Materials

The product layout being investigated is a double layer of 100 µm thick polyethylene film sealed on a 2 inch hexagon gland. This layout is the most general product layout produced by Anderson Lid Company (ALC).

Table 3.1 provides the relevant material specifications of the film and gland fitments used. The gland fitments are manufactured through injection moulding, whereas the films are produced from film-blowing. Both of these processes influence the characteristics of the final item produced since both processes allow melt to crystallise in particular directions.

During film blowing, the material crystallises in the blow direction, as discussed in the literature chapter. Film thickness can commonly vary about 10 % from the specified nominal thickness. During injection moulding, the material crystallises in the flow direction, away from the injection point. This process can induce internal stresses, due to non-uniform cooling, which can lead to part warpage. The gland fitment used for this project is displayed in Fig. 3.1, where Fig. 3.1a displays the isometric view and Fig. 3.1b displays the top view. The injection point is located on the flange, as can be seen in the bottom of Fig. 3.1b and part warpage is normally seen about the perimeter of the flange. This is a covariate, which is an uncontrollable variable effecting the seal strength (Mason *et al.*, 1989, p. 93).

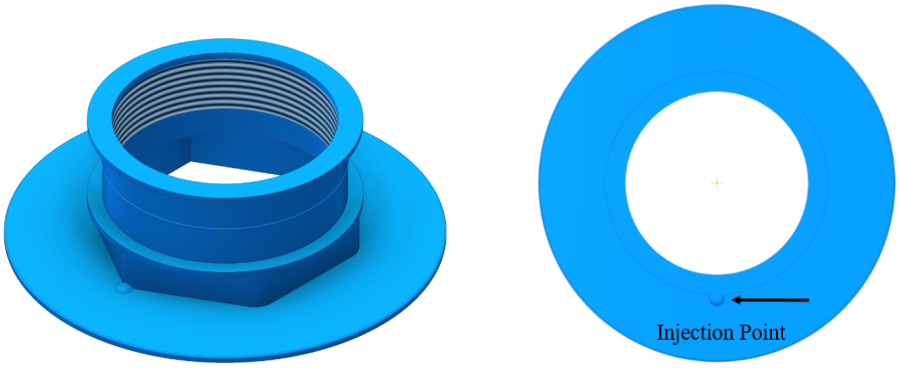

(a) Isometric View (b) Top View

Figure 3.1: The 2 inch hexagon gland is displayed where Fig. 3.1a and Fig. 3.1b respectively displays the isometric and top view of the gland.

Table 3.1: The table provides the material specifications of the film and fitments used concerning this project as provided by SASOL (2017). The glands and films are respectively produced from linear low density polyethylene (LLDPE) and low density polyethylene (LDPE).

	Material	
Specification	LLDPE Gland Fitment	LDPE Film
Grade Name:	HR3950	LF2103
MI (g/10min) [ASTM D1238]:	5	0.3
Density (g/cm^3) [ASTM D1505]:	0.939	0.921
Additives:	None	Antioxidant
Processing:	Injection Moulding	Film Extrusion

3.2 Design of Experiments

Experiments contain covariates and controlled variables; the controlled variables are defined as factors (Mason *et al.*, 1989, p. 92). The factors are varied during the execution of a design of experiments (DOE) to capture its influence on the response where the response is the measured output (Mason *et al.*, 1989, p. 93). The DOE approach entails the development of a well-defined experimental execution plan to capture the necessary data required for statistical modelling. Experimental designs should be economical and should be able to provide estimates of the experimental error (Mason *et al.*, 1989, p. 91). Economical designs refer to the best trade-off between minimising experimental data points while providing enough resolution to capture the adequate response

(Mason *et al.*, 1989, p. 91). This section will discuss the DOEs considered for the purpose of this project. Firstly, the two-factorial design is discussed, followed by the Box-Behnken design and the central composite design. The first is generally used for first order responses and the latter two for higher order responses. These DOEs work in conjunction with the response surface methodology (RSM) approach.

3.2.1 Two-Level Factorial Design: 2^k

Two-level factorial designs are able to capture the linear main effects of factors and the interaction effects thereof (Myers *et al.*, 2011, p. 73). Each replicate run has 2^k experimental trials, where k is the number of factors (Myers *et al.*, 2011, p. 73), e.g. when the response of three factors are studied by using a 2^k design (see Fig. 3.2), then the total number of experiments required will be $2^3 = 8$.

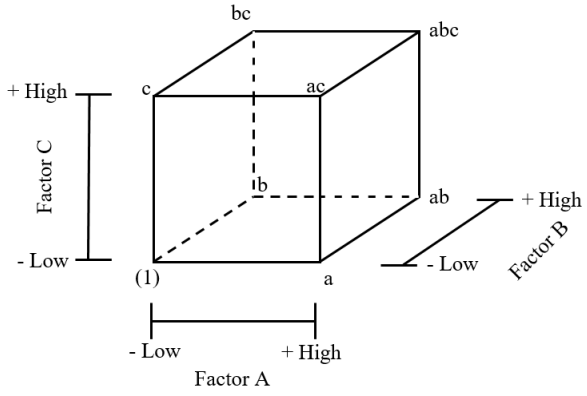

Figure 3.2: The two-level three factorial (2^3) design space is illustrated (Myers *et al.*, 2011, p. 86, Fig. 3.5 (a)). The schematic displays a full 2^3 design, where a single plane represents a 2^2 design. Each corner of the cube represents a single experimental trial. Each factor is controllable, where the low and high notations indicate the two levels of each factor. The total number of experimental trials are 8.

Factorial designs are generally used during the screening phase of experimental designs. It enables the experimenter to establish the significant variables at play, and it provides guidance to construct the boundaries for the next experimental design space (Myers *et al.*, 2011, p. 73). From Fig. 3.2, the design space is defined by the lower and upper limits of each factor (Mason *et al.*, 1989, p. 92). The geometrical cube is given in terms of the controllable variables. It is a schematic representation of the required experiments to capture the response at each factor level. The design matrix of the 2^3 design is given in Appendix A, Table A.1. These designs can be expanded to any

number of factors, e.g. when the factorial design is expanded to a two-level four factorial design, 2^4, then Fig. 3.3 is the resultant design space geometry.

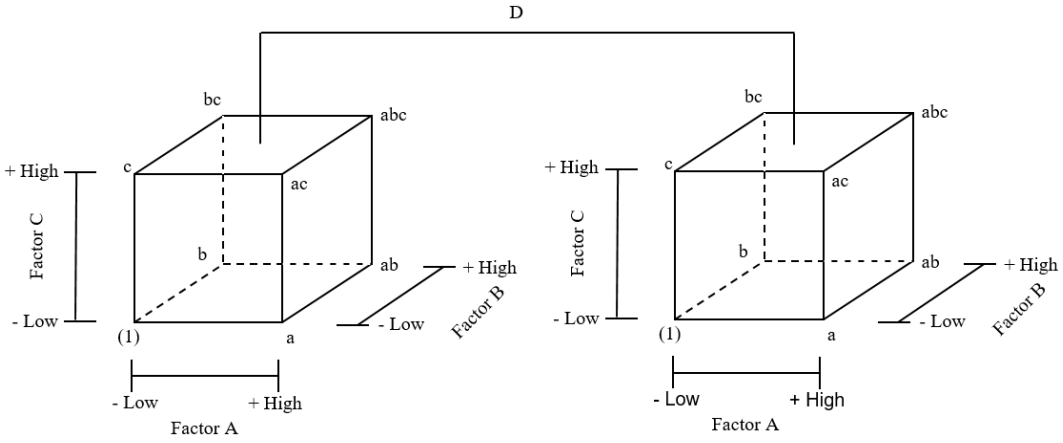

Figure 3.3: The two-level four factorial (2^4) design space is illustrated (Myers *et al.*, 2011, p. 97, Fig. 3.10). The schematic displays a full 2^4 design; the expansion from three factors to four factors is shown. The design space geometry displays a full 2^3 design at each level of factor D. The total number of experiential trials are 16.

Generally, a first-order response surface is fitted to a 2^k design; this forms part of the screening phase, where estimates of the factors are conducted to perform the method of steepest ascent (Myers *et al.*, 2011, p. 73). The steepest ascent will guide the experimenter to a new design space if the current design space does not contain a possible optimum (Myers *et al.*, 2011, p. 73).

A variety of DOEs is based on the factorial design, an example of which is the central composite design (Myers *et al.*, 2011, p. 73). When the factorial design is in the adequate design space, and a higher order model is required, then the design can be expanded to a central composite design without re-conducting the initial factorial experiments (Myers *et al.*, 2011, p. 73). As a result, the experiments are economically executed.

Factorial designs are often used to conduct experiments in literature. The applications of which vary significantly since the approach does not entail first principle derivations of the problem. A few examples of factorial designs used in literature are the following: Terezo and Pereira (2000) have investigated the properties of $Ti/IrO_2{-}NB_2O_5$ electrodes by using a fractional factorial design. Seki *et al.* (2006) have used a full factorial design to study the absorption of boron from aqueous solution on aluminium oxide, Al_2O_3. The statistical analysis has shown boron absorption decreases as the pH and temperature increase. Vicente *et al.* (1998) have made use of a factorial design to model biodiesel production; a response surface was constructed and optimised. These

are only a few examples of the diversity of problems solved in literature by using factorial designs in conjunction with response surface methodology.

3.2.2 Box-Behnken Design

The Box-Behnken design is schematically displayed in Fig. 3.4. This design makes optimum use of experimental data points that are required for the adequate model dimensionality (Mason *et al.*, 1989, p. 220). The design does not contain experimental trial runs at the corners of the design space. This allows the design to be used in applications when factor levels are practically limited (Mason *et al.*, 1989, p. 220).

Box-Behnken and central composite designs can be conducted sequentially (Mason *et al.*, 1989, p. 204). This becomes useful when the model contains a large number of factors. This equates to a large number of experimental trials that need to be conducted at homogeneous conditions. By using a design that permits blocking, the non-homogeneous effects can be reduced (Mason *et al.*, 1989, p. 140).

Both the Box-Behnken and central composite designs are more efficient than a full factorial design since they require fewer experimental trials to capture higher order responses (Mason *et al.*, 1989, p. 204). Among these, the Box-Behnken design makes use of the least number of experimental trials (Mason *et al.*, 1989, p. 220), e.g. the Box-Behnken design utilises 13 trial runs to capture a full second-order response of three factors, where the centre composite design uses 15 trial runs and the full factorial design requires $3^3 = 27$ experimental trials. As a result, the Box-Behnken design is preferred when extensive experimental trials are too expensive to conduct (Mason *et al.*, 1989, p. 220).

Aslan and Cebeci (2007) have made use of a Box-Behnken design to model Turkish coals. Three factors were considered; these were bond work index, grinding and ball diameter of the mill. Tests were constructed to grind the coals and to study the effects of three factors of interest. Aslan and Cebeci (2007) have chosen the Box-Behnken design due to its simplicity.

Annadurai and Sheeja (1998) studied the influence of temperature, pH and particle size of the absorption of verofix red by using biopolymer. These factors were studied at three levels, and the Box-Behnken DOE was the preferred design of choice. These two examples in literature are among many applications where Box-Behnken designs are used.

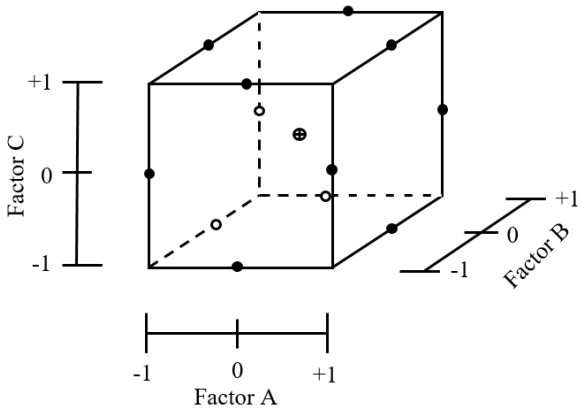

Figure 3.4: Three factor Box-Behnken design space is illustrated (Mason *et al.*, 1989, p. 219, Fig. 11.12). The schematic displays a total of 13 experimental trials required. When three repeated centre points are conducted, the total number of trials equates to 15. The factor values are displayed in terms of the coded variables, where -1, 0 and $+1$ respectively represents the low, mid and high values of the factor levels.

3.2.3 Central Composite Design

The central composite and face-centered composite designs are extensively used for fitting second order response surfaces (Myers *et al.*, 2011, p. 113). The central composite and face-centered composite designs are illustrated in Fig. 3.5. The total number of test runs required for each can be calculated by:

$$n = 2^k + 2\,k + m \tag{3.1}$$

where k is the number of factors and m the number of cube centre runs (Mason *et al.*, 1989, p. 217). The repeated cube centre runs normally vary from three to five (Myers *et al.*, 2011, p. 113), e.g. for three factors and three centre runs, the total number of test runs will be $n = 2^3 + 6 + 3 = 17$. The discrepancy between the two designs lies with their axial points; see Fig. 3.5. The axial points of the face-centered design lie on the faces (Mason *et al.*, 1989, p. 219); see Fig. 3.5b. In terms of coded variables, this is at $+1$ and -1 for each factor. However, for the central composite design, the axial points lie outside the face planes, at a distance that allows for a rotatable design (Mason *et al.*, 1989, p. 217). A rotatable design ensures that the variance of the predicted response is constant throughout the design space. As a result, the quality of future predictions is constant throughout (Mason *et al.*, 1989, p. 305). This is highly advantageous for constructive predictive models. To achieve a rotatable design with the central composite geometry, the axial points should lie at a distance:

$$a = F^{\frac{1}{4}} \tag{3.2}$$

where a is the axial distance from the cube centre in terms of coded variables, and F is the number of factorial points (Mason *et al.*, 1989, p. 217). The number of factorial points is equated for a full factorial by:

$$F = 2^k, \tag{3.3}$$

k being the number of factors (Mason *et al.*, 1989, p. 217), e.g. the axial distance for a rotatable central composite design for three factors will equate to $a = (2^3)^{\frac{1}{4}} = 1.6818$. The resultant design matrix for a central composite design with three factors and three reaped centre runs is provided in Table A.3. Note that run numbers 9 to 14 represent the axial points. Since those points lie on the faces of a face-centered composite design, as depicted in Fig. 3.5b, the run numbers containing the ± 1.68 values will change to the coded values of ± 1 for a face-centered composite design (Mason *et al.*, 1989, p. 219). The face-centered central composite design requires only three levels $(0, \pm 1)$ for each factor, whereas the central composite design makes use of five levels $(0, \pm 1, \pm 1.68)$ for each factor (Mason *et al.*, 1989, p. 219). Therefore, the face-centered design is preferred over the central composite design when the levels of the variables are constrained (Mason *et al.*, 1989, p. 219). However, the central composite design, being rotatable, should be used when possible.

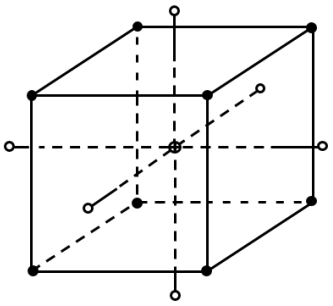

(a) Central Composite

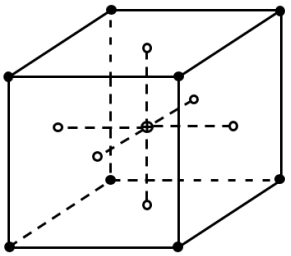

(b) Face-Centered Central Composite

Figure 3.5: Central composite design space is illustrated, where Fig. 3.5a (Mason *et al.*, 1989, p. 218, Fig 11.10) and Fig. 3.5b (Mason *et al.*, 1989, p. 219, Fig 11.11) respectively show the central composite and face-centered composite design spaces for three factors.

3.3 Sealing Process

Once the appropriate design of experiments (DOE) is chosen, the corresponding film to gland seals can be produced. The sealing process is summarised in these few steps:

1. Cut 400 mm by 400 mm sheets from LDPE film.
2. Cut 76 mm diameter hole in centre of each LDPE sheet.
3. Fit sheet over gland fitment.
4. Place film and gland on base of the heat head and produce seal.

The total number of sheets required equates to the number of trial runs in the DOE times the number of plies used for each film to gland fitment; each sheet is dimensioned 400 mm by 400 mm and the centre hole of diameter 76 mm is punched in the centre of each sheet. The total number of glands required will correspond to the number of trial runs of the DOE.

At this stage the sheets are fit onto each gland; see Appendix B.1, so that preparation before the sealing can occur. The machine direction of the films is aligned with the injection point of each gland to ensure uniformity between each test run. This is illustrated in Appendix B.1, where the injection point is located at the bottom of both figures and the corresponding machine direction of the films is in the vertical-downwards direction of the figures.

Finally, the seals are produced with a sealing heat head, which is depicted in Fig. 3.6a. The process variables corresponding to the DOE are adjusted on the machine as depicted by A in Fig. 3.6a. These variables are the heat head temperature, actuated pneumatic pressure on the sealing surface, and the process dwell time, which is the amount contact time during the sealing process.

The film to gland fitment is placed on the centre of the base, B, of the machine. A digital display indicates the real-time temperature reading of the heat head, which should comply with the set temperature once at equilibrium. Then the actuator, D is activated via a button and the seal is produced. Appendix B.2 displays the resulted gland seal.

The base, B is machined to account for concentricity where the base anvil has a groove to help align the gland with the heat head. However, the tilting angle of the head can be adjusted if necessary. A technician sets up the alignment of the machine beforehand by using ink paper. The ink paper is used to check the pressure distribution of the head on the sealing surface; Fig. 3.6b displays a piece of paper used for such a setup. A non-uniform pressure will result in an uneven distribution of the ink, therefore adjustments can be made accordingly.

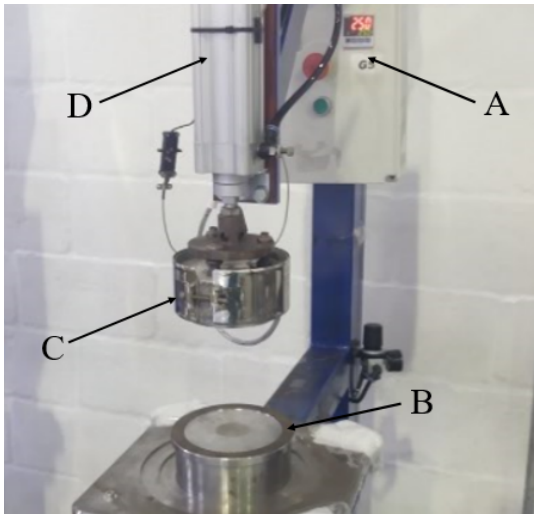

(a) Sealing Heat Head

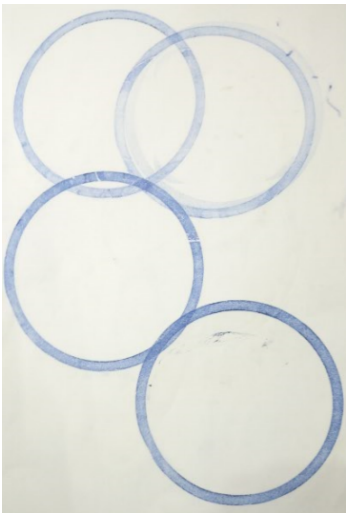

(b) Setup Allignment: Ink Paper

Figure 3.6: The sealing head is shown in Fig. 3.6a, where the major sections of the machine is labelled accordingly to, the controls A, base anvil B, heat head C and pneumatic cylinder D. Ink paper is used during the setup, where the uniformity is checked via the distribution of ink on paper; see Fig. 3.6b.

3.4 Uniaxial Tensile Testing

Since the project is concerned with seal strength, uniaxial tensile testing was performed on the film to gland fitments. It is a repeatable test method, which is relatively inexpensive to perform. This proved to be useful since a large number of tensile tests were required to develop a statistical accurate model. A number of test methods are available for polymer uniaxial tensile testing; e.g ISO 527 - 3 describes how to determine the tensile properties of plastics in general, where ASTM F88/F88M - 15 looks at determining the seal strength of polymers, and ASTM D882 - 02 looks at tensile properties of thin plastics. This project will only consider seal strength properties, therefore using ASTM F88/F88M - 15 as a guideline. The rest of this section will discuss the techniques and setup used for capturing the tensile properties. A description of the setup will be provided first followed by a detailed discussion on the sample geometry.

3.4.1 Setup and Preparation

An MTS tensile tester fitted with a calibrated 500 N load cell was used to perform the tensile tests where the strain rate was set to 50 mm/min and the data acquisition rate was set to 5 Hz, which complies with the ASTM F88/F88M - 15 standard. ASTM F88/F88M - 15 provides three possibilities for gripping the sample. These are unsupported 90° pull, supported 90° pull and

180° peal test. It was decided that the 180° peal test is the most appropriate technique concerning this project. It is performed by folding and pulling the film 180° away from the nominal direction, see Fig. 3.7.

Since polymers are highly viscoelastic and dependant on temperature conditions, the samples are conditioned in advanced before the tensile tests can be conducted. This is accomplished by placing the batch of samples at room temperature for more than 24 hours where room temperature is 23 °C within ±2 °C. The tensile tests should be performed under similar conditions. This was achieved in the project by placing all the samples in a room who's temperature was monitored.

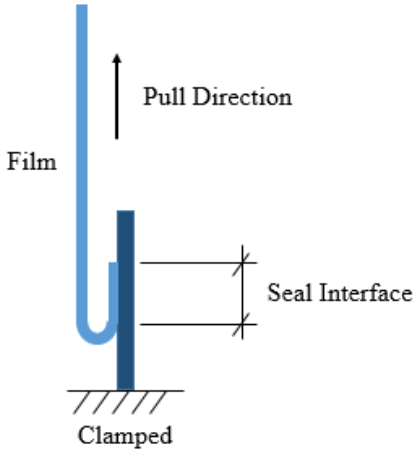

Figure 3.7: Peal test; the sample is clamped and the film is pulled 180° away from the seal interface.

3.4.2 Sample Geometry

Sample geometry plays a critical role in uniaxial tensile testing. The rest of this section will focus on sample geometry. Firstly, a standard geometry was used and tested, which gave unsatisfactory results. The failure occurred in the film rather than at the seal interface. Also, the response curves obtained did not provide clear insight into the tensile properties. These properties are a well-defined yield point, neck region with the onset of cold drawing and failure; see Fig. 3.13. The next step involved developing a sample geometry that provided satisfactory results. This was achieved with a wedge shape geometry. The subsequent sections will discuss the test results of both and the findings concerning the new sample geometry.

3.4.2.1 Rectangular Samples

The ASTM F88/F88M - 15 standard suggests using rectangular samples of dimension 25.4 mm by 76 mm. Anderson Lid Company (ALC) in comparison uses 114 mm by 14 mm rectangular gland seal samples. A single layer of 100 µm LDPE film was welded on a two inch hex gland by means of the G1 machine at ALC. A total of eight samples were cut from this single gland seal, with a die embedded at ALC. The tensile test were conducted at a data acquisition rate of 5 Hz and the strain rate was set to 50 mm/min. These test results are displayed in Fig. 3.8.

However, the rectangular samples gave unsatisfactory results upon the first investigation. This is evident in Fig 3.8. Most samples failed prematurely in the film rather than at the seal interface. Also, the obtained response curves did not display a well-defined stiffening point. The former was due to rough edge samples, and the latter had to do with the sample geometry.

The rough edges act as stress concentrations during uniaxial testing where the samples fail prematurely in the film when necking occurs. This is undesirable since failure is required at the seal interface. The rough edges were introduced during punching. This is when a pneumatic actuated die cuts out a sample from a gland seal. The die became blunt after being extensively used on the production line of ALC. As a result, it produced rough edge samples.

Therefore, it was decided to design and manufacture a new die geometry so that the newly produced samples will allow consistent failure at the seal interface, and that the corresponding response curves are well defined.

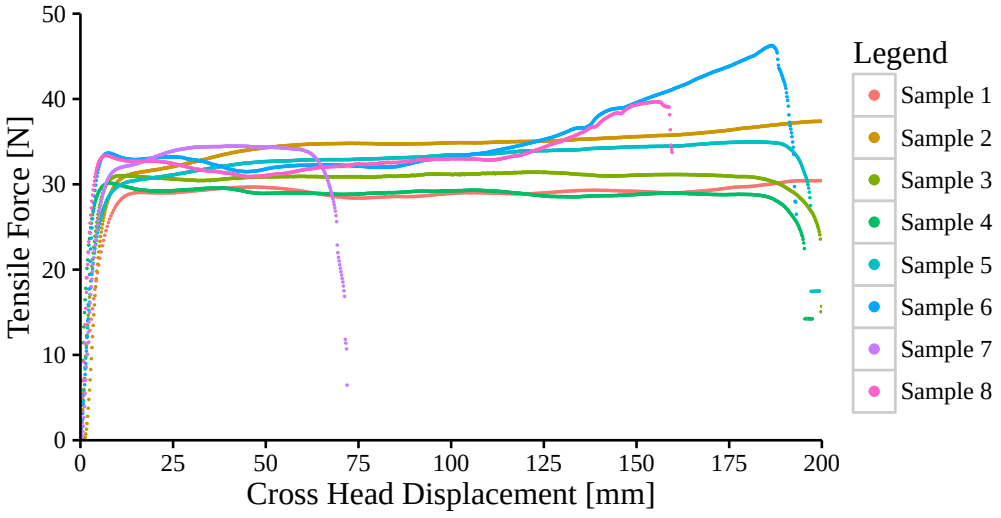

Figure 3.8: Rectangular tensile test results of eight 114 mm by 14 mm rectangular gland seal samples taken from a single gland seal.

3.4.2.2 Triangular Samples

Tensile tests were conducted to compare sample quality produced by the old and new die. The new sample geometry is triangular, where the sample narrows towards the seal interface, as can be seen in Fig 3.9. This ensures that the tensile load is focussed on the seal interface during uniaxial loading. As a result, premature film failure can be eliminated. The results of the repeated test runs are depicted in Fig 3.10. In comparison with Fig 3.8, the new response curves are well defined. Consistent failure occurred at the seal interface for all samples.

Since the samples were taken about the perimeter position of a gland, they were categorised into two groups. These are the in-line or machine direction of the film and cross direction of the film. One can clearly observe the discrepancy between the results of the two major groups in Fig. 3.10, the discrepancy being the strain at failure. This can be described by molecule arrangement in the polymer film. The molecules have to undergo larger orientation in the cross direction than in the machine direction of the film before failure occurs. This finding complies with what was discussed in section 2.2.5.

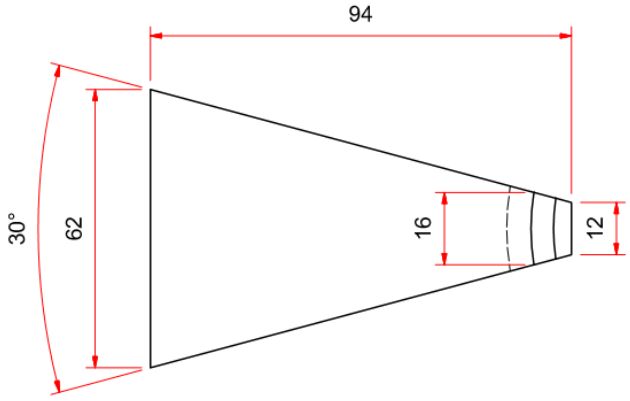

Figure 3.9: Improved sample geometry; the sample narrows towards the seal interface. This ensures that the tensile load is focussed on the seal interface during uniaxial loading; the detailed drawing can be seen in Appendix C.1 in drawing number: $0105 - 2017$.

Appendix C.1 and Appendix C.2, respectively, display the drawings of the newly designed die and template. The template is placed over the gland fitment as a guide for the die to cut equally spaced samples about the perimeter of the flange; Fig. B.5 and Fig. B.6, respectively, display the isometric view and top view of the template and die fitted over the gland fitment. The template is orientated so that one of the legs align with the injection point of the gland. This ensures that samples are cut symmetrically in the machine direction of

the film so that the tested samples consisting of the same sample number can be compared to consecutive trial runs. The sample numbering regime is displayed in Fig. B.7, where the machine direction of the film is indicated by a red line. The absolute angle between each sample is 30°, where all sample positions are measured from the datum, which lies between position one and two, e.g sample one will correspond to an angle of −15° from the reference position, and sample two will correspond to an angle of 15°.

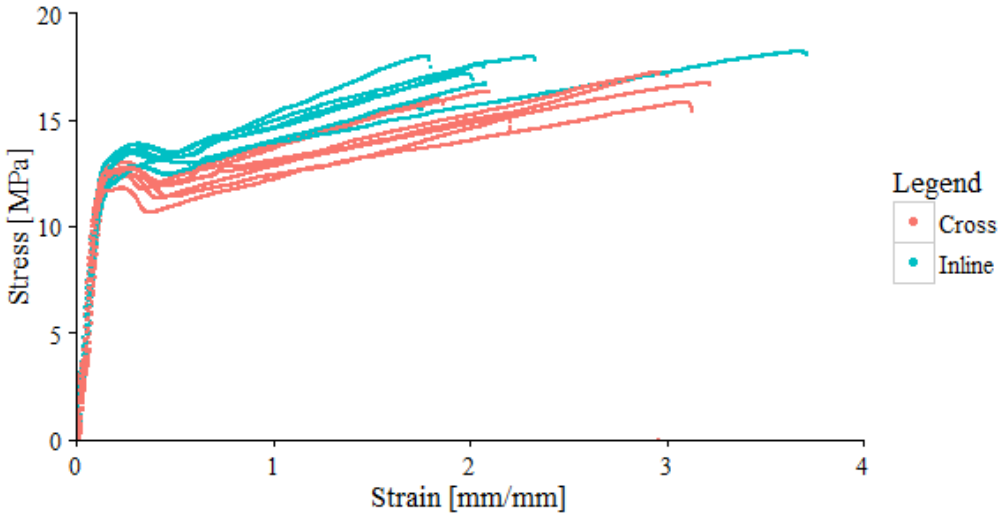

Figure 3.10: Test results of new sample geometry where well-defined response curves were obtained.

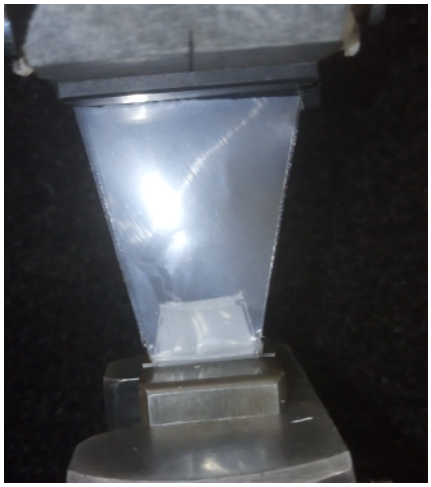

Figure 3.11: Improved sample geometry test setup; the sample is clamped and the film is pulled 180° away from the seal interface.

3.5 Data Processing Algorithm

Data processing plays a vital role in the development of statistical models. The raw test data needs to be processed before statistical modelling. Therefore, in the early stages of this project, a data processing algorithm was developed. The algorithm is depicted in terms of a flow diagram in Fig. 3.12 and the code is provided in Appendix D.

From fig. 3.12 the algorithm imports the necessary libraries. It then creates a empty CSV-file with the adequate headings which is later utilised to write the processed results into. The algorithm then enters the provided directory for the gland folders. Each gland folder contains multiple sample files of uniaxial tests. Each file is opened and the adequate tensile properties are calculated by the subroutines. The algorithm loops through each gland folder and contained sample files. Once terminated the results are written into a CSV-file.

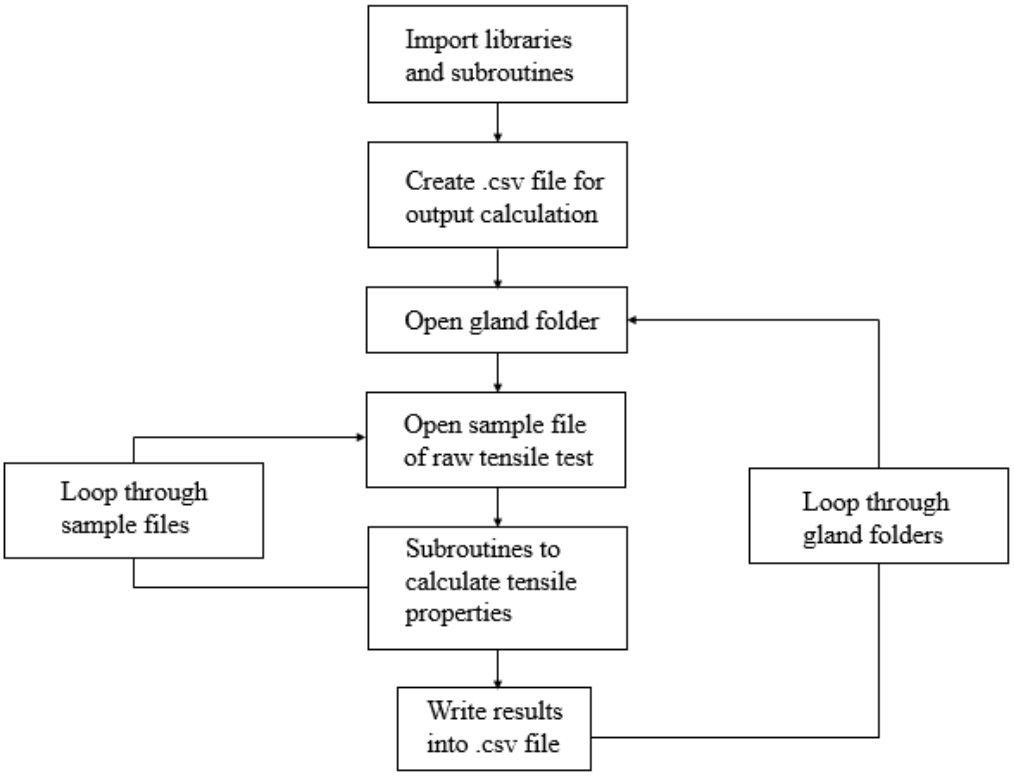

Figure 3.12: Algorithm flow diagram

Analytically the subroutines works by the following principles: From Fig. 3.13, label A refers to the inflection point in the elastic region; the elastic modulus is calculated about this point. Then, the 2 % offset construction line is

drawn to obtain the proportion proof stress, labelled B. Considère's construction is then used to obtain the upper yield point, C. The failure point E, is obtained through a backwards stepwise search for the maximum stress value. Then D, being the point where cold drawing starts to occur, can be obtained by searching for the minimum stress value between C and E. Finally, the second modulus of stiffening is obtained by calculating the gradient between D and E. In conjunction with these variables, the algorithm also calculates the toughness of the response curve, that being the area under the curve.

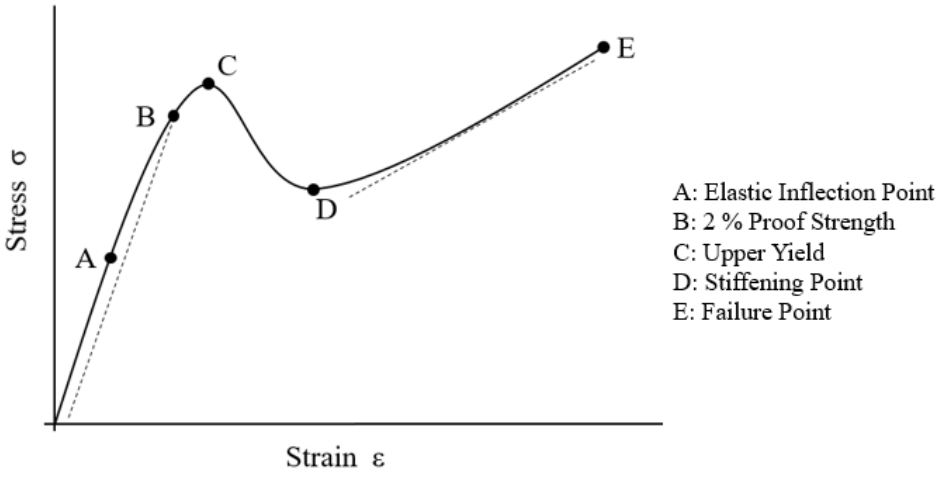

Figure 3.13: Uniaxial tensile properties of interest for the algorithm are labelled.

3.5.1 Inflection Point

The script for obtaining the inflection point is outlined in Appendix D.3.1. Firstly, the appropriate libraries are loaded in lines 2 and 3. Since an inflection point is obtained by the second derivative being zero, line 8 obtains the indices of the local maximums of the first derivative filtered data. The reason for calculating the maximums instead of the minimums is that the curvature in the elastic region changes from convex upwards to concave upwards.

Lines 14 to 18 construct the data frame of the derivative peaks and corresponding data points. Then the percentage drop of the peak magnitude is obtained by lines 20 to 22, which is used to obtain the most significant peak of the gradient data (line 29). This point corresponds to the most significant inflection point in the elastic region, thus the corresponding stress and strain values which can be obtained, as shown in lines 31 to 34.

3.5.2 Considère's Construction

Appendix D.3.2 displays the subroutine based on Considère's construction. The approach follows the discussion provided in section 2.2.6. Firstly, the strain is converted to the draw ratio, in lines 9 to 10, as shown in the denominator of eq. 2.16. Then the true stress is obtained by eq. 2.14 in line 12 of the script.

Considère's approach states that the solution where the tangent line of a true stress-draw ratio intersects with the origin (see Fig. 2.12), where the true stress and draw ratio are equal to zero, then the tangent point on the response curve is a turning point (Ward and Hadley, 1993, p. 217). The first solution is the upper yield and the second the stiffening point, where the onset of drawing starts to occur.

Once the gradient is obtained over the whole true stress-draw ratio region, the intercept of every tangent line can be computed, as seen in line 18. The onset of lines 19 to line 25 determines the solution where the intercept goes through the origin of the axes so that the tangent point corresponding to the extended tangent line becomes the upper yield point.

3.5.3 Proportional Proof Stress and Young's Modulus

Appendix D.3.3 contains the subroutine that calculates the proportional proof stress and Young's modulus. The appropriate libraries are imported in lines 2 to 4, and the subroutine calculating the yield point is imported in line 5.

The proportional proof stress is obtained by the solution where the 2 % offset construction line intercepts with the uniaxial response curve; see Fig. 3.13. Therefore, a function is required of the response curve to obtain a solution. However, only discrete data points are available numerically. Therefore, a polynomial is fitted to the response curve up until the upper yield point. Since the upper yield point is at a higher strain value than the proportional proof stress (see Fig. 3.13) it becomes a robust boundary point that will always contain the proportional proof strength. Then, based on the index value of the upper yield point, a polynomial function is constructed in lines 15 to 17.

In the inflection subroutine, see section 3.5.1, the index point of the inflection point has been calculated. The index of the inflection point is used to obtain the stress and corresponding strain value of this point; see lines 21 to 23 of the proportional proof stress and Young's modulus subroutine. The information is then sent, see line 24 of Appendix D.3.3, to the yield point subroutine, as provided in Appendix D.3.4 where Young's modulus is calculated by the gradient about the inflection point in the elastic region; see line 17 of the yield point subroutine. Then the 2 % offset construction line is obtained by lines 20 to 21. This is used to find the solution where the construction line crosses the response curve, as seen in lines 23 to 32.

3.5.4 Failure Stress and Strain

This subroutine is provided in Appendix D.3.5. The subroutine starts off by obtaining the number of data points in the data frame; see lines 4 and 5. Then it searches stepwise backwards from the end of the data frame to obtain the maximum failure stress. This is achieved by large step outer loops in conjunction with smaller step inner loop searches; see lines 7 to 10. The two work in conjunction to prevent the algorithm from converging to a local maximum, and to overcome the phenomenon where the tensile machine sometimes records the tensile force after the maximum failure stress has occurred, which results in the onset of concave downwards stress data. Once the algorithm has converged, the failure stress and strain are obtained (lines 12 and 13).

3.5.5 Second Modulus: Cold Drawing

As discussed before, the stiffening point or strain hardening point is obtained in the data processing script as the minimum stress value between the upper yield and failure point; see lines 68 to 70 of Appendix D.2. Once the point is known the subroutine responsible for obtaining the second modulus can be called. Cold drawing has a stiffening effect on the response curve; the gradient of which (see Fig. 3.13 between label D and E) is referred as the second modulus. The script for computing the second modulus is provided in Appendix D.3.6. The subroutine calculates the gradient between the failure point and stiffening point in line 12. From this, the corresponding tangent line is constructed (see lines 14 to 16) and sent back to the main script (line 18). The tangent line is plotted with the response curve in a later stage to check whether it approximates the stiffening response.

3.5.6 Numerical Integration: Toughness

The algorithm for numerical integration is based in the following formulation. When discrete points of a response curve are available, then the curve can be divided into sections between each data point, as shown by Fig. 3.14. To represent the area of the section, each section is subdivided by a triangle geometry in conjunction with a rectangle geometry; see Fig. 3.14. These two geometries are simple to work with, and the combined area of both can be easily obtained by:

$$\begin{aligned} A_{ab} &= 0.5\,(b-a)\,(F(b)-F(a)) + (b-a)\,(F(a)) \\ &= (b-a)[0.5\,F(b) - 0.5\,F(a) + F(a)] \\ &= 0.5\,(b-a)\,[F(b)+F(a)] \end{aligned} \tag{3.4}$$

where A_{ab} is the approximated area of the section consisting off a triangle and a rectangle, a and b are respectively the x-values at the the discrete data points

$F(a)$ and $F(b)$. Although not shown, eq. 3.4 is also true when $F(a) > F(b)$. By integrating over the whole curvature region, then eq. 3.4 is expanded to:

$$A_{tot} = 0.5 \sum_{i=1}^{k} (x_{i+1} - x_i)(F(x_{i+1}) + F(x_i)) \tag{3.5}$$

where A_{tot} is the approximated area under the whole curvature region, k is the total number of discrete data points, where x_i and x_{i+1} are the respective x-values corresponding to the discrete data points $F(x_i)$ and $F(x_{i+1})$.

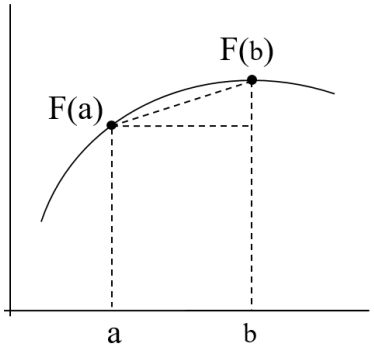

Figure 3.14: The figure displays a method for dividing a region into two geometries, rectangle and triangle, which are used for approximating the area beneath the curvature with numerical integration.

The script for the numerical integration subroutine is provided in Appendix D.3.7. Firstly, the variable corresponding to the toughness is initialised to zero, in line 4. Then eq. 3.5 is applied in lines 5 and 6, where the algorithm loops through each discrete data point, then calculate the area and add it to the area of the previously added regions.

As an example, consider the area of a circle that is halved, where the radius is $r = 2$. The true solution will be, $A_{circle} = 0.5(2^2\pi) = 6.283$. Now, consider the code provided in the numerical integration script from lines 11 to 17. If $k = 10$, then the algorithm provides a solution of, $A_{circle,\ k=10} = 6.038$, for $k = 100$, then the solution becomes, $A_{circle,\ k=100} = 6.276$ and finally, for $k = 1000$, then $A_{circle,\ k=1000} = 6.283$. Therefore, as the number of discrete data points (k) increase, the approximated area converges to the true solution. The typical number of discrete data points each tensile test contained, concerning this project, was $k = 1000$.

3.5.7 Write Results in CSV-File

The script is provided in Appendix D.3.8. All of the variables required for the subroutine are sent through line 82 of the processing script; see Appendix D.2.

Once inside the file writing subroutine, see Appendix D.3.8, the subroutine starts off in line 10 by extracting the gland number and corresponding process conditions (line 11) of the current iteration. The related process conditions are obtained from the design matrix subroutine, which is provided in Appendix D.3.9. The folder names are then used to classify the gland numbers accordingly; see lines 22 to 28.

Consequently, the sample number of the current iteration is extracted, and classified according to the perimeter angle position; see lines 13 to 20. Once the gland number and specimen number have been classified, the processing results are written accordingly in the results file (lines 30 to 35).

3.6 Response Surface Methodology

Myers *et al.* (2011) define response surface methodology (RSM) as the approach to optimise and improve processes by means of statistical and mathematical techniques (Myers *et al.*, 2011, p. 1). The processes consist of variables that influence the outcome of a process or product; this outcome is known as the response (Myers *et al.*, 2011, p. 1). RSM seeks to find the relationship between the factors and the response. Although the true response is unknown (Myers *et al.*, 2011, p. 2), an approximated relationship of the response can be constructed and evaluated. The RSM has three main objectives. These are (Myers *et al.*, 2011, p. 8):

- Map the response surface over a desirable region.
- Obtain optimised conditions of the response.
- Obtain operating conditions that achieve all requirements.

3.6.1 General Approach

The approach of RSM is sequential; different phases in the approach exist before the outcomes can be met or achieved. The initial phase, or phase zero, is the screening phase (Myers *et al.*, 2011, p. 7). This involves obtaining the significant variables of interest (Myers *et al.*, 2011, p. 7) as these will determine the complexity of the design of experiments required for the proceeding phases. Fewer significant variables will result in fewer experiments required to construct the response surface. Once the significant variables are identified, phase one can proceed.

Phase one involves obtaining the adequate design space region. An adequate region is one that contains the process optimum (Myers *et al.*, 2011, p. 7). Firstly the current phase is analysed to check whether an optimum falls in the region. If it does not, then the experimenter must make adjustments to obtain the adequate design space. At this stage, only first order response

surfaces are constructed and the method of steepest ascent is used to guide the experimenter to new design space regions (Myers *et al.*, 2011, p. 7). Phase two proceeds once the adequate region is obtained.

Phase two starts off in the adequate design region. During this phase, the resolution of the DOE near the optimum can be increased to obtain a closer approximation of the true response (Myers *et al.*, 2011, p. 7). This phase predominantly makes use of second-order models. Once an adequate response equation is obtained the process conditions can be optimised (Myers *et al.*, 2011, p. 7).

3.6.2 Linear Regression

RSM makes use of experimental results to construct linear regression models. The input variables are adjusted during the experimental trials according to a predetermined design of experiments (DEO), as discussed in section 3.2. Then the response (y_j) of each experimental trial is measured. Linear regression is then used to establish the relationship between the regression variables and the measured response. The response, being a function of the input variables, can be abbreviated as (Myers *et al.*, 2011, p. 2):

$$y = f(\xi_1, \xi_2, \cdots, \xi_k) + \epsilon, \tag{3.6}$$

where ξ_j are the natural variables and ϵ is the statistical error that accounts for the variability not accounted by the model equation (Myers *et al.*, 2011, p. 2). It is assumed that the statistical error (ϵ) is normal and independent distributed with a zero mean and variance σ^2, abbreviated as $\epsilon \sim NID(0, \sigma^2)$. Then the expected value of the response becomes (Myers *et al.*, 2011, p. 2):

$$E(y) \equiv \eta = E[f(\xi_1, \xi_2, \ldots, \xi_k) + E(\epsilon) = f(\xi_1, \xi_2, \ldots, \xi_k). \tag{3.7}$$

This can be rewritten in terms of the coded variables (x_j) as (Myers *et al.*, 2011, p. 3):

$$\eta = f(x_1, x_2, \ldots, x_k). \tag{3.8}$$

Coded variables are the result of non-dimensionalising the natural variables (Myers *et al.*, 2011, p. 3). This is, ξ_j can be non-dimentionalised to x_j, with the following relationship (Myers *et al.*, 2011, p. 18):

$$x_n = \frac{\xi_n - [\max(\xi_n) + \min(\xi_n)]/2}{[\max(\xi_n) - \min(\xi_n)]/2} \tag{3.9}$$

where $\min(\xi_n)$ and $\max(\xi_n)$ respectively refer to the lower and upper boundaries of the input variables. The DOEs discussed in section 3.2 were given in terms of coded variables, where e.q. 3.9 is used to obtain the natural variables

for each experimental trial. A typical first order response equation is given by (Myers *et al.*, 2011, p. 14):

$$y = \beta_0 + \beta_1 x_1 + \beta_2 x_2 + \cdots + \beta_k x_k + \epsilon. \tag{3.10}$$

The model equation is referred as a multiple linear regression model, which has k predictive variables (x_j), or factors, and $k+1$ regression coefficients (β_j) where $j = 0, 1, \ldots, k$. This equation describes the behaviour of the regression variables as a hyperplane in k-dimensional space (Myers *et al.*, 2011, p. 14), e.g. a two factors second order model with interaction can be constructed as follows (Myers *et al.*, 2011, p. 14):

$$y = \beta_0 + \beta_1 x_1 + \beta_2 x_2 + \beta_{11} x_1^2 + \beta_{22} x_2^2 + \beta_{12} x_1 x_2 + \epsilon. \tag{3.11}$$

Let, $x_3 = x_1^2$, $x_4 = x_2^2$, $x_5 = x_1 x_2$, $\beta_3 = \beta_{11}$, $\beta_4 = \beta_{22}$, and $\beta_5 = \beta_{12}$, then:

$$y = \beta_0 + \beta_1 x_1 + \beta_2 x_2 + \beta_3 x_3 + \beta_4 x_4 + \beta_5 x_5 + \epsilon, \tag{3.12}$$

which is a linear regression model (Myers *et al.*, 2011, p. 14). Therefore, the regression coefficients are determined by linear regression techniques regardless the order of the response curve (Myers *et al.*, 2011, p. 14). In general the model equation can be written in matrix form as:

$$\mathbf{y} = \mathbf{X}\,\boldsymbol{\beta} + \boldsymbol{\epsilon} \tag{3.13}$$

where

$$\mathbf{y} = \begin{bmatrix} y_1 \\ y_2 \\ \vdots \\ y_n \end{bmatrix}, \mathbf{X} = \begin{bmatrix} 1 & x_{11} & x_{12} & \cdots & x_{1k} \\ 1 & x_{21} & x_{22} & \cdots & x_{2k} \\ \vdots & \vdots & \vdots & & \vdots \\ 1 & x_{n1} & x_{n2} & \cdots & x_{nk} \end{bmatrix}, \boldsymbol{\beta} = \begin{bmatrix} \beta_0 \\ \beta_1 \\ \vdots \\ \beta_k \end{bmatrix} \text{ and } \boldsymbol{\epsilon} = \begin{bmatrix} \epsilon_1 \\ \epsilon_2 \\ \vdots \\ \epsilon_n \end{bmatrix} \tag{3.14}$$

where $\mathbf{y}$ is the observation vector of dimension $n \times 1$, $\mathbf{X}$ is an $n \times p$ model matrix of the independent input variables, $\boldsymbol{\beta}$ is the regression coefficient vector of dimension $p \times 1$, and $\boldsymbol{\epsilon}$ is the statistical error vector of dimension $p \times 1$. Take note, the first column entries of the model matrix $\mathbf{X}$ are all equal to one, and the proceeding entries are obtained by the DOE matrix being used for a specific problem formulation, as discussed in section 3.2. For instance the model matrix of a two-level three factorial design will equate to:

$$\mathbf{X} = \begin{bmatrix} 1 & -1 & -1 & -1 \\ 1 & +1 & -1 & -1 \\ 1 & -1 & +1 & -1 \\ 1 & +1 & +1 & -1 \\ 1 & -1 & -1 & +1 \\ 1 & +1 & -1 & +1 \\ 1 & -1 & +1 & +1 \\ 1 & +1 & +1 & +1 \end{bmatrix}. \tag{3.15}$$

The method of least squares seeks to find the solution of $\boldsymbol{\beta}$ where the sum of the squares of the statistical error is minimised. This is (Myers *et al.*, 2011, p. 16):

$$\left.\frac{\partial L}{\partial \boldsymbol{\beta}}\right|_{\mathbf{b}} = 0, \quad \text{where} \quad L = \sum_{i=1}^{n} \epsilon_i^2 = \boldsymbol{\epsilon}' \boldsymbol{\epsilon}. \tag{3.16}$$

Myers *et al.* (2011) give the solution to be:

$$\mathbf{b} = (\mathbf{X}' \mathbf{X})^{-1} \mathbf{X}' \mathbf{y} \tag{3.17}$$

where $\mathbf{b}$ is an $p \times 1$ vector of least square estimators, $\mathbf{y}$ is the observation vector of dimension $n \times 1$, and $\mathbf{X}$ is an $n \times p$ model matrix of the independent input variables (Myers *et al.*, 2011, p. 17). Then the regression model in matrix form becomes:

$$\hat{\mathbf{y}} = \mathbf{X}\,\mathbf{b} \tag{3.18}$$

where $\hat{\mathbf{y}}$ is the predicted response, which has the same dimension as the observed response $\mathbf{y}$, this is $n \times 1$ (Myers *et al.*, 2011, p. 17). Then the residuals can be calculated as the difference between the observed and predicted:

$$\mathbf{e} = \mathbf{y} - \hat{\mathbf{y}}. \tag{3.19}$$

3.6.3 Hypothesis Testing

Hypothesis testing is used in multiple linear regression to establish the significance of model parameters (Myers *et al.*, 2011, p. 24). The proceeding section will cover several important statistical hypothesis tests. These are tested for significance of regression, test for significance of individual coefficients and test for significance of a group of regression coefficients (Myers *et al.*, 2011, p. 24). Model assumptions concerning the statistical error are the same as before, this is $\epsilon \sim NID(0, \sigma^2)$ so that the observations y_i are normally and independently distributed with a mean $\beta_0 + \sum_{j=1}^{k} \beta_j\, x_{ij}$ (Myers *et al.*, 2011, p. 24).

3.6.3.1 Sum of Squares Formulation

Firstly, this section will start off with the sum of squares definitions followed by the discussion on the hypothesis tests. The total variance of the observed response can be calculated by the total some of squares (Myers *et al.*, 2011, p. 25):

$$SS_T = \sum_{i=1}^{n} y_i^2 - \frac{(\sum_{i=1}^{n} y_i)^2}{n} = \mathbf{y}'\,\mathbf{y} - \frac{(\sum_{i=1}^{n} y_i)^2}{n}. \tag{3.20}$$

Since the regression response is an approximation of the true solution unaccounted variance exists. Mathematically this can be expressed as:

$$SS_T = SS_R + SS_E \tag{3.21}$$

where SS_R is the regression sum of squares, being an indication of the variance accounted for by the model and SS_E is the residual sum of squares due to lack of fit and experimental error (Myers *et al.*, 2011, p. 24). The residual sum of squares can be equated as:

$$SS_E = \sum_{i=1}^{n} (y_i - \hat{y}_i)^2 \tag{3.22}$$

where y_i is the observed response and $\hat{y}_i$ is the predicted response (Myers *et al.*, 2011, p. 22). Since the difference between an observation and predicted response at a given point is the residual at that point, then eq. 3.22 becomes (Myers *et al.*, 2011, p. 22):

$$SS_E = \sum_{i=1}^{n} e_i^2 = \mathbf{e}'\,\mathbf{e} \tag{3.23}$$

where $\mathbf{e}'$ is the transpose of the residual vector, by expanding the expression with means of eq. 3.18 and eq. 3.19, then

$$SS_E = (\mathbf{y} - \mathbf{X}\,\mathbf{b})'\,(\mathbf{y} - \mathbf{X}\,\mathbf{b}), \tag{3.24}$$

which simplifies to (Myers *et al.*, 2011, p. 22):

$$SS_E = \mathbf{y}'\,\mathbf{y} - \mathbf{b}'\,\mathbf{X}'\,\mathbf{y}. \tag{3.25}$$

Then by substituting eq. 3.20 and eq. 3.25 into eq. 3.21 and solving for SS_R (Myers *et al.*, 2011, p. 25):

$$SS_R = \mathbf{b}'\,\mathbf{X}'\,\mathbf{y} - \frac{(\sum_{i=1}^{n} y_i)^2}{n}. \tag{3.26}$$

The coefficient of multiple determination is provided by Myers *et al.* (2011) as:

$$R^2 = \frac{SS_R}{SS_T} = 1 - \frac{SS_E}{SS_T}, \tag{3.27}$$

which gives an indication of the variance accounted for by the regression model, where $0 \leq R \leq 1$ (Myers *et al.*, 2011, p. 26). However, the sum of squares formulation is dependant on the degrees of freedom of the model terms. As a result, R^2 increases even if unnecessary terms are added to the model (Myers *et al.*, 2011, p. 26). Therefore a high R^2 value does not necessarily imply that a good model approximation is achieved (Myers *et al.*, 2011, p. 26). Instead, an adjusted coefficient of multiple determination R^2_{adj} is used (Myers *et al.*, 2011, p. 27). It can be calculated by:

$$R^2_{adj} = 1 - \frac{MS_E}{MS_T} \tag{3.28}$$

where MS_E is the residual mean square, and MS_T is the total mean square of the observations (Myers *et al.*, 2011, p. 27). The mean square of a quantity is obtained by dividing the sum of squares with the degrees of freedom of that specific quantity; this is:

$$MS_T = \frac{SS_R}{n-1}, \quad MS_R = \frac{SS_R}{k} \text{ and } MS_E = \frac{SS_E}{n-p} \tag{3.29}$$

where the observations have $(n-1)$ degrees of freedom, the regression terms have (k) degrees of freedom, and the residuals have $(n-p)$ degrees of freedom (Myers *et al.*, 2011, p. 24). Recall from eq. 3.14, that n is the number of experimental observations, and p is the total number of regression coefficients β_j, where $k = p-1$. Then by substituting the expressions of MS_E and MS_T into eq. 3.28 result into (Myers *et al.*, 2011, p. 27):

$$R^2_{adj} = 1 - \frac{SS_E \,/\, (n-p)}{SS_T \,/\, (n-1)} = 1 - \frac{n-1}{n-p}\,(1-R^2). \tag{3.30}$$

As a result, R^2_{adj} will most often decrease when unnecessary terms are added to the model (Myers *et al.*, 2011, p. 27). In common practice, R^2 is used in conjunction with R^2_{adj}, where a significant difference between the two values indicates that nonsignificant terms are included in the model (Myers *et al.*, 2011, p. 27). Ideally, when $R^2_{adj} \approx R^2$ then the value of R^2_{adj} can be used for describing the amount of variance accounted for by the model.

3.6.3.2 Regression Significance

The test for significance of regression establishes whether at least one non-zero regression coefficient exists (Myers *et al.*, 2011, p. 24). The appropriate hypothesis is outlined in eq. 3.31 (Myers *et al.*, 2011, p. 24).

$$\begin{aligned} H_0 &: \beta_1 = \beta_2 = \cdots = \beta_k = 0 \\ H_1 &: \beta_j \neq 0 \text{ for at least one j} \end{aligned} \tag{3.31}$$

When F_0 exceeds $F_{\alpha,k,n-k-1}$ the null hypothesis is rejected, or alternatively with the P-value approach, H_0 is rejected when the P-value of statistic F_0 is less then α (Myers *et al.*, 2011, p. 24). This implies that at least one regression variable x_j exists that significantly contributes to the model (Myers *et al.*, 2011, p. 24). In common practice, α is chosen to be 0.05 (Myers *et al.*, 2011, p. 26) where F_0 can be calculated by the following:

$$F_0 = \frac{MS_R}{MS_E} \tag{3.32}$$

where the means square values can be obtained through eq. 3.29. Once the null hypothesis is rejected, confirming the alternative hypothesis, then the significance of individual coefficients can be tested.

3.6.3.3 Significance on Individual Coefficients

This test considers whether an individual regression coefficient is significant (Myers *et al.*, 2011, p. 27). The hypothesis test is given in eq. 3.33.

$$\begin{aligned} H_0 &: \beta_j = 0 \\ H_1 &: \beta_j \neq 0 \end{aligned} \tag{3.33}$$

The null hypothesis is rejected when $|t_0| > t_{\alpha/2,n-k-1}$, suggesting that β_j is significant. The P-value approach suggests that the null hypothesis is rejected when the P-value of statistic $|t_0|$ is less then α. The t_0 statistics can be obtained by (Myers *et al.*, 2011, p. 28):

$$t_0 = \frac{b_j}{se(b_j)} \tag{3.34}$$

where b_j is the corresponding solution of the individual regression coefficient, of vector $\mathbf{b}$, where $\mathbf{b}$ can be obtained by eq. 3.17, and $se(b_j)$ is the standard error of the regression coefficient, as given by (Myers *et al.*, 2011, p. 28):

$$se(b_j) = \sqrt{MS_E\, C_{jj}} \tag{3.35}$$

where C_{jj} is the diagonal element of $(\mathbf{X}'\,\mathbf{X})^{-1}$ corresponding to b_j, where MS_E can be obtained in eq. 3.29.

3.6.3.4 Significance on Group of Coefficients

Sometimes it is useful in response surface methodology to test the significance of a group of variables, this is $x_1, x_2, \ldots, x_r$ where $r < k$, and k being the total number of model terms (Myers *et al.*, 2011, p. 29). It is commonly used to test the significance of a group of variables containing the same dimension (Myers *et al.*, 2011, p. 30), e.g. first-order terms, second order terms, etc. Let the $\boldsymbol{\beta}$ from eq. 3.14 be divided into two groups, $\boldsymbol{\beta_1}$ and $\boldsymbol{\beta_2}$; this is:

$$\boldsymbol{\beta} = \begin{bmatrix} \boldsymbol{\beta_1} \\ \boldsymbol{\beta_2} \end{bmatrix}, \tag{3.36}$$

where vector $\boldsymbol{\beta_1}$ is of dimension, $(r \times 1)$, and $\boldsymbol{\beta_1}$ has dimensions of $(p-r) \times 1$, where p is the total number of regression coefficients (Myers *et al.*, 2011, p. 29). Then the hypothesis test can be constructed to test the significance of $\boldsymbol{\beta_1}$:

$$\begin{aligned} H_0 &: \boldsymbol{\beta_1} = 0 \\ H_1 &: \boldsymbol{\beta_1} \neq 0 \end{aligned} \tag{3.37}$$

given that $\boldsymbol{\beta_2}$ is included into the model (Myers *et al.*, 2011, p. 29). The null hypothesis states that the $\boldsymbol{\beta_1}$ vector is significantly contributing towards the model. The alternative hypothesis states that the group of variables being

analysed, is insignificant. When F_0 exceeds $F_{\alpha,r,n-p}$ the null hypothesis is rejected, or alternatively with the P-value approach, H_0 is rejected when the P-value of statistic F_0 is less than α (Myers *et al.*, 2011, p. 30). Myers *et al.* (2011) provide the following formulation for calculating F_0 (Myers *et al.*, 2011, p. 29-30):

$$F_0 = \frac{SS_R(\boldsymbol{\beta_1} \mid \boldsymbol{\beta_2}) \,/\, r}{MS_E}, \tag{3.38}$$

where MS_E can be obtained from eq. 3.29, and

$$SS_R(\boldsymbol{\beta} \mid \boldsymbol{\beta_2}) = SS_R(\boldsymbol{\beta}) - SS_R(\boldsymbol{\beta_2}), \tag{3.39}$$

where

$$SS_R(\boldsymbol{\beta}) = \mathbf{b}'\,\mathbf{X}'\,\mathbf{y} \;\text{ and }\; SS_R(\boldsymbol{\beta_2}) = \mathbf{b_2}'\,\mathbf{X_2}'\,\mathbf{y}. \tag{3.40}$$

3.6.4 Confidence Intervals

Confidence intervals provide the range in which a specific variable or feature will fall into. The intervals are constructed based on the standard error associated with that specific term (Myers *et al.*, 2011, p. 31). The rest of this section will look at constructing confidence intervals on individual regression coefficients, confidence interval on mean response and confidence interval on predicted response.

3.6.4.1 On Individual Coefficients

The proceeding analyses assume that the statistical error is normal and independent distributed with a zero mean and variance σ^2, abbreviated as $\epsilon \sim NID(0, \sigma^2)$, so that the observations y_i are normally and independently distributed with a mean of $\beta_0 + \sum_{j=1}^{k} \beta_j\, x_{ij}$ (Myers *et al.*, 2011, p. 24). But first, the expected value of the residual sum of the squares is:

$$E(SS_E) = \sigma^2\,(n-p), \tag{3.41}$$

then the unbiased estimator of σ^2 becomes (Myers *et al.*, 2011, p. 23):

$$\hat{\sigma}^2 = \frac{SS_E}{n-p} = MS_E \tag{3.42}$$

where $(n-p)$ are the degrees of freedom of the residuals. Myers *et al.* (2011) provide the following equation to calculate the $100\,(1-\alpha)\,\%$ confidence interval on a single regression coefficient β_j, as (Myers *et al.*, 2011, p. 32):

$$b_j - t_{\alpha/2\,,n-p}\,\sqrt{\hat{\sigma}^2\,C_{jj}} \le \beta_j \le b_j + t_{\alpha/2\,,n-p}\,\sqrt{\hat{\sigma}^2\,C_{jj}}, \tag{3.43}$$

by using eq. 3.35 the confidence intervals for a single regression coefficient can be written as (Myers *et al.*, 2011, p. 32):

$$b_j - t_{\alpha/2\,,n-p}\,se(b_j) \le \beta_j \le b_j + t_{\alpha/2\,,n-p}\,se(b_j). \tag{3.44}$$

When a $95\,\%$ confidence interval is required, then α is chosen to be 0.05.

3.6.4.2 On Mean Response

Confidence intervals on the mean response can be obtained at each experimental trial. The design vector can be written as (Myers *et al.*, 2011, p. 33):

$$\mathbf{x}_i = \begin{bmatrix} 1 \\ x_{i1} \\ x_{i2} \\ \vdots \\ x_{ik} \end{bmatrix}, \tag{3.45}$$

which is obtained from the row number i corresponding to the experimental number of the model matrix $\mathbf{X}$; see eq. 3.14. The mean response can be obtained by (Myers *et al.*, 2011, p. 33):

$$\mu_{y|\mathbf{x}_i} = \beta_i + \beta_1 x_{11} + \beta_2 x_{22} + \cdots + \beta_k x_{1k} = \mathbf{x}_i' \mathbf{b}. \tag{3.46}$$

The estimated response at that point is (Myers *et al.*, 2011, p. 33):

$$\hat{y}(\mathbf{x}_i) = \mathbf{x}_i' \mathbf{b} \tag{3.47}$$

where the variance of $\hat{y}_i(\mathbf{x}_i)$ is (Myers *et al.*, 2011, p. 33):

$$\mathrm{Var}[\hat{y}(\mathbf{x}_i)] = \hat{\sigma}^2 \mathbf{x}_i' (\mathbf{X}'\mathbf{X})^{-1} \mathbf{x}_i. \tag{3.48}$$

Then the $100\,(1-\alpha)\,\%$ confidence interval on the mean response of the i'th experimental trial can be obtained by (Myers *et al.*, 2011, p. 34):

$$\hat{y}(\mathbf{x}_i) - t_{\alpha/2,\,n-p} \sqrt{\mathrm{Var}[\hat{y}(\mathbf{x}_i)]} \leq \mu_{y|\mathbf{x}_i} \leq \hat{y}(\mathbf{x}_i) + t_{\alpha/2,\,n-p} \sqrt{\mathrm{Var}[\hat{y}(\mathbf{x}_i)]}. \tag{3.49}$$

3.6.4.3 Prediction Interval

The regression model developed with RSM is often used to make future predictions at specific process conditions or experimental trials. It is benificial to construct the confidance interval for the predicted output when predictions are made. Myers *et al.* (2011) provide the following formulation:

$$\hat{y}(\mathbf{x}_i) - t_{\alpha/2,\,n-p} \sqrt{\hat{\sigma}^2 \left(1 + \mathbf{x}_i' (\mathbf{X}'\mathbf{X})^{-1} \mathbf{x}_i\right)} \leq \mu_{y|\mathbf{x}_i} \leq \\ \hat{y}(\mathbf{x}_i) + t_{\alpha/2,\,n-p} \sqrt{\hat{\sigma}^2 \left(1 + \mathbf{x}_i' (\mathbf{X}'\mathbf{X})^{-1} \mathbf{x}_i\right)} \tag{3.50}$$

to obtain the $100\,(1-\alpha)\,\%$ confidence interval for the predicted response of a given experimental trial $\mathbf{x}_i$ (Myers *et al.*, 2011, p. 35). The model vector $\mathbf{x}_i$ is obtained from the design matrix $\mathbf{X}$; see eq. 3.14 where i is the row number referring to the corresponding experimental trial number in the DOE.

3.6.5 Check Model Adequacy

It is always essential to check model assumptions and to establish whether the constructed model provides an adequate approximation of the true solution (Myers *et al.*, 2011, p. 36). The method of least squares assumes that the statistical error is normal and independent distributed with a zero mean and variance σ^2, abbreviated as $\epsilon \sim NID(0, \sigma^2)$, so that the observations y_i are normally and independently distributed with a mean of $\beta_0 + \sum_{j=1}^{k} \beta_j x_{ij}$ (Myers *et al.*, 2011, p. 24). This section will discuss the techniques suggested by Myers *et al.* (2011) to check model assumptions and to check whether the constructed model provides a satisfactory approximation of the true system.

3.6.5.1 Validate Model Assumptions

The least squares assumptions are examined through a residuals plot and Quantile - Quantile plot. Model adequacy is checked by examining the lack of fit test. The residuals are obtained through eq. 3.19 for each experimental trial where $e_i = y_i - \hat{y}_i$ as $i = 1, 2, \ldots, n$. From this the residual vs. predicted, and a quantile-quantile (QQ) plot thereof can be constructed. The normality assumption is approved when the data in the QQ-plot approximates a diagonal line. The proceeding assumptions are evaluated through residual vs. predicted plot and approved when the residuals have a constant spread (σ^2 is constant) about the zero mean (residuals independent of y_i).

3.6.5.2 Scaling Residuals

Different scaling approaches towards residuals exist. Some of these are standardised residuals and studentized residuals. The former is used to identify outliers, and the latter is used in the diagnostic plots to check model assumptions (Myers *et al.*, 2011, p. 38-39). The standardised residuals can be calculated by (Myers *et al.*, 2011, p. 38):

$$d_i = \frac{e_i}{\hat{\sigma}^2} \tag{3.51}$$

where e_i is the residual corresponding to the experimental trial number, $i = 1, 2, \ldots, n$, and $\hat{\sigma}^2$ is the residual mean square error; see eq. 3.29 and eq. 3.42. The standardised residuals falling outside, $-3 \leq d_i \leq 3$, are outliers (Myers *et al.*, 2011, p. 38). The studentized residuals can be obtained by (Myers *et al.*, 2011, p. 39):

$$r_i = \frac{e_i}{\sqrt{\hat{\sigma}^2 (1 - h_{ii})}} \tag{3.52}$$

as $i = 1, 2, \ldots, n$, and h_{ii} is diagonal elements of the hat matrix $\mathbf{H}$ where the hat matrix is obtained by (Myers *et al.*, 2011, p. 39):

$$\mathbf{H} = \mathbf{X} (\mathbf{X}'\mathbf{X})^{-1} \mathbf{X}' \mathbf{y}. \tag{3.53}$$

When the variance of studentized residuals $\text{Var}(r_i) = 1$ regardless of x_i, then the adequate model form is achieved (Myers *et al.*, 2011, p. 39). This makes it easier to detect when model assumptions are violated at remote locations in the data set (Myers *et al.*, 2011, p. 39). Compared to the variance of the residuals $\text{Var}(e_i) = \sigma^2 (1 - h_{ii})$, which is dependant on the location of x_i (Myers *et al.*, 2011, p. 39) has a tendency to be small at the outer edges of the data set, which may lead to misleading interpretations concerning model assumptions (Myers *et al.*, 2011, p. 39). Therefore, Myers *et al.* (2011) suggest using the studentized residuals when model assumptions are inspected.

3.6.5.3 Lack of Fit Test

The lack of fit test requires replicates of experimental trials. As discussed in section 3.2, the replicates are often conducted at the centre point of the design space where atleast three to five centre repeats are required. The addition of replicates to a DOE allows the error sum of squares to be subdivided into two major groups. These are the sum of squares due to lack of fit SS_{LOF}, and pure error sum of squares SS_{PE}; mathematically this is (Myers *et al.*, 2011, p. 44):

$$SS_E = SS_{PE} + SS_{LOF} \tag{3.54}$$

where (Myers *et al.*, 2011, p. 45)

$$SS_{PE} = \sum_{i=1}^{m} \sum_{j=1}^{n_i} (y_{ij} - \bar{y}_i)^2 \tag{3.55}$$

and (Myers *et al.*, 2011, p. 45)

$$SS_{LOF} = \sum_{i=1}^{m} n_i (\bar{y}_i - \hat{y}_i)^2 \tag{3.56}$$

where n_i is the number of replicates at a specific experimental trial point x_i for $i = 1, 2, \ldots, m$, and m is the number of distinct points in the DOE. Also, y_{ij} is the observation at x_i, for $i = 1, 2, \ldots, m$, as $j = 1, 2, \ldots, n$, where n is the total number of observations including the replicates, therefore $n > m$. Also, $\bar{y}_i$ is the mean of the observations at trial number i and $\hat{y}_i$ is the predicted response at trial number i. The lack of fit test regime establishes whether the appropriate model curvature is achieved. The appropriate hypothesis test for lack of fit is given by Myers *et al.* (2011) to be:

$$\begin{aligned} H_0 &: \text{Model is adequate to describe data} \\ H_1 &: \text{Model is inadequate to describe system} \end{aligned} \tag{3.57}$$

where the null hypothesis is rejected when F_0 exceeds $F_{\alpha, m-p, n-m}$ or alternatively with the P-value approach, H_0 is rejected when the P-value of statistic

F_0 is less then α (Myers *et al.*, 2011, p. 46). When the null hypothesis is rejected, strong evidence exists against model adequacy (Myers *et al.*, 2011, p. 46). Statistic F_0 can be calculated by:

$$F_0 = \frac{SS_{LOF}/(m-p)}{SS_{PE}/(n-m)} = \frac{MS_{LOF}}{MS_{PE}} \tag{3.58}$$

where SS_{LOF} is the lack of fit sum of squares and SS_{PE} is the sum of squares of the pure error. The former has $(m-p)$ degrees of freedom and the latter has $(n-m)$ degrees of freedom. However, accepting H_0 does not necessarily imply that the model is significant (Myers *et al.*, 2011, p. 46) since the range of possible predicted values should be larger than the standard error. If not, the model is fitted to noise instead and not to the true response (Myers *et al.*, 2011, p. 46).

Chapter 4

Results and Discussion

This chapter provides the results and discussion of the Response Surface Methodology (RSM) approach. The discussion includes the screening experiments, followed by the second phase which entails establishing the significant variables and identifying the adequate model equation. During model selection, additional approaches are used in conjunction with linear regression. These are a stepwise regression, Bayesian information criterion (BIC) and robust regression. Once a satisfying model is obtained, validations tests are conducted, followed by optimisation of the response surface with a discussion of the findings.

4.1 Phase Zero and One: Screening Experiments

The screening experiments seek to establish the adequate design space of the process variables, which should contain the process optimum. The most common film to fitment layout at ALC makes use of two plies of 100 µm LDPE film, welded on a 2 inch hex gland; see Appendix B. Therefore, all preliminary tests were conducted with a similar layout. During the execution of the preliminary tests, the process variables were changed according to the DOE provided in Table A.4 of Appendix A.1.4 where factors A, B and C correspond to the process variables of the seal heat head, which is temperature, pressure and dwell time. Table 4.1 provides the design space of the process variables for the preliminary tests, where the lower boundary, midpoint and upper boundary, respectively, refer to the coded variables of the DOE, -1, 0 and 1. Since the midpoint represents the operating process point at the time for ALC, it was used as a guideline to estimate the design region for the first model iteration.

Once the DOE was in place, the gland seals were produced accordingly, followed by sample cutting, uniaxial tensile testing, data processing and finally, data analysing. This process was outlined and discussed in Chapter 3. The statistical analyses were performed in *R*-statistic, where the Response Surface

Methodology approach was followed, as outlined in section 3.6.

Table 4.1: Defined range of process parameters for preliminary model.

Variable	Lower Boundary	Mid Point	Upper Boundary
Temperature	205 °C	255 °C	305 °C
Pressure	8 bar	9 bar	10 bar
Dwell Time	3.3 sec	6.3 sec	9.3 sec

The first model equation iteration was constructed based upon the preliminary test results, where the method of linear regression was used. Section 3.6.2 describes the construction of a model equation based upon linear regression. The resulted model equation took the form of:

$$\begin{aligned}\hat{y}_{ts} =&\beta_0 + \beta_1 x_1 + \beta_2 x_2 + \beta_3 x_3 + \beta_{12} x_1 x_2 \\ &+ \beta_{13} x_1 x_3 + \beta_{23} x_2 x_3 + \beta_{11} x_1^2 + \beta_{22} x_2^2 + \beta_{33} x_3^2\end{aligned} \tag{4.1}$$

where $\hat{y}_{ts}$ is the predicted failure stress based upon the process variables, in terms of the coded scheme. The coded variables x_1, x_2 and x_3 refer to the process variables, temperature, pressure and dwell time respectively where eq. 3.9 is used to transform the coded scheme x_n to the natural scheme ξ_n. The coded scheme is dimensionless and the natural scheme is in terms of the natural units of the input variables. As mentioned before, the DOEs are given in terms of the coded scheme, therefore A, B and C refer to x_1, x_2 and x_3 respectively in the DOE; see Table A.4.

The summary of the statistical analysis is provided in Table 4.2. The table provides the summary of fit, parameter estimates and the analysis of variance of the initial model estimation. The coefficients of the model terms are provided in the second column of the parameter estimate section of the table. These can be inserted into eq. 4.1 to give:

$$\begin{aligned}\hat{y}_{ts} =&16.045 + 2.54 x_1 + 0.902 x_2 + 2.188 x_3 - 1.48 x_1 x_2 \\ &- 1.68\, x_1 x_3 - 1.587 x_2\, x_3 - 0.835 x_1^2 - 3.035 x_2^2 - 0.199 x_3^2.\end{aligned} \tag{4.2}$$

Section 3.6.3.3 describes the test procedure for establishing whether an individual coefficient is significant. The hypothesis test is outlined in eq. 3.33, where the null hypothesis is rejected when $|t_0| > t_{\alpha/2,n-k-1}$, indicating that β_j is significant. Concerning the preliminary model, $t_{\alpha/2,n-k-1} = t_{0.05/2,145-10} = 1.978$, where n is the total number of samples tested, $k - 1 = p$ is the number of coefficients in the model equation and α is chosen to be 0.05 % in common

practice. The t-value can then be obtained from a t-statistics table. Alternatively, the null hypothesis is rejected when the P-value of statistic $|t_0|$ is less then α. Now, consider Table 4.2. All variables are significant except for x_3^2, since $0.524 < 1.978$ or alternatively the P-value approach, $0.60108 > 0.05$. As a result, x_3^2 can be eliminated from the model equation without sacrificing accuracy.

The analysis of variance provides insight into the significance of a group of variables. Section 3.6.3.4 outlines the hypothesis test concerning the significance of a group of variables, where the null hypothesis in eq. 3.37 is rejected when the P-value of statistic F_0 is less then $\alpha = 0.05$. From Table 4.2 in the analysis of variance section, the P-value of statistic P_0 for the first order (FO), two way interaction (TWI) terms, and pure quadratic (PQ) terms are all $< 2.2 \times 10^{-16}$, being less than $\alpha = 0.05$ suggests that the null hypothesis in eq. 3.37 is rejected for all. This concludes that first order, interaction and quadratic terms are significant and required in the model equation.

However, the hypotheses tests can only be accepted when all model assumptions are met. This is, statistical error is normal and independent distributed with a zero mean and variance σ^2, abbreviated as $\epsilon \sim NID(0, \sigma^2)$, so that the observations y_i are normally and independently distributed with a mean of $\beta_0 + \sum_{j=1}^{k} \beta_j x_{ij}$ (Myers *et al.*, 2011, p. 24). These assumptions are evaluated through visual inspection of a quartile-quartile plot and a residual plot. These two graphs are depicted in Fig. 4.1 for the preliminary tests. Fig. 4.1a displays the QQ-plot of the residual data, normality about a zero mean is met when the data approaches the diagonal line as shown in the figure.

The proceeding model assumptions are evaluated through the residual plot; see Fig. 4.1b. The figure displays the standardised residuals, obtained through eq. 3.51 vs. the predicted stress values corresponding to the trial runs of the DOE. Since no standardised residuals fall outside, $-3 \leq d_i \leq 3$, no outliers are detected within the cluster of data points. The least squares assume that the residuals are independent of the predictions, with a constant variance. The former is true when the centre of each cluster of points falls on the zero mean; this is, there is no noticeable trend in the residuals vs. predicted results. The latter requires that the residuals have a constant spread about the zero mean. Both assumptions are violated in Fig. 4.1b at the outer edges of the predictions. However, satisfactory results are obtained between 12 MPa and 14 MPa.

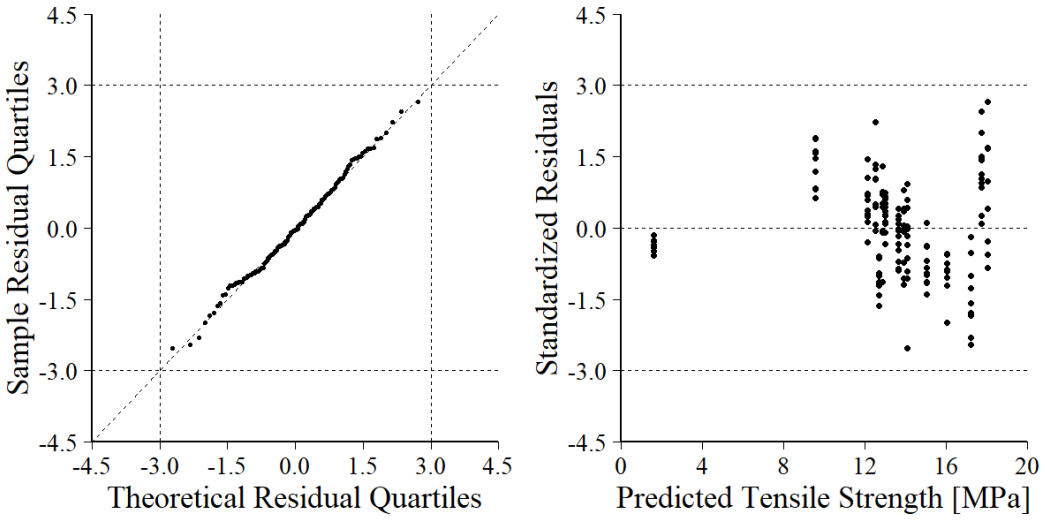

(a) Residual Quartile-Quartile Plot (b) Standardised Residual Analysis

Figure 4.1: Normality test and residual analysis of preliminary model. The sample residual quantiles should follow the diagonal line in the Quantile - Quantile (QQ) plot to prove normality, as proven in case of Figure 4.1a. The standardised residuals analysis is displayed in Fig. 4.1b where the least squares assumptions are violated at the outer edges of the predictions.

Due to the deviation from the actual response at the outer edges, the model suffers from a lack of fit. This is illustrated by the hypothesis test outlined in section 3.6.5.3. This is the null hypothesis in eq. 3.57 is rejected when the P-value of statistic F_0 is less then α. From Table 4.2 the analysis of variance is provided, where the probability of F_0 being larger than $F_{\alpha,m-p,n-m}$, is $< 2.2 \times 10^{-16}$, which is less than $\alpha = 0.05$. Therefore the null hypothesis is rejected in eq. 3.57, suggesting that the model suffers from a lack of fit. As a result, unaccounted variance exists which shows up in the R-square and R-squared adjusted values. See summary of fit section of Table 4.2, where $R^2 = 0.804$ and $R^2_{adj} = 0.792$ which suggests that the model only accounts for about 80 % of the total variance.

The latter part of section 3.6.3 outlines the significance of both variables. The R-square and R-squared adjusted variables can respectively be obtained through eq. 3.27 and eq. 3.28. Where R^2 increases even if unnecessary terms are added to the model, as a result R^2_{adj} is used in conjunction, which decreases when unnecessary terms are added. Therefore, when $R^2_{adj} \approx R^2$ then the value of R^2_{adj} can be used to describe the amount of variance accounted for by the model. From eq. 3.27 and eq. 3.30 the unaccounted variance is due to the residual sum of squares SS_E, where SS_E consists of the pure error sum of squares SS_{PE} and lack of fit sum of squares SS_{LOF}; see equation eq. 3.54.

The SS_{PE} term is due to the variance between the observed response and the mean of the replicates at that specific DOE point; see eq. 3.55. This is why replicates are useful during the construction of a DOE, which is to measure the variance induced between experimental trials. The lack of fit sum of squares SS_{LOF} is obtained through the variance between the predicted and mean response; see eq. 3.56. Therefore, the unaccounted variance can be reduced by either limiting the variance induced between experimental trials or by improving the model fit.

The corresponding sum of square values is provided in the analysis of variance section of Table 4.2 for the preliminary model. This provides useful insight into the relative contribution of the model terms towards the total variance and the lack of variance due to the error terms. The total variance accounted for by the regression model is $SS_R = 1342.35 + 595.65 + 426.72 = 2364.72$, and the unaccounted variance is $SS_E = SS_{PE} + SS_{LOF} = 210.92 + 366.2 = 577.12$. From Table 4.2, $(1342.35/2364.72) \times 80.4\,\% = 45.64\,\%$ of the 80.4% is accounted by the first order terms, 20.25 % is accounted by the interaction terms and the proceeding 14.43 % of the 80.4% is accounted by the quadratic terms. Now concerning the unaccounted variance, 7.16 % of the 19.6 % unaccounted variance is due to error induced between trial runs, and the proceeding 12.44 % is due to lack of fit.

In summary, the preliminary model was constructed over the design space as outlined in Table 4.1. The least squares assumptions were violated at the outer edges of the predictions. Since the resolution of the data was low between the outer and inner regions, the model was not able to capture the curvature in these regions. As a result, a lack of fit existed in these regions. However, the generated model accounted 80.4 % of the total variance. The proceeding unaccounted variance is due to lack of fit, 12.44 %, and due to experimental error, 7.16 %. As a result, the model was regarded as insignificant by the lack of fit hypothesis test outlined in section 3.6.5.3. An eigenvalue analysis in R-statistic has shown that the stationary point provided in Table 4.2 is an optimum. However, it falls outside the current design space; see 4.1. Therefore, the design space for the next model iteration should provide better resolution at the outer regions, where the optimum conditions should lie within the design space of the model. Additionally, the next model iteration will seek to minimise the error terms as discussed above, to establish a significant model.

Table 4.2: Regression output from *R*-Statistic (i386 3.2.5) of preliminary model, corresponding to eq. 4.1 for failure stress. The *t*-statistic values test for significance of individual coefficients where the *F*-statistic values test for significance of a group of coefficients. The appropriate hypothesis tests are outlined in the preceding sections. The *R*-square adjusted value represents the amount of variance accounted for of the total variance.

Summary of Fit				
R-Square	0.804			
R-Square Adjusted	0.792			
Parameter Estimates				
Term	Coefficient	Std Error	t_0	Prob ($>\|t\|$)
Intercept	16.045	0.340	47.236	$< 2.2 \times 10^{-16}$
x_1	2.540	0.197	12.922	$< 2.2 \times 10^{-16}$
x_2	0.902	0.197	4.569	1.04×10^{-5}
x_3	2.188	0.197	11.114	$< 2.2 \times 10^{-16}$
x_1x_2	-1.480	0.222	-6.674	4.90×10^{-10}
x_1x_3	-1.680	0.222	-7.568	4.03×10^{-12}
x_2x_3	-1.587	0.222	-7.152	3.89×10^{-11}
x_1^2	-0.835	0.380	-2.193	0.02984
x_2^2	-3.035	0.381	-7.957	4.62×10^{-13}
x_3^2	-0.199	0.381	-0.524	0.60108
Analysis of Variance				
Source	DF	Sum of Squares	Mean Square	Prob ($>F$)
FO Terms	3	1342.35	447.45	$< 2.2 \times 10^{-16}$
TWI Terms	3	595.65	198.55	$< 2.2 \times 10^{-16}$
PQ Terms	3	426.72	142.24	$< 2.2 \times 10^{-16}$
Residuals	145	577.12	3.98	
Lack of Fit Total	5	366.20	73.24	$< 2.2 \times 10^{-16}$
Pure Error	140	210.92	1.51	
Stationary Point				
Variable Regime	Temperature	Pressure	Dwell Time	Prediction
Coded	1.513	−0.289	0.263	18.12 MPa
Natural	333.66 °C	7.71 bar	7.09 sec	18.12 MPa

4.2 Second Phase

As outlined in the previous section, the objectives of the second model iteration are to improve upon the preliminary model, where better data resolution was required with an update on the design space to include the optimum seal strength conditions, while all least square assumptions are met. Also, reducing the variance induced by the error terms so that the model equation will yield to be significant.

A new DOE was constructed to capture the adequate response curvature of the seal tensile strength. The new design makes use of a face-centred design in conjunction with a central composite design. The two designs are fused to provide higher resolution between the centre points and outer regions of the design space. The corresponding design matrix and design space are provided in Table A.5 and Table 4.3 respectively, the coded variables are related to the natural variables as provided. The centre point was shifted to a higher temperature, lower pressure and lower dwell time. The temperature boundaries were also adjusted to include the possible optimum, as predicted from the preliminary model.

During the sealing process, the gland seals were produced starting from the highest temperature and ending with the lowest temperature setting specified by the DOE. Besides from this, the trial runs were randomised to reduce any systematic error.

Table 4.3: Defined Range of Process Parameters: Second Model Iteration

	Coded Variable				
Natural Variable	-1.68	-1	0	1	1.68
Temperature	216.2 °C	240 °C	280 °C	320 °C	343.8 °C
Pressure	4.4 bar	5 bar	6 bar	7 bar	7.6 bar
Dwell Time	2.1 sec	3 sec	4.5 sec	6 sec	6.9 sec

A full second order model equation was constructed from the new tests data consisting of four variables. These are the heat head temperature, actuator pressure, dwell time and perimeter angle position of where the samples were cut from. The perimeter position was inserted in the model equation as an attempt to model the geometric variances between replicate trial runs. The resulted model equation took the form of:

$$\begin{aligned}\hat{y}_{ts} =& \beta_0 + \beta_1 x_1 + \beta_2 x_2 + \beta_3 x_3 + \beta_4 x_4 \\ &+ \beta_{12} x_1 x_2 + \beta_{13} x_1 x_3 + \beta_{14} x_1 x_4 + \beta_{23} x_2 x_3 \\ &+ \beta_{24} x_2 x_4 + \beta_{34} x_3 x_4 + \beta_{11} x_1^2 + \beta_{22} x_2^2 + \beta_{33} x_3^2 + \beta_{44} x_4^2.\end{aligned} \tag{4.3}$$

Table 4.4: Regression output from *R*-Statistic (i386 3.2.5) of second model iteration, corresponding to eq. 4.3. The *t*-statistic values test for significance of individual coefficients where the *F*-statistic values test for significance of a group of coefficients. The appropriate hypothesis tests are outlined in the preceding sections. The *R*-square adjusted value represents the amount of variance accounted for of the total variance.

Summary of Fit	
R-Square	0.9088
R-Square Adjusted	0.8797

Parameter Estimates

Term	Coefficient	Std Error	*t*-value	Prob ($>\|t\|$)
Intercept	17.1187	0.213274	80.2664	$< 2.2 \times 10^{-16}$
x_1	1.349496	0.118091	11.4276	9.31×10^{-15}
x_2	−0.25474	0.130356	−1.9542	0.057053
x_3	1.221552	0.117494	10.3967	1.99×10^{-13}
x_4	0.097345	0.159312	0.611	0.544322
x_1x_2	−0.48744	0.154445	−3.1561	0.002884
x_1x_3	−1.11169	0.154799	−7.1815	6.20×10^{-9}
x_1x_4	−0.15482	0.181654	−0.8523	0.398681
x_2x_3	−0.75472	0.153235	−4.9252	1.23×10^{-5}
x_2x_4	0.282048	0.21521	1.3106	0.196802
x_3x_4	−0.12131	0.18453	−0.6574	0.514358
x_1^2	−0.60811	0.133117	−4.5682	3.96×10^{-5}
x_2^2	0.703837	0.150902	4.6642	2.90×10^{-5}
x_3^2	−0.75021	0.124469	−6.0273	3.08×10^{-7}
x_4^2	−0.03061	0.307091	−0.0997	0.921066

Analysis of Variance

Source	DF	Sum of Squares	Mean Square	Prob ($> F$)
FO	4	135.529	33.882	$< 2.2 \times 10^{-16}$
TWI	6	47.27	7.878	1.34×10^{-9}
PQ	4	34.934	8.733	1.10×10^{-8}
Residuals	44	21.861	0.497	
Lack of fit	37	14.096	0.381	0.9843
Pure error	7	7.765	1.109	

The statistical analysis of the new model equation is provided in Table 4.4. Section 3.6.3.3 provides the hypothesis test concerning the significance of an individual coefficient; see eq. 3.33. The P-value approach suggests that the null hypothesis is rejected when the P-value of statistic $|t_0|$ is less then $\alpha = 0.05$. This is, all model terms in Table 4.4 are significant when the probability ($> |t|$) values are less than 0.05, and insignificant when the probability ($> |t|$) values exceed 0.05. From this, it can be seen that all terms containing x_4 are insignificant.

However, the t-statistic is dependant on the number of regression coefficients. Therefore cross-validating techniques are used to ensure that the adequate terms are eliminated. One such method is stepwise regression (Mason *et al.*, 1989, p. 572). The backward stepwise regression starts off with the full model equations, e.g. as provided in eq. 4.3, then it eliminates stepwise the insignificant coefficients until the remaining coefficients are significant (Mason *et al.*, 1989, p. 574). This was performed in R-studio, which also yielded that all terms containing x_4 are insignificant.

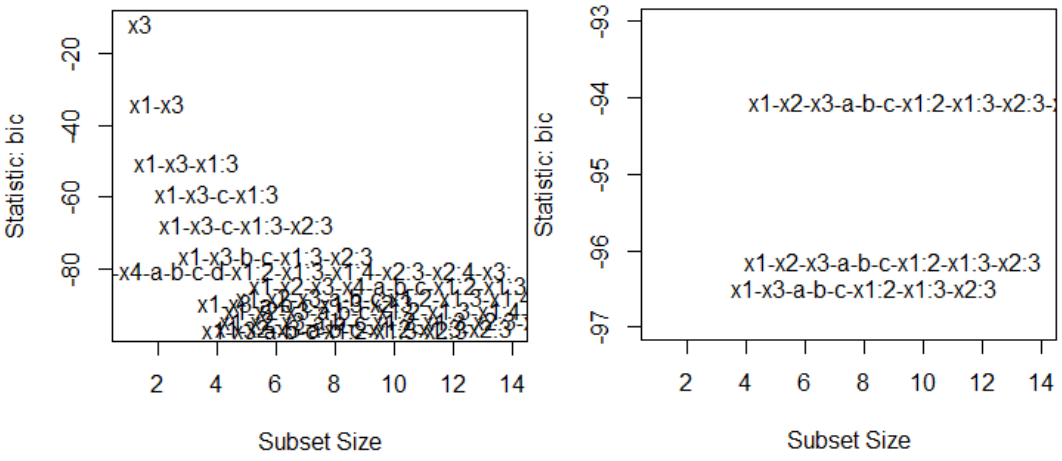

(a) Full Analysis (b) Zoomed Analysis

Figure 4.2: Model Selection: The Bayesian criterion (BIC) analysis was performed in R-studio on all model term combinations of eq. 4.3. The BIC value for the best model combination at specific subset size is plotted; subset size being the number of regression coefficients.

Additionally, the Bayesian information criterion (BIC) can be used for model selection (Schwarz *et al.*, 1978). It makes use of the maximum likelihood principle, in conjunction with penalising larger dimensioned models, in an attempt to prevent overfitting (Schwarz *et al.*, 1978). This criterion was performed on all possible model combinations, based upon the regression coefficients outlined in eq. 4.3, and the results are displayed in Fig 4.2. The lowest BIC value indicates the best trade-off between model fit and model simplicity.

Fig. 4.2a displays the full analysis where the increasing model size reduces the BIC value. However, a turning point is reached where ongoing model expansion increases the BIC value. Fig. 4.2b displays the turning point with higher resolution. The a, b and c variables refer to x_1^2, x_2^2 and x_3^2 respectively. The analysis indicates that the best model candidate excludes all regression terms containing x_4, and β_2 from eq. 4.3. However, eliminating $\beta_2 x_2$ from the model equation reduces the accuracy of fit. Therefore the linear combination of x_2 is kept since sufficient experimental resolution is available to compute β_2 when higher order combinations of x_2 are included in the model, and including $\beta_2 x_2$ has little effect on the BIC value.

All the analyses above concluded that the model terms containing x_4 are insignificant, suggesting that the seal strength is independent of the perimeter position. Therefore, x_4 is excluded from the model. Then, eq. 4.3 is reduced to:

$$\begin{aligned}\hat{y}_{ts} =&\beta_0 + \beta_1 x_1 + \beta_2 x_2 + \beta_3 x_3 + \beta_{12} x_1 x_2 \\ &+ \beta_{13} x_1 x_3 + \beta_{23} x_2 x_3 + \beta_{11} x_1^2 + \beta_{22} x_2^2 + \beta_{33} x_3^2.\end{aligned} \tag{4.4}$$

The statistical analysis corresponding to eq. 4.4 is provided in Table 4.5. From this, the model equation can be written in terms of the coded regime:

$$\begin{aligned}\hat{y}_{ts} =&17.101 + 1.326 x_1 - 0.223 x_2 + 1.232 x_3 - 0.515 x_1 x_2 \\ &- 1.104 x_1 x_3 - 0.75 x_2 x_3 - 0.592 x_1^2 + 0.696 x_2^2 - 0.742 x_3^2.\end{aligned} \tag{4.5}$$

The transformation between the coded and natural regime is accomplished by using eq. 3.9 in conjunction with the model design space, as provided in Table 4.3; this is:

$$x_1 = \frac{T - 280}{40},\ x_2 = \frac{P - 6}{1},\ \text{and}\ x_3 = \frac{t - 4.5}{1.5} \tag{4.6}$$

where T is the heat head temperature (°C), P is the pneumatic pressure (bar) and t is the process dwell time (sec). The QQ-plot and residual analysis graphs are depicted in Fig. 4.3. The normality assumption is met in the QQ-plot since the residual quartiles approximate the diagonal line as shown in Fig. 4.3a. The proceeding least square assumptions are analysed in Fig. 4.3b. It displays the standardised residuals vs. the predicted seal tensile strength. Compared to the residual analysis of the preliminary model, the new model approximates the least square assumptions better. This means the residuals are independent of the predicted values and are distributed with a constant variance about the zero mean. As a result, the latter model accounts for more variance than the preliminary model. Also note, since no standardised residuals fall outside $-3 \leq d_i \leq 3$, no outliers are detected within the cluster of data points. Although one point nearly lies at $d_i = 3$, it still lies within the boundaries, therefore it is kept part of the dataset.

Table 4.5: Regression output from *R*-Statistic (i386 3.2.5) of second model iteration without perimeter position, corresponding to eq. 4.4. The *t*-statistic values test for significance of individual coefficients where the *F*-statistic values test for significance of a group of coefficients. The appropriate hypothesis tests are outlined in the preceding sections. The *R*-square adjusted value represents the amount of variance accounted for of the total variance.

Summary of Fit	
R-Square	0.9018
R-Square Adjusted	0.8837

Parameter Estimates

Term	Coefficient	Std Error	*t*-value	Prob ($>\|t\|$)
Intercept	17.10127	0.16723	102.2633	$< 2.2 \times 10^{-16}$
x_1	1.3258	0.11386	11.644	1.02×10^{-15}
x_2	−0.22295	0.12473	−1.7876	0.080032
x_3	1.23152	0.11356	10.8444	1.28×10^{-14}
x_1x_2	−0.51529	0.1504	−3.4261	0.001248
x_1x_3	−1.10373	0.15047	−7.3353	2.01×10^{-9}
x_2x_3	−0.74974	0.15017	−4.9925	7.94×10^{-6}
x_1^2	−0.59225	0.12913	−4.5864	3.14×10^{-5}
x_2^2	0.69555	0.14676	4.7395	1.88×10^{-5}
x_3^2	−0.7415	0.1219	−6.0826	1.75×10^{-7}

Analysis of Variance

Source	DF	Sum of Squares	Mean Square	Prob ($> F$)
FO	3	133.887	44.629	$< 2.2 \times 10^{-16}$
TWI	3	47.754	15.918	7.55×10^{-12}
PQ	3	34.419	11.473	1.14×10^{-9}
Residuals	49	23.534	0.48	
Lack of fit	11	8.854	0.805	0.04643
Pure error	38	14.679	0.386	

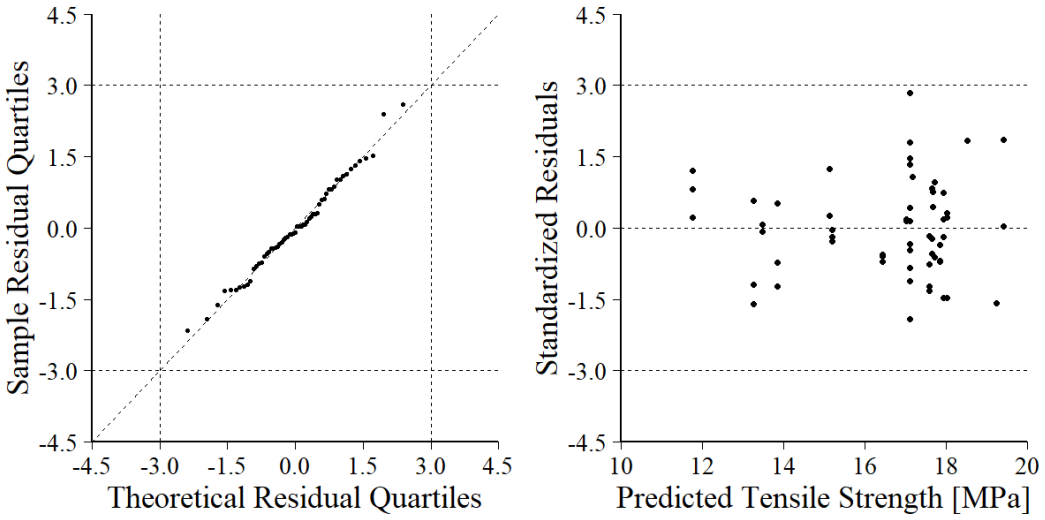

(a) Residual Quartile-Quartile Plot (b) Standardised Residual Analysis

Figure 4.3: The consecutive graphs are based upon the second model iteration, as provided in eq. 4.5. The sample residual quantiles should follow the diagonal line in the Quantile - Quantile plot to prove normality, as proven in case of Figure 4.3a. The standardised residuals analysis is displayed in Fig. 4.3b, where the least squares assumptions are met.

Table 4.5 provides the summary of fit of the new model, where $R^2 = 0.9018$ and $R^2_{adj} = 0.8837$. This suggests that the new model accounts for about 88 % of the total variance, which is ±8 % improvement on the preliminary model. This was achieved by the improved DOE, which provided higher resolution to capture the true response. As a result, the lack of fit was reduced. The P-value of statistic F_0 is 0.04643, is less than $\alpha = 0.05$, suggesting evidence of lack of fit exists. However, this is nearly on the border of being significant, thus a major improvement was achieved from the preliminary model where the P-value of statistic F_0 was $< 2.2 \times 10^{-16}$.

In a attempt to reduce the lack of fit, the model equation can be transformed where the model transformation takes the form of $\hat{y}^{\lambda}$. In general, power transformations seek three main objectives, this is to stabilise the variance of the response, improve normality of the residuals, and reduce the lack of fit (Myers *et al.*, 2011, p. 60). This procedure is called the Box-Cox transformation and is implemented in R-statistic where it seeks to find the maximum likelihood of λ to minimise the residual sum of squares SS_E (Myers *et al.*, 2011, p. 61). The Box-Cox analysis was performed on eq. 4.5, and the corresponding output from R-statistic is displayed in Fig. B.8. The figure displays the 95 % confidence interval on the value of λ which will minimise SS_E. Myers *et al.* (2011) suggest using a transformation which can easily be implemented

without sacrificing accuracy (Myers *et al.*, 2011, p. 62). For instance the ideal solution is shown in Fig. B.8 to be where $\lambda = -0.3$. However, $\lambda = 0$ is the more practical choice which still falls within the 95 % confidence interval. The model equation is then transformed through the natural logarithmic when $\lambda = 0$ (Myers *et al.*, 2011, p. 61). Then, eq. 4.4 becomes:

$$\begin{aligned}\ln(\hat{y}_{ts}) =& \beta_0 + \beta_1 x_1 + \beta_2 x_2 + \beta_3 x_3 + \beta_{12} x_1 x_2 \\ &+ \beta_{13} x_1 x_3 + \beta_{23} x_2 x_3 + \beta_{11} x_1^2 + \beta_{22} x_2^2 + \beta_{33} x_3^2,\end{aligned} \tag{4.7}$$

which simplifies to:

$$\hat{y}_{ts} = e^{\beta_0+\beta_1 x_1+\beta_2 x_2+\beta_3 x_3+\beta_{12} x_1 x_2+\beta_{13} x_1 x_3+\beta_{23} x_2 x_3+\beta_{11} x_1^2+\beta_{22} x_2^2+\beta_{33} x_3^2}. \tag{4.8}$$

A BIC analysis was performed on the transformed model equation. The results are depicted in Fig. 4.4. The same finding can be concluded as before. This is, $\beta_2 x_2$ is included with little expense, therefore eq. 4.8 becomes the solution. When compared to Fig. 4.2, the BIC analysis on the transformed model equation yielded to lower values which suggest that for the same variable dimensionality the transformation yielded to a better fit.

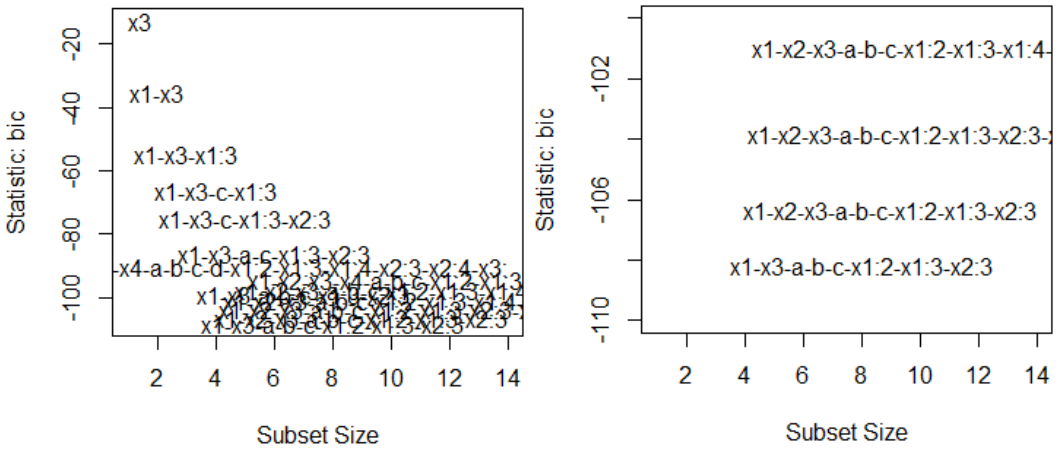

(a) Full Analysis (b) Zoomed Analysis

Figure 4.4: Model Selection: The Bayesian criterion (BIC) analysis was performed in R-studio on all model term combinations of the natural logarithmic transformation of eq. 4.3. The a, b and c variables respectively refer to x_1^2, x_2^2 and x_3^2.

Table 4.6: Regression output from *R*-Statistic (i386 3.2.5) of transformed model equation, corresponding to eq. 4.7. The *t*-statistic values test for significance of individual coefficients where the *F*-statistic values test for significance of a group of coefficients. The appropriate hypothesis tests are outlined in the preceding sections. The *R*-square adjusted value represents the amount of variance accounted for of the total variance.

Summary of Fit	
R-Square	0.9174
R-Square Adjusted	0.9022

Parameter Estimates

Term	Coefficient	Std Error	*t*-value	Prob ($>\|t\|$)
Intercept	2.83886	0.009883	287.2543	$< 2.2 \times 10^{-16}$
x_1	0.084656	0.006729	12.581	$< 2.2 \times 10^{-16}$
x_2	−0.01014	0.007371	−1.3762	0.175018
x_3	0.080988	0.006711	12.0674	2.75×10^{-16}
x_1x_2	−0.03259	0.008888	−3.6663	0.000605
x_1x_3	−0.0755	0.008892	−8.4903	3.43×10^{-11}
x_2x_3	−0.04565	0.008875	−5.1435	4.72×10^{-6}
x_1^2	−0.03898	0.007631	−5.1072	5.35×10^{-6}
x_2^2	0.040193	0.008673	4.6343	2.68×10^{-5}
x_3^2	−0.05033	0.007204	−6.9861	6.97×10^{-9}

Analysis of Variance

Source	DF	Sum of Squares	Mean Square	Prob ($> F$)
FO	3	0.56231	0.187437	$< 2.2 \times 10^{-16}$
TWI	3	0.20622	0.068741	2.12×10^{-13}
PQ	3	0.14384	0.047947	7.88×10^{-11}
Residuals	49	0.08219	0.001677	
Lack of fit	11	0.02953	0.002685	0.06487
Pure error	38	0.05266	0.001386	

The statistical analysis was performed on the transformed model equation and the subsequent results are provided in Table 4.6. From this the coefficients can be inserted into eq. 4.8 to give:

$$\hat{y}_{ts} = e^{2.84+0.085x_1-0.01x_2+0.081x_3-0.033x_1x_2-0.075x_1x_3-0.046x_2x_3-0.039x_1^2+0.04x_2^2-0.05x_3^2}. \tag{4.9}$$

As before, the natural variables are related to the coded variables through eq. 4.6 and are used in conjunction with eq. 4.9 to make predictions.

Apart from the linear least squares approach, robust regression can be performed to estimate the regression coefficients. With the least squares approach, the model equation is highly influenced by outliers (Mason *et al.*, 1989, p. 593). Robust regression however, minimises the influence of outliers (Mason *et al.*, 1989, p. 593). Ideally, the solution produced by robust regression should approximate the least squares solution in the absence of contaminated data. Robust regression was performed in R-studio on the model equation provided in eq. 4.8, and the generated solution in the coded regime took the form of:

$$\hat{y}_{ts} = e^{2.83+0.084x_1-0.01x_2+0.079x_3-0.032x_1x_2-0.076x_1x_3-0.046x_2x_3-0.037x_1^2+0.04x_2^2-0.044x_3^2} \tag{4.10}$$

where the natural variables are related to the coded variables through eq. 4.6. The solution provided above is nearly identical to the solution produced by the linear least squares approach; see eq. 4.9 which cross validates the estimates of the regression variables, confirming both solutions to be feasible.

The corresponding QQ-plot and residual analysis are displayed in Fig. 4.5. The normality assumption is met, where the residual quartiles approximate the diagonal line. The transformation yielded a model that approximates the least squares assumption better than the prior model. The standardised residuals are better distributed about the zero mean and with careful inspection, the variance about the zero mean are more uniform than before. This can be seen by comparing Fig. 4.5b with Fig. 4.3b. As a result, the lack of fit was reduced. This can be proven through the hypothesis test outlined in section 3.6.5.3. Since the P-value of statistic F_0 in Table 4.6, 0.06487 is greater then $\alpha = 0.05$ the alternative hypothesis in eq. 3.57 is rejected, accepting H_0, suggesting there is no strong evidence of lack of fit. Additionally, the variance of the studentized residuals was calculated from eq. 3.52 to be $\text{Var}(r_i) = 1.031 \simeq 1$, as a result the form of the model is correct (Myers *et al.*, 2011, p. 39).

Fig. 4.6 displays the actual vs. predicted response during the training phase of the model equation provided in eq. 4.9. Ideally, the mean of the data points should follow the diagonal line, as shown in the figure where the solid black line, being the mean of the observations, falls directly on the dashed diagonal line. Section 3.6.4.2 outlines the procedure of obtaining the $100(1-\alpha)\,\%$ confidence interval about the mean response, since $\alpha = 0.05$ the confidence

interval becomes 95 %. The confidence interval on the mean response is displayed through the grey region in Fig. 4.6, which suggests that the model has 95 % confidence that the population mean falls within this region. Since this region follows the diagonal line, satisfactory results were obtained.

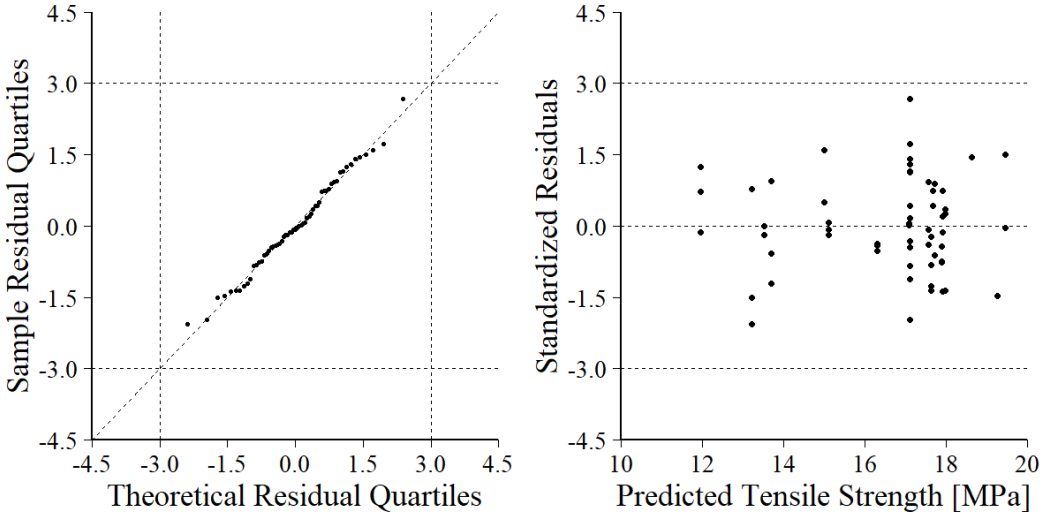

(a) Residual Quartile-Quartile Plot (b) Standardised Residual Analysis

Figure 4.5: The consecutive graphs are based upon a transformation of the second model iteration, as provided in eq. 4.9. The sample residual quantiles should follow the diagonal line in the Quantile - Quantile plot to prove normality, as proven in case of Figure 4.5a. The standardised residuals analysis is displayed in Fig. 4.5b, where the least squares assumptions are met.

The red dashed lines indicate the 95 % confidence interval on future observations based upon new predictions. These boundaries are roughly within ± 1.7 MPa of the mean response, the variance of which is constant, since the confidence intervals are linear and parallel. This suggests that the quality of future predictions is constant throughout the design space. This is a key characteristic of using a rotatable experimental design. As a result, future observations shall be within ± 1.7 MPa of the predicted response throughout the design space.

Section 3.6.4.3 outlines the method for obtaining the $100(1-\alpha)$ % confidence interval for new predictions. The confidence interval is calculated by eq. 3.50, which is highly dependant on the standard error between replicates during the training phase of the model. As a result, if the observed variance between replicates SS_{PE} is high, then the prediction range increases. This range should be smaller than the total range of the response so that the model is not dominated by noise. The observed response span from ± 12 MPa to

± 20 MPa, is larger than the noise range from the mean ± 1.7 MPa. This concludes that the model is not dominated by noise, therefore the hypothesis test concerning the lack of fit can be accepted. Therefore, the model equation outlined in eq. 4.9 is significant. It accounts for 90 % of the total variance, which is ± 2 % increase due to the logarithmic transformation where 3.6 % of the ± 10 % unaccounted variance is due to lack of fit, and 6.4 % is due to the variability between replicates.

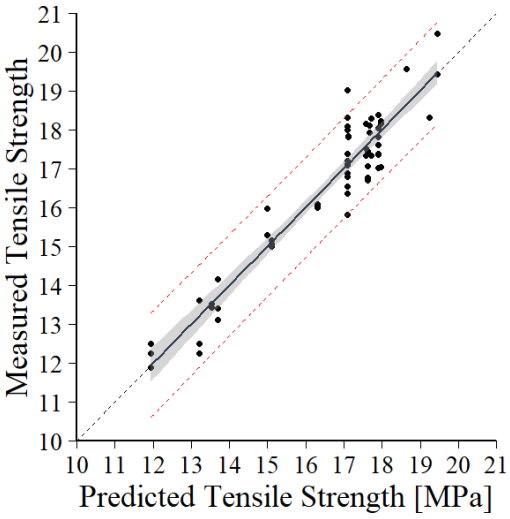

Figure 4.6: The graph displays the measured vs. predicted response of the transformed model equation provided of eq. 4.9, in conjunction with eq. 4.6. The data points correspond to the tensile test results of the second DOE iteration, which is provided in Table A.6.

4.3 Model Validation Test Results

Independent validation tests were conducted to verify the quality of the model equation provided in eq. 4.9. The results are provided in Table A.7 and plotted in Fig. 4.7. It can be seen in Fig. 4.7 that the data falls within the predicted 95 % confidence interval of the model. The mean of the observed response depicted by the solid black line approximates the predicted mean provided by the black dashed diagonal line. Also, a R^2 value of 89 % was obtained, which is nearly the same as for the training set being 90 %. These results validate the use of the model equation provided in eq. 4.9, in conjunction with eq. 4.6 given that the process variables fall within the design space provided in Table 4.3.

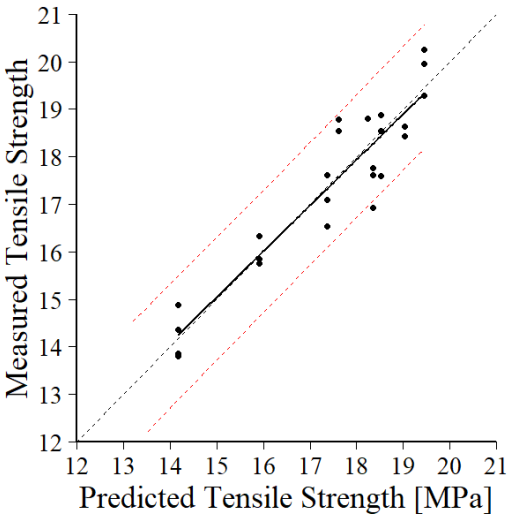

Figure 4.7: The graph displays the validation tests results of the predictive model provided in eq. 4.9. The data points and corresponding process variables are provided in Table A.7 where the 95 % confidence interval on future predictions indicated by the red dashed lines were obtained from Table A.6. The observed data falls within this region, of which the mean of the response approximates the diagonal line.

4.4 Model Implementation and Use

This section will discuss the recommendations concerning the use of the predictive model as a tool-set to support production at the industry partner. Anderson Lid Company (ALC) is concerned with producing gland seals that exceed a tensile strength of 15 MPa. The maximum achievable seal strength can be obtained by optimising the predictive model provided in eq. 4.9. This corresponds to a seal strength of 21.9 MPa, and process variables of temperature = 320 °C, pressure = 4.4 bar and dwell time = 5.5 sec. Since 4.4 bar lies on the lower pressure boundary (see Fig 4.8), additional tests outside the design space were conducted to verify the optimum pressure setting, see Table A.8.

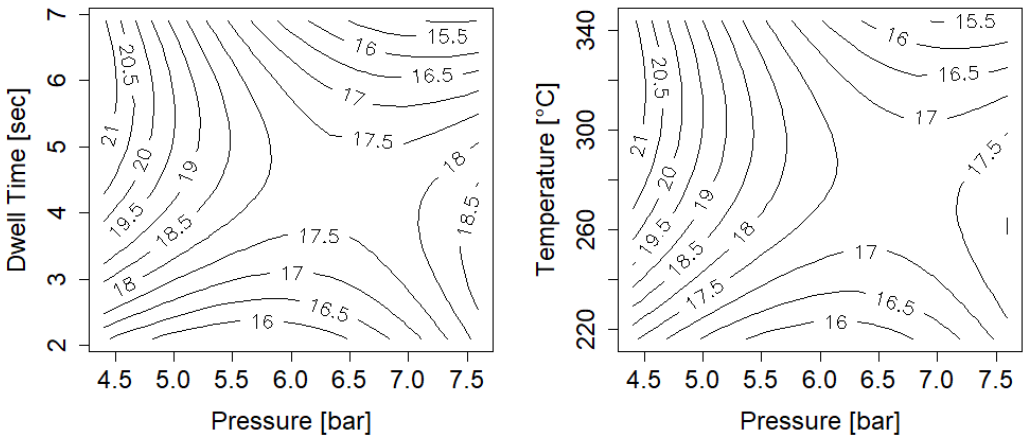

(a) Contour Plot: Dwell Time-Pressure (b) Contour Plot: Temperature-Pressure

Figure 4.8: Contour plots are based upon the model equation provided in eq. 4.9, in conjunction with eq. 4.6. Two factors are varied and the third is kept constant, e.g. Fig. 4.8a displays the resulted tensile strength based upon the pressure and dwell time at a constant temperature of 320 °C. Also, Fig. 4.8a displays the tensile strength contours based upon the temperature and pressure effects while the dwell time is constantly at 5.5 sec. High strength seals are obtained at the lower pressure values of the design space.

However, in the industry, the high strength seals are normally associated to be deep which refers to the physical depth of the seal interface into the gland fitment. From a marketing point of view, the deeper seals are less aesthetically attractive than the weaker shallow seals. Therefore it is highly desirable to establish a trade-off between aesthetics and seal strength.

Consider the above as a case study to display the possible uses for the predictive model. Since seal strength is directly proportional to seal depth being an industry rule of thumb, the shallowest seal to pass quality will most likely just exceed a seal strength of 15 MPa. Considering the noise between replicates being ± 2 MPa from the mean of the response, then the process variables corresponding to a predicted strength of 17 MPa, are a possible solution.

The lowest pressure setting in the design space will most likely produce the shallowest seal, being 4.4 bar. Then, the response surface and corresponding contour plot of the temperature and dwell time can be plotted for a constant pressure of 4.4 bar; see Fig. 4.9. The optimum conditions are clearly seen at temperature = 320 °C, dwell time = 5.5 sec and pressure = 4.4 bar, which correspond to a seal strength of 21.9 MPa.

The 17 MPa contour is highlighted in red in Fig. 4.9b. This line represents all the possible solutions of temperature and dwell time at constant 4.4 bar pressure that will yield to a seal strength of 17 MPa. If production is concerned with limiting cycle time, e.g. at 2.5 sec, then the corresponding required temperature will be 314 °C. Then, by using eq. 3.50 the 95 % confidence interval can be constructed about the 17 MPa prediction, which computes to 15.3 MPa - 18.9 MPa suggesting there is 95 % confidence that the actual seal strength will fall well within this region. Also, the lower boundary exceeds the minimum 15 MPa requirement by 0.3 MPa, which provides additional leverage outside the confidence interval in the case of outliers.

The manufacturer might also be interested in saving energy, limiting temperature at the expense of increasing the dwell time. Although not shown, a similar approach could be followed to obtain a solution as outlined above. Therefore, the manufacturer can tailor specific solutions that comply with their requirements. As a result, the constructed model is highly beneficial for the industry partner, allowing them to adapt in limited time to manufacture gland seals that comply with specific requirements.

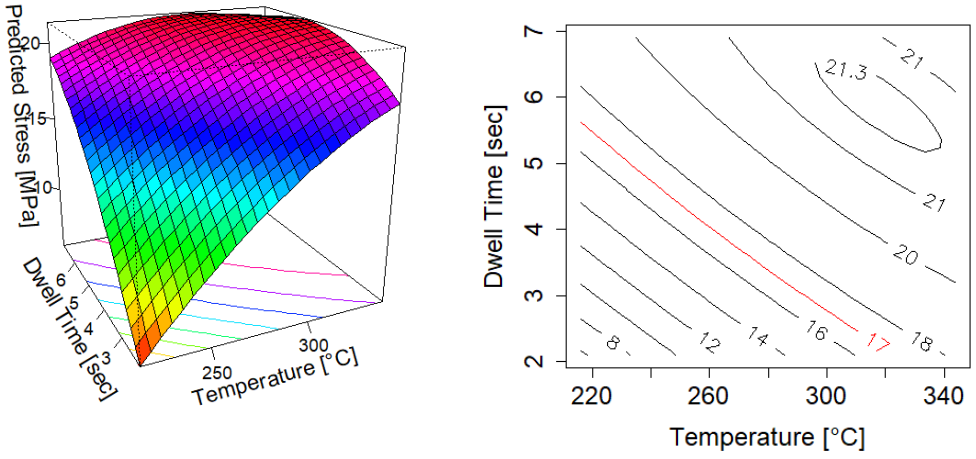

(a) Response Surface (b) Contour Plot

Figure 4.9: The consecutive graphs were produced from the model equation provided in eq. 4.9, in conjunction with eq. 4.6. The pressure is kept constant at 4.4 bar to yield the shallowest seal depth, and the temperature and dwell time effects are captured. The response surface is provided in Fig. 4.9a, and the corresponding contour plot is provided in Fig. 4.9b.

Chapter 5

Conclusions and Recommendations

5.1 Conclusions

This project set out to obtain a predictive model associated with the seal strength between film to gland fitments. The objectives were to establish the significant variables at play, obtain an adequate model equation, and finally predict the adequate process variables that will result in high strength seals, exceeding 15 MPa.

The project was limited to the most common product layout at Anderson Lid Company, being two plies of 100 µm LDPE film welded on a 2 inch hexagon gland. However, the outlined approach can be expanded to different product layouts if required. The approach followed consisted of constructing the design of experiments (DOE), producing the gland seals accordingly; cutting uniaxial tensile samples, conducting tensile tests, processing data and constructing the statistical model.

During the preliminary phase of the project, it was found that the current sample geometry being used at ALC is inadequate to provide accurate results since most failures occurred in the film rather than at the seal interface, and the uniaxial response curves did not provide clear insight into the uniaxial properties. Therefore a new sample geometry and die were designed and manufactured. These results resembled that of literature, where similar uniaxial response curves were obtained.

A data processing algorithm was written during the course of this project. The user provides a directory containing all the folders and consecutive raw uniaxial test data corresponding to the constructed DOE. The algorithm then computes and classifies the uniaxial properties of interest. The processed results are written in a CSV-file, which is later utilised for the statistical modelling. Although the tensile strength is the only uniaxial property used during modelling, the proceeding uniaxial properties were included for possible fu-

ture research projects as the industry partner might be interested in other mechanical properties affected by the process variables.

The response surface methodology approach was followed by statistical modelling. The preliminary model made use of a centre composite design. The significant variables of interest were the process variables of the sealing process. This model accounted for 80 % of the total observed variance, where the least square assumptions were violated at the extreme ends of the model predictions. As a result, the hypothesis test concluded that strong evidence existed for lack of fit.

From the preliminary study, a new DOE was constructed consisting of a central composite design in conjunction with a face-centred composite design. The new DOE which provided higher resolution has led to better approximations of the true response. Initially, an additional variable, the perimeter angle position was added to the model to reduce the unaccounted variance. However, multiple statistics tests concluded that the perimeter position is insignificant suggesting that the variance between samples are not directly related to the perimeter position of the seal interface.

A new model was constructed, which excluded the perimeter position, and only consisted of the process variables. Due to the higher resolution DOE, the accounted variance was increased to 88 % which is an 8 % improvement from the preliminary model. Additionally, a power law transformation was performed on the model equation to reduce the lack of fit. The Box-Cox analysis suggested using the natural logarithmic on the predictor variable. As a result, the transformed model accounted for about 90 % of the variance where 3.6 % of the 10 % unaccounted variance is due to lack of fit, and 6.4 % is due to the variability between replicates. Additionally, robust regression was performed to validate the coefficient estimates.

Independent validation tests were conducted to verify the use of the model. Amongst these was the predicted optimum corresponding to a seal strength of 21.9 MPa, at process variables of temperature = 320 °C, pressure = 4.4 bar and dwell time = 5.5 sec. The results obtained were within the constructed 95 % confidence interval, and the mean approximated the true response. The model accounted 89 % of the variance of the validation set. Although the model is only suited for process variables falling inside the design space, it can easily be expanded by additional trial points in the experimental design plan if required.

Additionally, the predictive model was applied in a case-study. It considered obtaining the adequate process variables that would result in seal strength exceeding 15 MPa, while limiting the process time and seal depth. The prediction quality of the model was considered during the analysis, and as a result, a predicted seal strength of 17 MPa $\pm$ 2 MPa was regarded as a possible solution. The solution of the process variables was temperature = 314 °C, dwell time = 2.5 sec and pressure = 4.4 bar. The 95 % confidence interval equated to 15.3 MPa - 18.9 MPa where the lower limit exceeds the 15 MPa requirement by 0.3 MPa, which provides additional leverage for outliers.

Although not limited to, the case-study has displayed a possible application of the predictive model where the manufacturer can tailor specific solutions to comply with changing requirements. As a result, the outlined approach and constructed model are highly beneficial for the industry partner, allowing them to adapt in limited time to manufacture gland seals that comply with specific requirements.

5.2 Recommendations

At this stage all of the objectives were met where the outlined procedures and solutions developed can be utilised for future projects. The predictive model accounted for 90 % of the total observed variance; a new project might be able to determine additional significant variables to reduce the unaccounted variance. This will reduce the standard error, which will result in even higher accuracy on the predictor variable.

Although tensile strength has been the only uniaxial tensile property modelled, additional properties could be considered. Since the processing algorithm computes all the uniaxial tensile properties, the model expansion to the remaining variables could be easily accomplished. New models can be constructed to capture the effect of the processing variables on the remaining tensile properties. Once each uniaxial property is determined, the whole uniaxial response curve can be predicted.

Also, the industry partner might be interested in looking into other failure regimes than just uniaxial tensile failure, e.g. fatigue failure might be a more appropriate representation of how the product fails in the industry than static tensile failure. The same modelling techniques could be used to adapt to new failure regimes.

Appendices

Appendix A

Tables

A.1 Design of Experiments

A.1.1 Two-Level Three Factorial Design Matrix

Table A.1: The design matrix of the two-level three factorial design is provided (Myers *et al.*, 2011, p. 86, Fig. 3.5 (b)). Each run number represents an experimental trial where the different factors are adjusted accordingly, where -1 and $+1$ refers to the lower and upper level of each factor in the design space; see Fig. 3.2. The treatment combinations refer to the geometric design space of a 2^3 design as provided in Fig. 3.2.

Run Number	Factor A	Factor B	Factor C	Treatment Combination
1	-1	-1	-1	(1)
2	$+1$	-1	-1	a
3	-1	$+1$	-1	b
4	$+1$	$+1$	-1	ab
5	-1	-1	$+1$	c
6	$+1$	-1	$+1$	ac
7	-1	$+1$	$+1$	bc
8	$+1$	$+1$	$+1$	abc

A.1.2 Box-Behnken Three Factor Design Matrix

Table A.2: The design matrix of a three factor Box-Behnken design with three centre repeats is provided (Mason *et al.*, 1989, p. 220, Table 11.5). Each run number represents an experimental trial where the different factors are adjusted accordingly; see Fig. 3.4. Run numbers 13, 14 and 15 are repeats of the centre point in Fig. 3.4.

Run Number	Factor A	B	C
1	−1	−1	0
2	−1	+1	0
3	+1	−1	0
4	+1	+1	0
5	−1	0	−1
6	−1	0	+1
7	+1	0	−1
8	+1	0	+1
9	0	−1	−1
10	0	−1	+1
11	0	+1	−1
12	0	+1	+1
13	0	0	0
14	0	0	0
15	0	0	0

A.1.3 Central Composite Three Factor Design Matrix

Table A.3: The design matrix of a three factor central composite design with three centre repeats is provided (Mason *et al.*, 1989, p. 218, Table 11.4). The design is depicted in Fig. 3.5a. Each run number represents an experimental trial where the different factors are adjusted accordingly. Run numbers 15, 16 and 17 are repeats of the centre point in Fig. 3.5a and run numbers 9 to 14 represent the axial points.

Run	Factor		
Number	A	B	C
1	−1	−1	−1
2	−1	−1	+1
3	−1	+1	−1
4	−1	+1	+1
5	+1	−1	−1
6	+1	−1	+1
7	+1	+1	−1
8	+1	+1	+1
9	−1.68	0	0
10	+1.68	0	0
11	0	−1.68	0
12	0	+1.68	0
13	0	0	−1.68
14	0	0	+1.68
15	0	0	0
16	0	0	0
17	0	0	0

A.1.4 Face-Centered Composite Three Factor Design

Table A.4: The design matrix of a three factor face-centered composite design with three centre repeats is provided (Mason *et al.*, 1989, p. 218, Table 11.4). The design is depicted in Fig. 3.5b. Each run number represents an experimental trial where the different factors are adjusted accordingly. Run numbers 15, 16 and 17 are repeats of the centre point in Fig. 3.5b and run numbers 9 to 14 represent the axial points.

Run	Factor		
Number	A	B	C
1	−1	−1	−1
2	−1	−1	+1
3	−1	+1	−1
4	−1	+1	+1
5	+1	−1	−1
6	+1	−1	+1
7	+1	+1	−1
8	+1	+1	+1
9	−1	0	0
10	+1	0	0
11	0	−1	0
12	0	+1	0
13	0	0	−1
14	0	0	+1
15	0	0	0
16	0	0	0
17	0	0	0

A.1.5 Face-Centered in Conjunction with Central Composite Three Factor Design

Table A.5: The design matrix of a three factor face-centered in conjunction with central composite design with four centre repeats is provided. Each run number represents an experimental trial where the different factors are adjusted accordingly. Run numbers 9 to 14 represent the face-centered points, run numbers 15 to 20 represent the out of face axial points and run numbers 21 to 24 are repeats of the centre point.

Run	Factor		
Number	A	B	C
1	−1	−1	−1
2	−1	−1	+1
3	−1	+1	−1
4	−1	+1	+1
5	+1	−1	−1
6	+1	−1	+1
7	+1	+1	−1
8	+1	+1	+1
9	−1	0	0
10	+1	0	0
11	0	−1	0
12	0	+1	0
13	0	0	−1
14	0	0	+1
15	−1.68	0	0
16	+1.68	0	0
17	0	−1.68	0
18	0	+1.68	0
19	0	0	−1.68
20	0	0	+1.68
21	0	0	0
22	0	0	0
23	0	0	0
24	0	0	0

A.2 Results

A.2.1 Second Phase

Table A.6: Measured uniaxial tensile results and corresponding predicted results from eq. 4.9 with 95 % confidence interval on the mean fit are provided. The DOE provided in Table A.1.5 was used to execute the experiments where the design space is given in Table 4.3. This data set is the training set of the model.

Test Number	Gland Number	Sample Number	Measured [MPa]	95 % Confidence Interval on Mean		
				Lower	Fit	Upper
1	1	Sample08	17.12055098	16.31443	17.08795	17.89814
2	1	Sample11	17.09373021	16.31443	17.08795	17.89814
3	2	Sample02	16.09141862	15.66409	16.30572	16.97364
4	2	Sample08	16.0649145	15.66409	16.30572	16.97364
5	2	Sample11	16.00167828	15.66409	16.30572	16.97364
6	3	Sample04	17.92802407	16.88509	17.66937	18.49008
7	3	Sample10	18.1169411	16.88509	17.66937	18.49008
8	4	Sample01	17.51637112	16.87051	17.56658	18.29138
9	4	Sample04	18.15493984	16.87051	17.56658	18.29138
10	4	Sample10	17.32637745	16.87051	17.56658	18.29138
11	5	Sample01	17.81190627	17.25794	17.89968	18.56529
12	5	Sample04	17.01497783	17.25794	17.89968	18.56529
13	5	Sample07	18.0388537	17.25794	17.89968	18.56529
14	5	Sample10	18.38717543	17.25794	17.89968	18.56529
15	6	Sample01	14.15759975	13.14673	13.69045	14.25666
16	6	Sample04	13.1079164	13.14673	13.69045	14.25666
17	6	Sample07	13.41038632	13.14673	13.69045	14.25666
18	7	Sample01	16.35528816	16.76009	17.09627	17.4392
19	7	Sample04	16.79331856	16.76009	17.09627	17.4392
20	7	Sample07	16.87777074	16.76009	17.09627	17.4392
21	7	Sample10	18.00189994	16.76009	17.09627	17.4392
22	8	Sample04	20.47181761	18.57825	19.45832	20.38007
23	8	Sample10	19.42685244	18.57825	19.45832	20.38007
24	9	Sample01	18.08635212	16.76009	17.09627	17.4392
25	9	Sample07	17.2049715	16.76009	17.09627	17.4392
26	10	Sample01	12.25832806	11.47667	11.94742	12.43748
27	10	Sample04	11.89043699	11.47667	11.94742	12.43748
28	10	Sample07	12.4920836	11.47667	11.94742	12.43748
29	11	Sample01	19.00991134	16.76009	17.09627	17.4392
30	11	Sample10	18.31326789	16.76009	17.09627	17.4392
31	12	Sample01	13.43676377	13.00373	13.52563	14.06848
32	12	Sample04	13.52650412	13.00373	13.52563	14.06848
33	13	Sample04	17.38442052	16.76009	17.09627	17.4392
34	13	Sample07	16.53473718	16.76009	17.09627	17.4392
35	13	Sample10	15.80642812	16.76009	17.09627	17.4392

36	14	Sample01	12.50785307	12.74337	13.21744	13.70915
37	14	Sample04	12.24930336	12.74337	13.21744	13.70915
38	14	Sample07	13.60224826	12.74337	13.21744	13.70915
39	15	Sample04	17.82773908	16.44093	17.1151	17.81691
40	15	Sample10	17.8249525	16.44093	17.1151	17.81691
41	16	Sample04	17.3369221	17.02613	17.72039	18.44296
42	16	Sample10	18.29743509	17.02613	17.72039	18.44296
43	17	Sample10	18.3080114	18.39559	19.24698	20.13778
44	18	Sample10	19.55782141	17.76551	18.63397	19.54487
45	19	Sample01	15.15186827	14.77674	15.10807	15.44683
46	19	Sample04	15.06228626	14.77674	15.10807	15.44683
47	19	Sample07	14.9978784	14.77674	15.10807	15.44683
48	20	Sample01	17.37913236	17.50117	17.89536	18.29844
49	20	Sample04	17.36355288	17.50117	17.89536	18.29844
50	20	Sample07	17.60079164	17.50117	17.89536	18.29844
51	21	Sample01	18.22884737	17.54905	17.97887	18.41923
52	21	Sample04	18.16022799	17.54905	17.97887	18.41923
53	21	Sample10	17.04664345	17.54905	17.97887	18.41923
54	22	Sample02	17.46038632	17.17312	17.6178	18.07399
55	22	Sample08	17.06776441	17.17312	17.6178	18.07399
56	23	Sample04	15.29610513	14.67435	14.9924	15.31734
57	23	Sample10	15.96475617	14.67435	14.9924	15.31734
58	24	Sample01	16.70889804	17.22735	17.62853	18.03905
59	24	Sample10	16.77222926	17.22735	17.62853	18.03905

A.2.2 Validation Set

Table A.7: Independent validations tests were performed to verify the use of the model provided in eq. 4.9, in conjunction with eq. 4.6. The process variables corresponding to the measured uniaxial tensile results, and predicted values are given. The obtained optimum conditions were included, where the temperature = 320 °C, pressure = 4.4 bar and dwell time = 5.5 sec, which corresponds to a predicted seal strength of 21.9 MPa. It can be seen that the results approximate the predicted solutions.

Gland Number	Sample Number	Measured [MPa]	Predicted [MPa]	Temp [°C]	Press [bar]	Dwell [sec]
1	1	14.884	14.164	260	4.5	3
1	4	14.368	14.164	260	4.5	3
1	7	13.864	14.164	260	4.5	3
1	10	13.797	14.164	260	4.5	3
2	1	16.34	15.91	280	4.5	3
2	4	15.84	15.91	280	4.5	3
2	7	15.748	15.91	280	4.5	3
3	1	17.613	17.361	300	4.5	3
3	4	17.092	17.361	300	4.5	3
3	10	16.528	17.361	300	4.5	3
4	1	17.594	18.517	320	4.5	3
4	4	20.355	18.517	320	4.5	3
4	7	18.539	18.517	320	4.5	3
4	10	18.869	18.517	320	4.5	3
5	6	20.397	21.03	320	4.5	4.9
5	10	19.979	21.03	320	4.5	4.9
6	5	18.63	19.034	302	5	7
6	6	18.426	19.034	302	5	7
7	4	18.545	17.606	338	5	7
7	5	18.775	17.606	338	5	7
8	4	19.961	19.452	338	5	4
8	9	20.245	19.452	338	5	4
8	11	19.285	19.452	338	5	4
9	5	17.61	18.341	302	5	4
9	6	16.926	18.341	302	5	4
9	8	17.762	18.341	302	5	4
10	2	18.799	18.228	320	5.6	5.5

A.2.3 Verify Pressure Optimum

Table A.8: Tests were performed outside the design space of Table 4.3 to show that the lower pressure boundary lies at the optimum of the model equation given in eq. 4.9. The optimum conditions were obtained and these were, temperature = 320 °C, pressure = 4.4 bar and dwell time = 5.5 sec, which corresponds to a seal strength of 21.9 MPa. The pressure value was changed respectively to 4 bar and 2.4 bar while keeping the proceeding factors at their optimum state. The results show a decrease in stress with further decrease in pressure for pressure values lower than 4.4 bar. However, from Fig. 4.8 beyond 4.4 bar, stronger seals were obtained for lower pressure settings, concluding that the pressure setting of 4.4 bar lies near the optimum.

Gland Number	Sample Number	Stress [MPa]	Temp [°C]	Press [bar]	Dwell [sec]
1	2	19.33	320	4	5.5
1	9	19.81	320	4	5.5
1	11	20.23	320	4	5.5
2	6	20.07	320	4	5.5
2	12	18.86	320	4	5.5
3	4	20.17	320	4	5.5
3	10	19.66	320	4	5.5
4	1	17.39	320	2.4	5.5
4	3	17.27	320	2.4	5.5

Appendix B

Figures

B.1 Cut Film Fitted on Gland

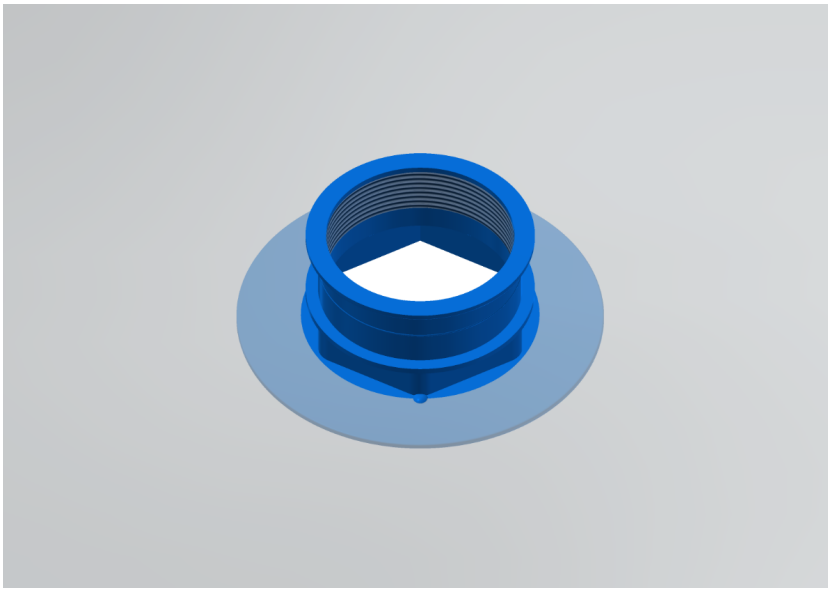

Figure B.1: Cut Film Fitted on Gland: Isometric View

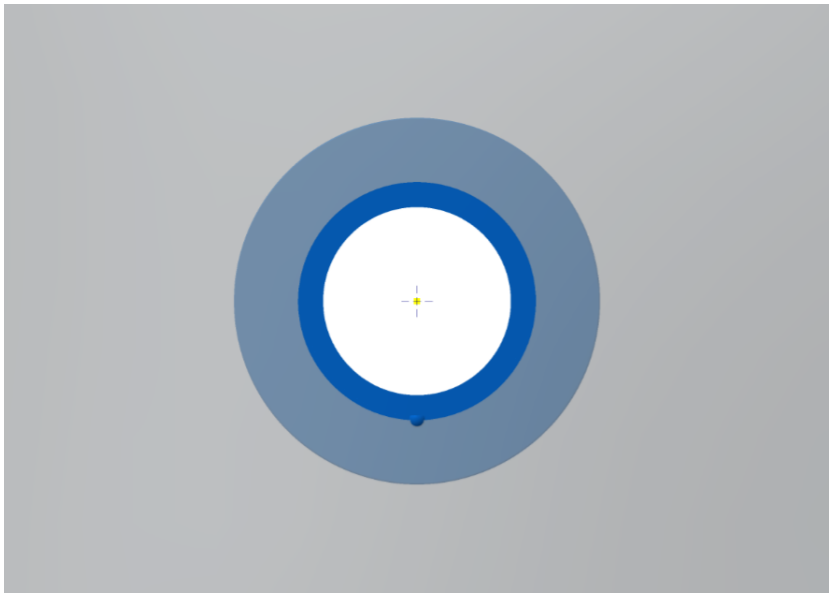

Figure B.2: Cut Film Fitted on Gland: Top View

B.2 Film to Gland Seal

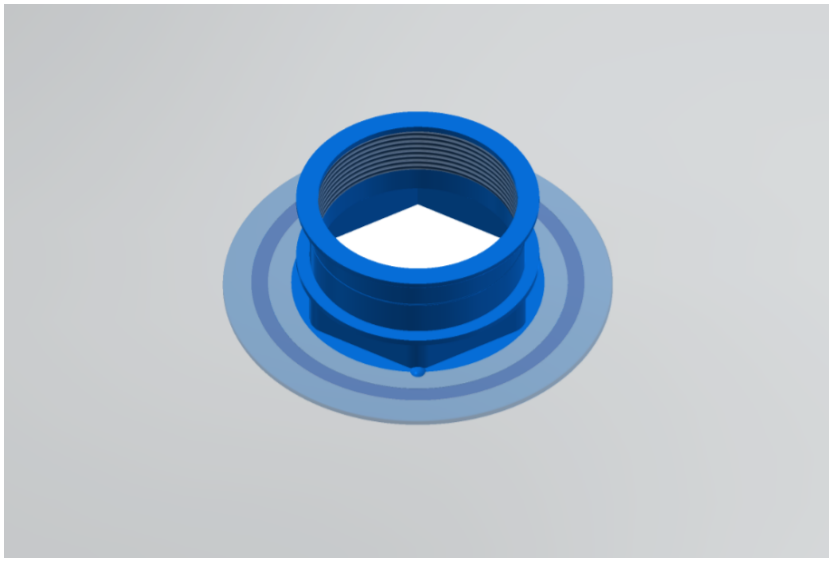

Figure B.3: Film to Gland Seal: Isometric View

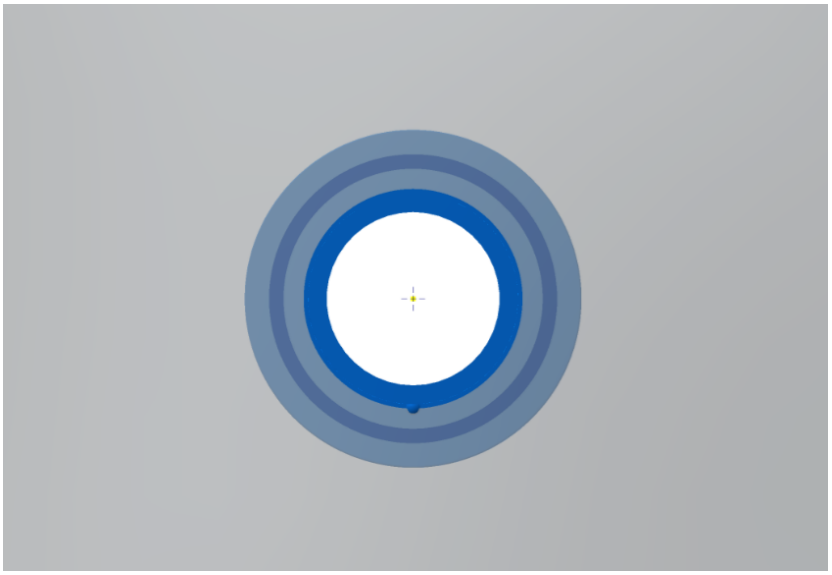

Figure B.4: Film to Gland Seal: Top View

B.3 Die and Template Placed Over Film to Gland Seal

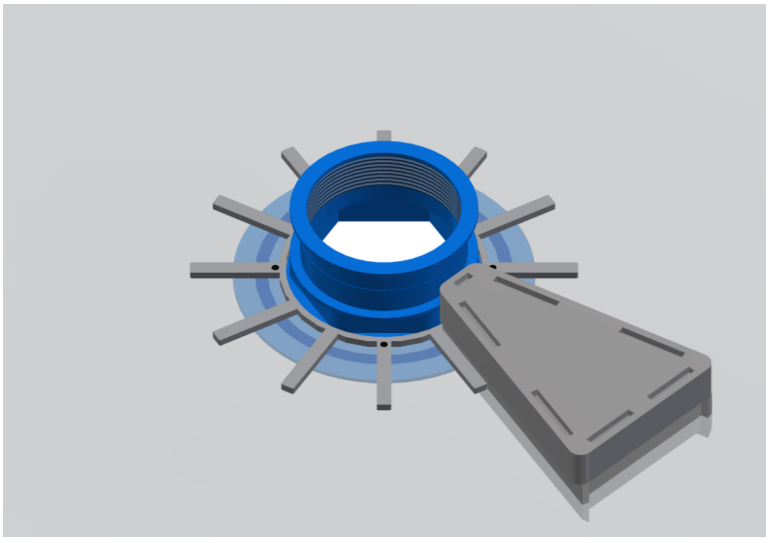

Figure B.5: Die and Template Placed Over Film to Gland Seal: Isometric View

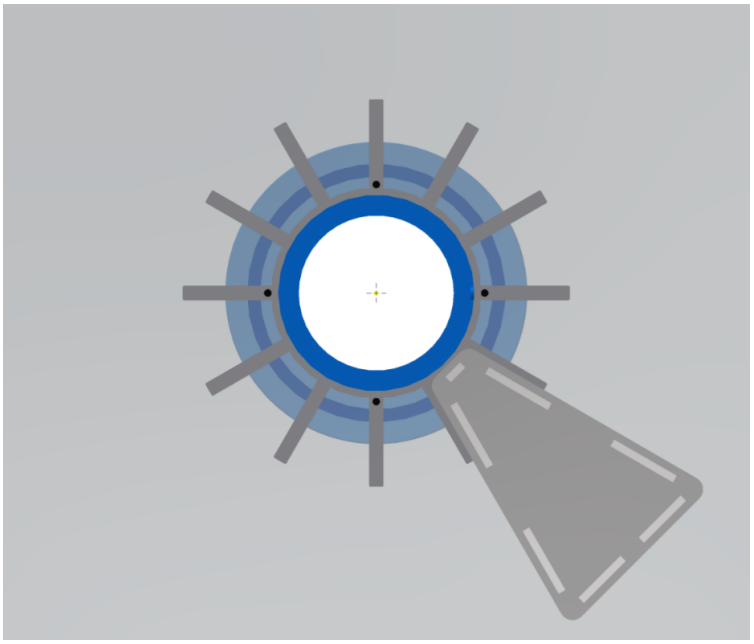

Figure B.6: Die and Template Placed Over Film to Gland Seal: Top View

B.4 Numbering Regime for Samples

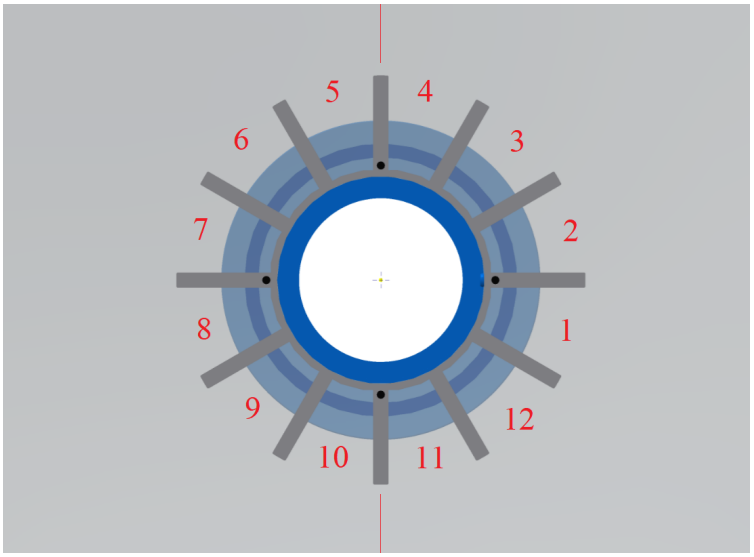

Figure B.7: Numbering Regime for Samples: Top View

B.5 Box Cox Analysis: R-studio Output

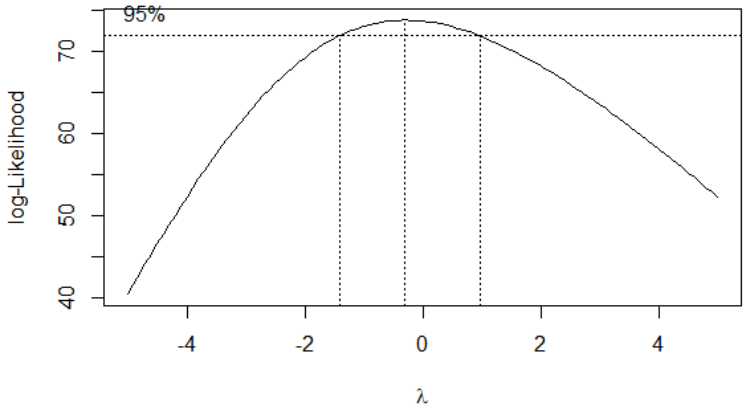

Figure B.8: Box Cox Analysis: Corresponding to model in eq. 4.5.

Appendix C

Drawings

C.1 Triangular Die Design

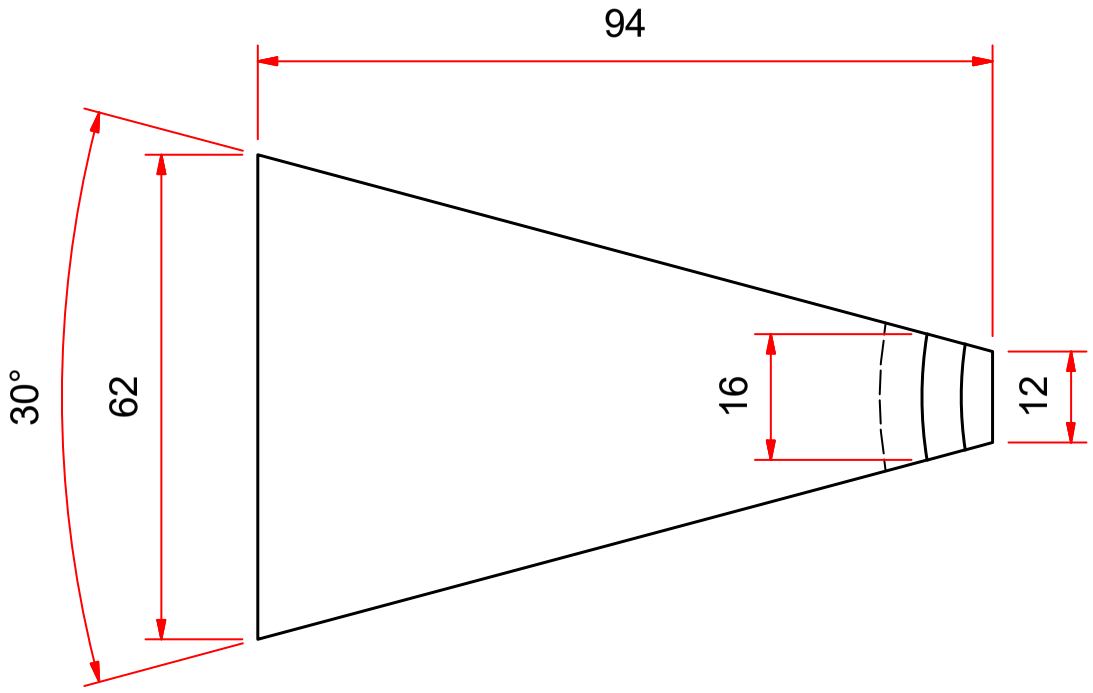

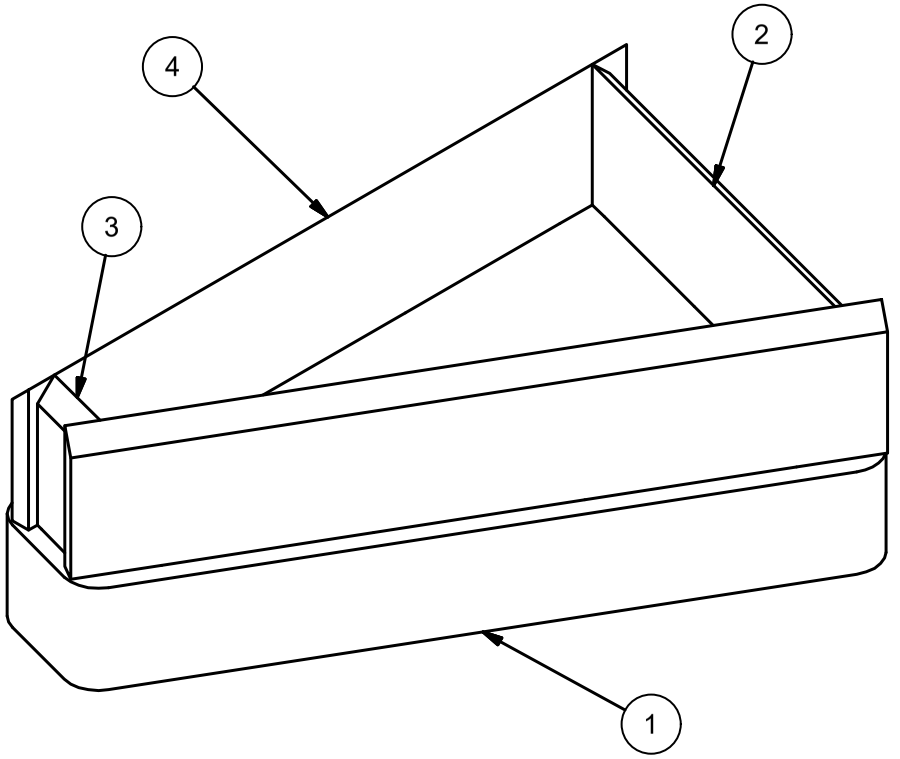

NOTE: THE DIMENSIONS ARE PROVIDED FOR THE RESULTED CUT SAMPLE, WHERE THE WIDTH OF THE SEAL INTERFACE IS 16. HOWEVER, DEPENDING ON THE SEAL PRODUCED, THIS DIMENSION MAY VARY. THEREFORE THE SEAL WIDTH SHOULD BE MEASURED BEFORE UNIAXIAL TENSILE TESTING.

ITEM	BESKRYWING	AANTAL	MATERIAAL / SPESIFIKASIES
4	SIDE BLADE	2	0505-2017
3	FRONT BLADE	1	0405-2017
2	BACK BLADE	1	0305-2017
1	BASEPLATE	1	0205-2017

UNIVERSITEIT VAN STELLENBOSCH

SKAAL OP A 4 1:1
MATE IN mm
TITEL: TRIANGULAR DYE

STUDENTE No. 17216346 | TEKENAAR I. VAN JAARSVELD | NAGESIEN | DATUM 25/07/2017 | VEL No. 1 VAN 5 VELLE | No. 0105-2017

NOTE: THE OUTER GEOMETRY OF THE BASE IS LASER CUT, WHILE THE INTERNAL SLOTS ARE WIRE CUT. THE SLOTS GO THROUGH THE ENTIRE BASEPLATE, WHICH HAS A THICKNESS OF 16.

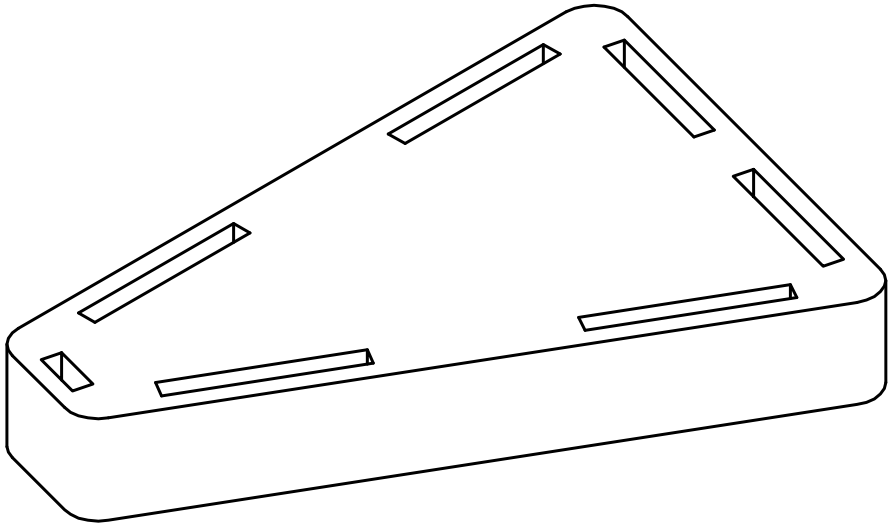

ITEM	BESKRYWING	AANTAL	MATERIAAL / SPESIFIKASIES
1	BASEPLATE	1	STAINLESS STEEL : 75 X 106 X 16

UNIVERSITEIT VAN STELLENBOSCH

STUDENTE No. 17216346	TEKENAAR I. VAN JAARSVELD	NAGESIEN	SKAAL OP A 4 1:1 MATE IN mm DATUM 25/07/2017	TITEL: BASEPLATE VEL No. 2 VAN 5 VELLE	No. 0205-2017

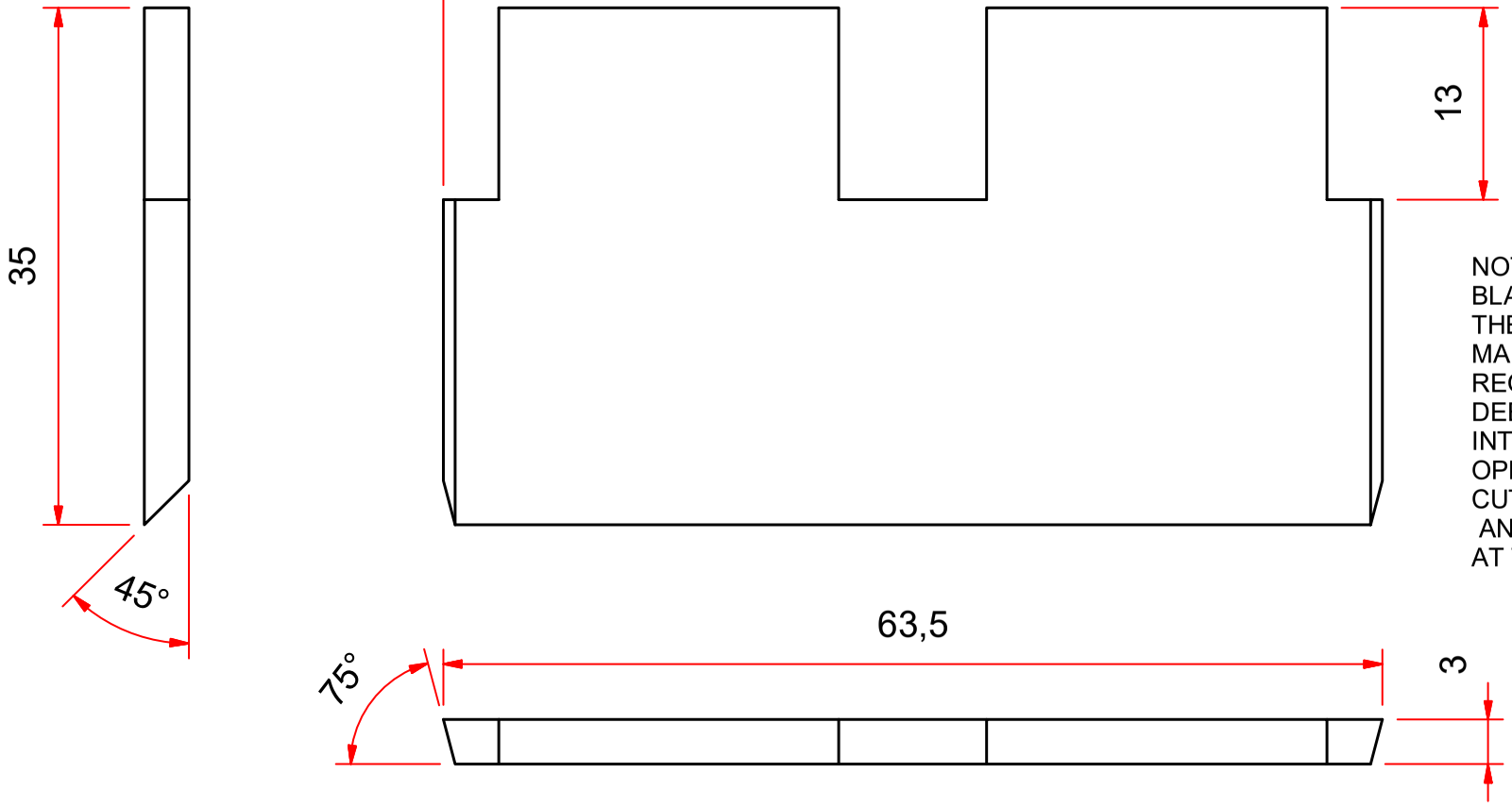

NOTE: THE 18% HSS BLADES ARE SUPPLIED, THEREFORE THE ONLY MANUFACTURING REQUIRED ARE THE 13 DEEP SLOTS THAT FIT INTO THE BASEPLATE, OPPOSITE OF THE 45° CUTTING EDGE AND THE 75° ANGLES AT THE SIDE.

UNLESS OTHERWISE STATED
TOLERANCES ± 0,1
ANGLES 1°

ITEM	BESKRYWING	AANTAL	MATERIAAL / SPESIFIKASIES
2	BACK BLADE	1	18 % HSS STEEL : 63.5 X 35 X 3

UNIVERSITEIT VAN STELLENBOSCH

SKAAL OP A4 2:1
MATE IN mm
TITEL: BACK BLADE

STUDENTE No.	TEKENAAR	NAGESIEN	DATUM	VEL No.	VAN	VELLE	No.
17216346	I. VAN JAARSVELD		25/07/2017	3	5		0305-2017

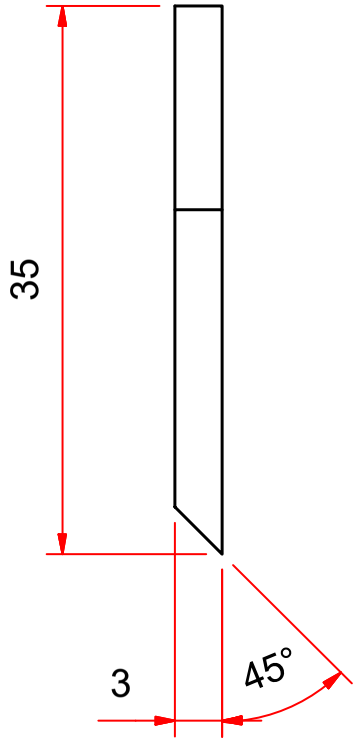

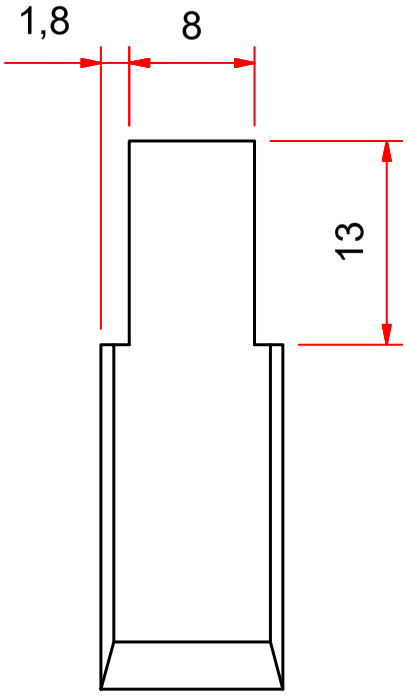

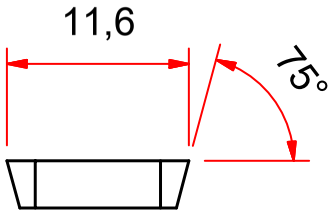

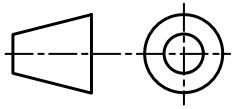

NOTE: THE 18% HSS BLADES ARE SUPPLIED, THEREFORE THE ONLY MANUFACTURING REQUIRED ARE THE 13 DEEP SLOTS THAT FIT INTO THE BASEPLATE, OPPOSITE OF THE 45° CUTTING EDGE AND THE 75° ANGLES AT THE SIDE.

UNLESS OTHERWISE STATED
TOLERANCES ± 0,1
ANGLES 1°

ITEM	BESKRYWING	AANTAL	MATERIAAL / SPESIFIKASIES
3	FRONT BLADE	1	18 % HSS STEEL : 11.6 X 35 X 3

UNIVERSITEIT VAN STELLENBOSCH

SKAAL OP A4 2:1		TITEL: FRONT BLADE	
MATE IN mm			
STUDENTE No. 17216346	TEKENAAR I. VAN JAARSVELD	NAGESIEN	DATUM 25/07/2017
VEL No. 4 VAN 5 VELLE			No. 0405-2017

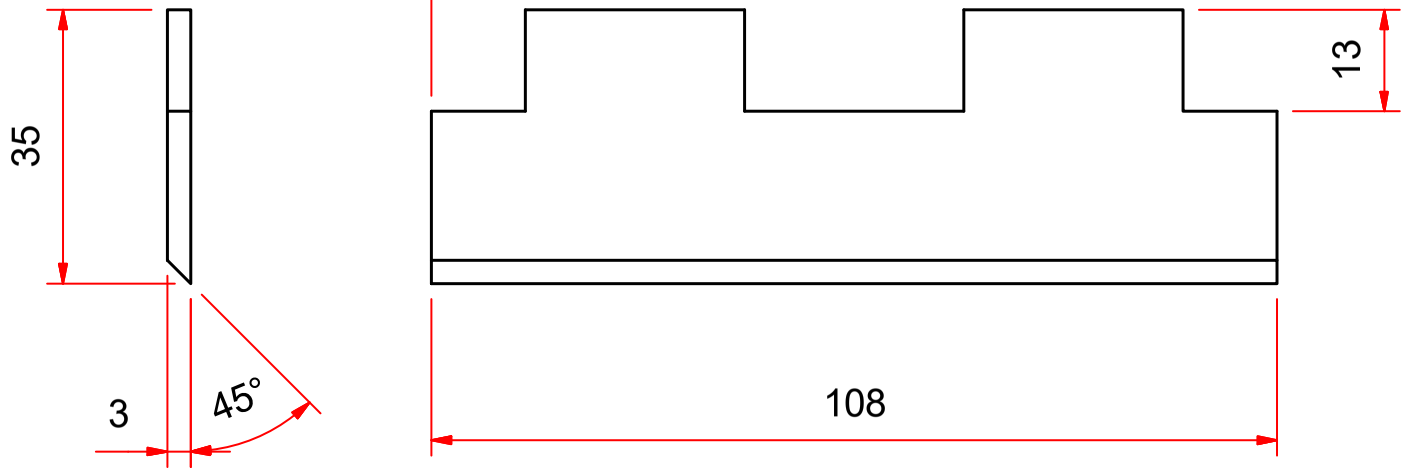

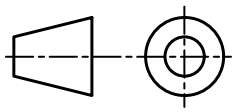

NOTE: THE 18% HSS BLADES ARE SUPPLIED, THEREFORE THE ONLY MANUFACTURING REQUIRED ARE THE 13 DEEP SLOTS THAT FIT INTO THE BASEPLATE, OPPOSITE OF THE 45° CUTTING EDGE.

UNLESS OTHERWISE STATED
TOLERANCES ± 0,1
ANGLES 1°

ITEM	BESKRYWING	AANTAL	MATERIAAL / SPESIFIKASIES
4	SIDE BLADE	2	18 % HSS STEEL : 108 X 35 X 3

UNIVERSITEIT VAN STELLENBOSCH

STUDENTE No. 17216346	TEKENAAR I. VAN JAARSVELD	NAGESIEN	SKAAL OP A 4 1:1 MATE IN mm DATUM 25/07/2017	TITEL: SIDE BLADE VEL No. 4 VAN 5 VELLE	No. 0505-2017

C.2 Grid: Die Positioning

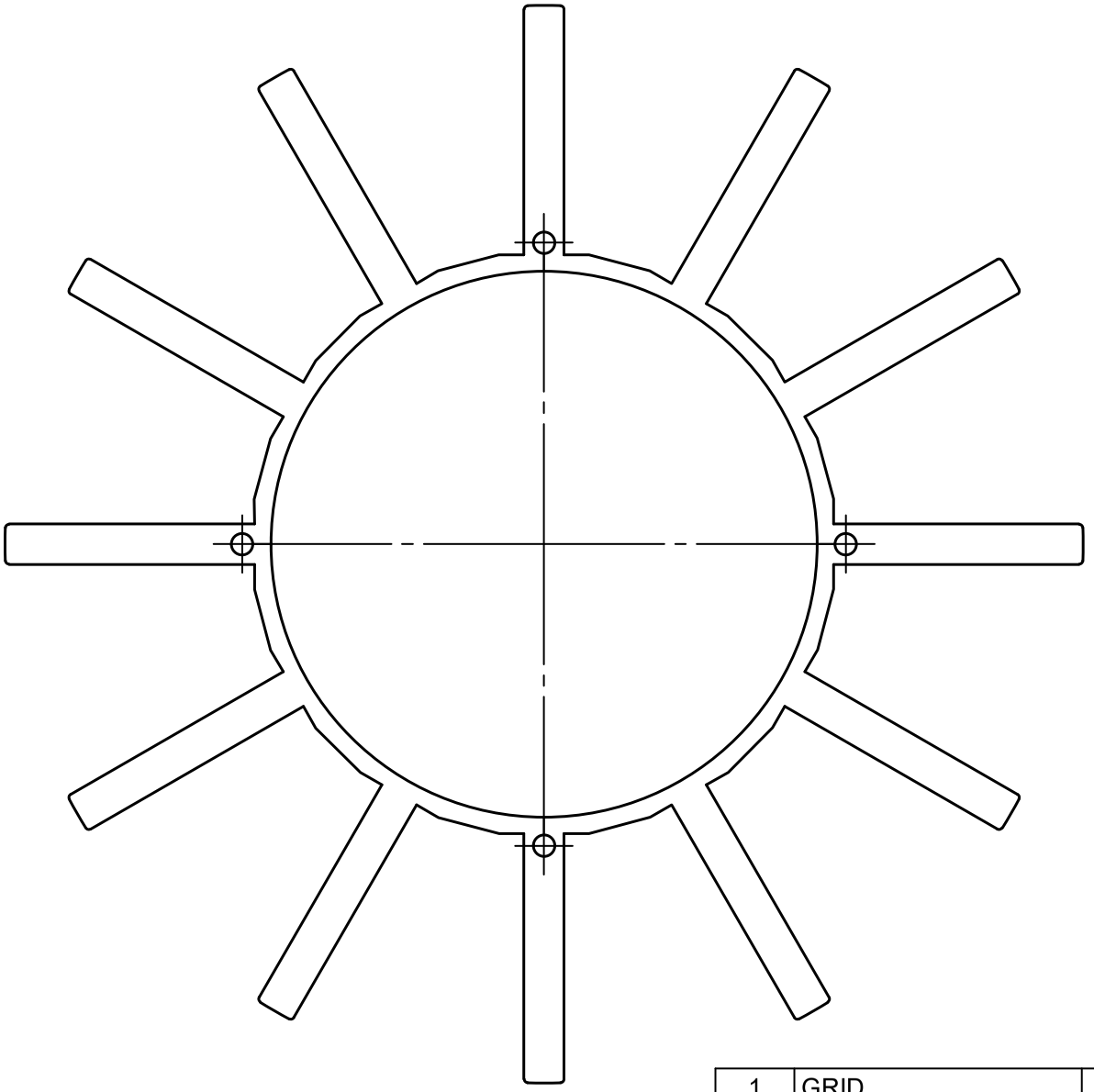

NOTE: THE GEOMETRY
IS TO BE LASER CUT

ITEM	BESKRYWING	AANTAL	MATERIAAL / SPESIFIKASIES
1	GRID	1	STAINLESS STEEL : 150 Ø X 3

UNIVERSITEIT VAN STELLENBOSCH

STUDENTE No. 17216346	TEKENAAR I. VAN JAARSVELD	NAGESIEN	SKAAL OP A4 1:1 MATE IN mm DATUM 25/07/2017	TITEL: GRID VEL No. 1 VAN 1 VELLE	No. 010105-2017

Appendix D

Data Processing Algorithm

D.1 Main Script

```
#_____________________________________________________________________
#_____________________________ Libraries _____________________________

import csv, os                  # import the csv library
import numpy as np              # import the numpy library
from Fprocessing_var import *   # imports all the functions in processing.py
from display_results import *   # import all the functions in display_results.
    py
#_____________________________________________________________________
#_____________________________ Creating a CSV file ___________________________

with open('26012017.csv','wb') as fp: # creating csv file
    a=csv.writer(fp)
    heading=[['Directory','Gland Number','Sample Number','Failure Stress [MPa]
    ','Strain at Breack [mm/mm]','Youngs Modules [MPa]',' Proportional Yield
    Stress [MPa]','Proportional Yield Strain [mm/mm]','Upper Yield [MPa]','
    Strain at Upper Yield [mm/mm]','Stiffening Point [MPa]','Strain at
    Stiffening [mm/mm]','Tangent Modulus of Second Stiffening [MPa]','
    Toughness [MJ/m^3]','Temperature [Degree Celsius]','Pressure [Bar]','Dwell
     Time [seconds]','Angular Position [Degrees]', 'Sine(Angular Position)', '
    digland_number']] # define the headings
    a.writerows(heading) # writes the aadequate headings in the file
fp.close()
#_____________________________________________________________________
#_____________________ Loop Through and Process Multiple Results _____________

directory="C:\Test\Tensile Tests\\2017_06_10\\"

for root, dirs, files in os.walk(directory):
    for file in files:
        if file.endswith(".txt") and not file.endswith("mf.txt"):
            print '_____________________________________________________________';
    print''
            print(os.path.join(os.path.join(root,file)));print ''

            path=os.path.join(os.path.join(root,file))

            with open (os.path.join(os.path.join(root,file)),'r') as fn:
                fnreader=csv.reader(fn)
                newlist=[]
                for row in fnreader:
                    if len(row)!=0:
                        newlist=newlist+[row]
```

```
35
36                 data=np.array(newlist[1:len(newlist)]).astype(np.float)
37                 filtered_data=Fprocessing_var(root,data,path,file,directory)
38             fn.close()
39
40 print "list length=";print len(newlist)
41 #_____________________________________________________________________
```

D.2 Data Processing Script

```
1 #_____________________________________________________________________
2 #_____________________________ Libraries _____________________________
3
4 from __future__ import division     # look up but it is necessary
5 import numpy as np                  #  import the numpy library
6 from matplotlib import pyplot as plt#  import pyplot from matplotlib
7 from scipy.ndimage.filters import gaussian_filter # import gaussian_filter
8
9 from inflection_point import *      # importfunction inflection_point.py
10 from ConsidereConstruction import * # importfunction ConsidereConstruction.py
11 from youngsmodulus import *         # importfunction youngsModulus.py
12 from failure import *               # importfunction failure.py
13 from secondMod import *             # importfunction secondMod.py
14 from numerical_integration import * # importfunction numerical_integration.py
15 from writeCSV import *              # importfunction writeCSV.py
16 #_____________________________________________________________________
17
18 def Fprocessing_var(root,data,path,file,directory):
19
20 #_____________________________________________________________________
21 #_____________________________ Input Variables _____________________________
22
23     disp= 1     # coluhm 1 is the displaement measured by the mts
24     load= 2     # coluhm 2 is the load measured by the mts
25     area= 3.158 # area of tensile test specimen mm^2
26     nominal_length=50 # crosshead to crosshead distance mm
27
28     data[:,1]=data[:,1]/nominal_length  # calculating strain
29     data[:,2]=data[:,2]/area            # calculating stress
30 #_____________________________________________________________________
31 #_____________________________ Filter Data _____________________________
32 #
33     filtered_data= gaussian_filter(data[:,2], 3)
34 #_____________________________________________________________________
35 #_____________________________ Numerical Derivatives _____________________________
36
37     gradient_1=[]
38     for i in range(len(filtered_data)-1): # calculating the first numerical
       derivative of the filtered data
39         gradient_1.append((filtered_data[i+1]-filtered_data[i])/(data[i+1,1]-
       data[i,1]))
40
41     filtered_gradient_1=gaussian_filter(gradient_1,3)
42 #_____________________________________________________________________
43 #_____________________ Inflection Point: Elastic Region _____________________
44
45     def_strain,def_stress=inflection_point(filtered_gradient_1,filtered_data,
       data)
46 #_____________________________________________________________________
47 #_____________________________ Considere Construction _____________________________
48
49     c_min,ii=ConsidereConstruction(filtered_data,data)
50 #_____________________________________________________________________
51 #_____________________________ Upper Yield Point _____________________________
52
```

```
53      YP=max(data[0:c_min[0][ii],2])
54      YP_int=np.where(data[0:c_min[0][ii],2]==YP); YP_int=YP_int[0][0]
55      YP_strain= data[YP_int,1]
56#_____________________________________________________________________
57#_____________________ Yield obtained by 2% method ___________________
58#_____________________ & Young's Modulus_____________________________
59
60      y_p,youngs_modulus,yield_strain,Yield2percent,tangentpoint = youngsmodulus
        (def_strain,data,filtered_data,YP_int)
61#_____________________________________________________________________
62#_____________________ Maximum Stress & Strain _______________________
63
64      strain_at_break,failure_stress,index_ms=failure(data)
65#_____________________________________________________________________
66#_____________________ Stiffening Point ______________________________
67
68      stiffening_point=min(data[c_min[0][ii+1]:index_ms,2])
69      stiff_int=np.where(data[c_min[0][ii+1]:index_ms,2]==stiffening_point);
        stiff_int=stiff_int[0][0]+len(data[0:c_min[0][ii+1],2])
70      stiff_strain=data[stiff_int,1]
71#_____________________________________________________________________
72#_____________ Tangent Modulus of Second Linear Response _____________
73
74      x_tangent,y_tangent,tangent_modulus,index_MS=secondMOd(data,
        strain_at_break,stiff_strain)
75#_____________________________________________________________________
76#_____________________ Toughness _____________________________________
77
78      toughness=numerical_integration(index_ms,data,load,disp)
79#_____________________________________________________________________
80#_____________ Creates cvs file containing the processed results_____
81
82      writeCSV(file,root,path,failure_stress,strain_at_break,youngs_modulus,
        Yield2percent,yield_strain,YP,YP_strain,stiffening_point,stiff_strain,
        tangent_modulus,toughness)
83#_____________________________________________________________________
84#_____________________ Print Results _________________________________
85
86      print "Tangentpoint=", tangentpoint, "MPa"; print ""
87      print "Youngs modulus =", youngs_modulus,"MPa";print ""
88      print "Proportional Proof Strength (Yield) =",Yield2percent, "MPa"
89      print "Perposional Proof Strain=",yield_strain, "mm/mm";print ""
90      print "Upper Yield Point =", YP, "MPA"
91      print "Strain at Upper Yield Point =", YP_strain, "mm/mm"; print ""
92      print "Tangent Modules of Second Stiffeing =",tangent_modulus, "MPa"
93      print "Stiffening Point =", stiffening_point, "MPa"
94      print "Strain at Stiffening =",stiff_strain, "mm/mm"; print ""
95      print "Stiffening Point =", stiffening_point, "MPa"
96      print "Strain at Stiffening =",stiff_strain, "mm/mm"; print ""
97#_____________________________________________________________________
98#_____________________ Plots Results _________________________________
99
100     plt.plot(x_tangent,y_tangent,'-',color='k')
101     plt.plot(data[0:YP_int,1],y_p,'-', label='Polynomial Fit')
102     plt.plot(yield_strain, Yield2percent,'o',color='k',label='Porportional
        Proof Strength')
103     plt.plot(data[0:index_MS+1,1],filtered_data[0:index_MS+1],'-',color="k",
        label="Filtered Data")
104     plt.plot(def_strain,def_stress,'o', color='b',label="Inflection Point")
105     plt.plot(stiff_strain, stiffening_point,'o',color='m',label='Stiffening
        Point')
106     plt.plot(strain_at_break,failure_stress,'o',color='c',label='Failure
        Stress')
107     plt.plot(YP_strain,YP,'h',color='r',label='Upper Yield Point')
108     plt.xlabel("Strain (mm/mm)")
109     plt.ylabel("Stress (MPa)")
```

```
    plt.legend(bbox_to_anchor=(1.05,1),loc=2,borderaxespad=0.)
    plt.show()

    return filtered_data
#_____________________________________________________________________
```

D.3 Subroutines

D.3.1 Linear Elastic Inflection Point

```
#_____________________________________________________________________
import numpy as np
from scipy.signal import argrelmax
#_____________________________________________________________________

def inflection_point(filtered_gradient_1,filtered_data,data):

    der_peaks=argrelmax(filtered_gradient_1,order=1) # calculate the index of the peaks of the first derivative filtered data
    max_der_stress=[]
    max_der_strain=[]
    der_y=[]
    der_x=[]

    for value in der_peaks:
        max_der_stress.extend(filtered_data[value]) # obtain the stress value coresponding to the peaks of the first derivatives
        max_der_strain.extend(data[value,1])        # obtain the strain value coresponding to the peaks of the first derivatives
        der_y.extend(filtered_gradient_1[value])    # obtain the first derivative y values at the peaks
        der_x.extend(data[value,1])                 # obtain the first derivative x values at the peaks

    kaa=[]
    for i in range(len(der_y)-1):
        kaa.extend(([der_y[i]-der_y[i+1]])/max(filtered_gradient_1[0:len(filtered_gradient_1)])) # obtain the drop in magnitude of the peaks of the first derivative function

    npp=len(kaa)
    search=0


    if max(kaa[0+search:npp+search])>0.1:   # establish  whether large change in the magitute drop is greater than 10 %
        temp=max(kaa[0+search:3+search])  # establish the significant peak (larger of the two) thet lead to the highest drop

        ds_int=np.where(kaa[0+search:npp+search]==temp); ds_int=ds_int[0][0]+search # obtain the index of the significant peak in Kaa
        def_stress= max_der_stress[ds_int] # obtain the stress value of the significant peak
        def_int=np.where(filtered_data==def_stress);def_int=def_int[0][0] # obtain the index of the significant peak in filtered _data
        def_strain=data[def_int,1]  # obtain the correspnding strain value of the deflection point in the leastic region S

    return def_strain,def_stress
#_____________________________________________________________________
```

D.3.2 Considère's Construction

```
#_____________________________________________________________________________
import numpy as np
from scipy.ndimage.filters import gaussian_filter
from scipy.signal import argrelmin
#_____________________________________________________________________________

def ConsidereConstruction(filtered_data,data):

    drawratio=np.add(np.array(data[:,1]),1)
    drawratio=list(drawratio)

    true_stress=np.multiply(np.array(filtered_data[:]),np.array(drawratio))

    considere_gradient=[]
    for i in range(len(true_stress)-1): # calculating the first numerical
    derivative
        considere_gradient.append((true_stress[i+1]-true_stress[i])/(drawratio
    [i+1]-drawratio[i]))

    c=np.subtract(np.array(true_stress[:-1]),np.multiply(np.array(
    considere_gradient),np.array(drawratio[:-1])))
    c_filtered=gaussian_filter(c, 2)
    c_min=argrelmin(abs(c_filtered),order=3)
    c_min=list(c_min)

    ii=0
    while data[c_min[0][ii],2]<data[c_min[0][ii+1],2]: # obrains upper yield
        ii=ii+1

    return c_min,ii
#_____________________________________________________________________________
```

D.3.3 Proportional Proof Strength and Young's Modulus

```
#_____________________________________________________________________________
import numpy as np
from scipy.interpolate import *
from scipy.fftpack import fft
from yieldpoint import *
#_____________________________________________________________________________

def youngsmodulus(def_strain,data,filtered_data,search_point):
#_____________________________________________________________________________
#_____________________ Yield obtained by 2% method ___________________________

        def find_nearest(array,value):
            idx = (np.abs(array-value)).argmin()
            return array[idx]
        f_linear=interp1d(data[0:search_point,1],data[0:search_point,2]) #
    creates a function called f_linear which is an interpolation of strain and
     stress
        p3=np.polyfit(data[0:search_point,1],data[0:search_point,2],13) #
    obtaines the coeficients of the 13th order polynomial
        y_p=np.polyval(p3,data[0:search_point,1]) # calculates the respective
    y-values (stress) for the respective strain values
    #_____________________________________________________________________
    #_____________________ Young's Modulus_____________________________

        nearest_def_strain=find_nearest(data[:,1],def_strain) # the stress
    value at which the first increment of youngs modules is calculated
```

```
        index_def=np.where(data[:,1]==nearest_def_strain);index_def=index_def
    [0][0]
        tangentpoint=filtered_data[index_def]
        ys_list=yieldpoint(filtered_data,data,tangentpoint,search_point,
    index_def)
        ys_array=np.asarray(ys_list) # finds the maximum  solution point

        youngs_modulus=ys_array[1]
    #_____________________________________________________________________

        yield_strain=ys_array[0][0]
        Yield2percent=np.asarray(f_linear(yield_strain))

        return y_p,youngs_modulus,yield_strain,Yield2percent,tangentpoint
#_____________________________________________________________________
```

D.3.4 Yield Point

```
#_____________________________________________________________________
from __future__ import division      # look up but it is necessary
import numpy as np                   #  import the numpy library
from matplotlib import pyplot as plt#  import pyplot from matplotlib
from scipy.interpolate import *
#_____________________________________________________________________

def yieldpoint(filtered_data,data,tangentpoint,search_point,index_def):

    def find_nearest(array,value):
        idx = (np.abs(array-value)).argmin()
        return array[idx]

    p3=np.polyfit(data[0:search_point,1],filtered_data[0:search_point],13) #
    obtaines the coeficients of the 13th order polynomial
    grad_int=index_def
    m=(filtered_data[grad_int+1]-filtered_data[grad_int-1])/(data[grad_int
    +1,1]-data[grad_int-1,1]) # the gradient or Young's Modulus is calculated
    about the 8 MPA indicated value
    youngs_modulus=m

    c=filtered_data[grad_int]-data[grad_int,1]*m # the intercept of the
    tangent line, which goes through the point where youngs's modulus is
    calculated, is required for the 2% yield point calculation
    y_2=m*(data[grad_int:grad_int+20,1]-0.02)+c  # this is the concstruction
    line to obtain the 2% yield point
    plt.plot(data[grad_int:grad_int+20,1],y_2,label='2 % Construction Line') #
     the construction line is plotted

    p3[-1]=p3[-1]-c+0.02*m  # solving where the interpolated equation and
    construction line crosses
    p3[-2]=p3[-2]-m         # solving where the interpolated equation and
    construction line crosses
    roots=np.roots(p3)      # obtaines the roots, which is the desired
    solution of where the interpolated function and construction line crosses
    #print "roots=",roots

    yield_strain_array=[]   # creates a emty array
    for value in roots:     # loops through the roots, check for the positive
    real value which becomes the sollution
        if value.imag==0 and value.real>0:

            yield_strain_array.extend([value.real])


    temp=yield_strain_array<data[search_point,1]  # look for the solution of
    points in the region of interest
```

```
    yield_strain_np_array=np.asarray(yield_strain_array) # change array type
    to numpy array type

    return yield_strain_np_array[temp], youngs_modulus
#_____________________________________________________________________________
```

D.3.5 Failure Stress and Strain

```
#_____________________________________________________________________________

def failure(data):
        tot_index=len(data[:,2])-1
        index_ms=tot_index

        while abs(data[index_ms-10,2])/abs(data[index_ms,2])>1:
            while abs(data[index_ms-1,2])/abs(data[index_ms,2])>1:   #
    determines when there is a significant change in the stress value
                index_ms=index_ms-1
            index_ms=index_ms-5

        failure_stress=data[index_ms,2]
        strain_at_break=data[index_ms,1]

        return strain_at_break,failure_stress,index_ms
#_____________________________________________________________________________
```

D.3.6 Second Modulus: Cold Drawing

```
#_____________________________________________________________________________
from find_nearest import *
import numpy as np
#_____________________________________________________________________________

def secondMOd(data,strain_at_break,stiff_strain):

    temp_strain=find_nearest(data[:,1],strain_at_break)
    index_MS=np.where(data[:,1]==temp_strain);index_MS=index_MS[0][0]
    st_int=np.where(data[:,1]==stiff_strain);st_int=st_int[0][0]

    tangent_modulus=tangent_modulus=(data[index_MS,2]-data[st_int,2])/(data[
    index_MS,1]-data[st_int,1])

    c_tangent= data[st_int,2]-tangent_modulus*data[st_int,1]
    x_tangent=data[st_int:index_MS,1]
    y_tangent=tangent_modulus*data[st_int:index_MS,1]+c_tangent

    return x_tangent,y_tangent,tangent_modulus,index_MS
#_____________________________________________________________________________
```

D.3.7 Toughness

```
#_____________________________________________________________________________

def numerical_integration(index_ms,data,load,disp): # this function integrates
     up until the breakpoint
    toughness=0                         # before integration the toughness is
    set to 0
    for num in range (0,index_ms):      # loops until break point
        toughness=toughness+ 0.5*(data[num+1,load]+data[num,load])*(data[num
    +1,disp]-data[num,disp]) # numerical integration
    print "Toughness (Deformation Energy) =", toughness, "MJ/m^3";print ""  #
    prints the youngs toughness
    return toughness

```

```
    ######## Example of integration that works: cricle where r=2 ########
    #k=5                                                                 #
    #x=np.linspace(-2.0,2.0,k)                                          #
    #y=np.zeros((1,2000))                                               #
    #y=np.sqrt(4-x**2)                                                  #
    #area=0                                                             #
    #for num in range (0,k-1):                                          #
    #    area=area+ 0.5*(y[num+1]+y[num])*(x[num+1]-x[num])             #
    ######################################################################
#_____________________________________________________________________
```

D.3.8 Write Results in CSV-File

```
#_____________________________________________________________________
import numpy as np
import csv, os
import math
from design_m import *
#_____________________________________________________________________

def writeCSV(file,root,path,failure_stress,strain_at_break,youngs_modulus,
    Yield2percent,yield_strain,YP,YP_strain,stiffening_point,stiff_strain,
    tangent_modulus,toughness):

    gland_number_value=root[-2:]
    temp, press, dt = design_m(gland_number_value)

    sample_number=file.strip('.txt') # stripthe .txt string from the full
    string
    sam_number=np.array(['Sample01','Sample02','Sample03','Sample04','Sample05
    ','Sample06','Sample07','Sample08','Sample09','Sample10','Sample11','
    Sample12'])
    per_angle=[345,15,45,75,105,135,165,195,225,255,285,315]
    int_ang=np.where(sam_number==str(sample_number))
    int_ang=int_ang[0][0]

    angular_position=per_angle[int_ang]
    sine_angular_position=math.sin(math.pi*per_angle[int_ang]/180)

    folder_path = os.path.dirname(path)
    path,folder_name = os.path.split(folder_path)

    dict_gland={'01':'Gland01','02':'Gland02','03':'Gland03','04':'Gland04','
    05':'Gland05','06':'Gland06','07':'Gland07','08':'Gland08','09':'Gland09',
    '10':'Gland10','11':'Gland11','12':'Gland12', '13':'Gland13', '14':'
    Gland14', '15':'Gland15', '16': 'Gland16', '17':'Gland17', '18':'Gland18',
    '19':'Gland19', '20':'Gland20', '21': 'Gland21', '22':'Gland22', '23':'
    Gland23', '24':'Gland24'}

    gland_number=folder_name
    digland_number=dict_gland[folder_name]

    lst=[path,gland_number,sample_number,failure_stress,strain_at_break,
    youngs_modulus,Yield2percent,yield_strain,YP,YP_strain,stiffening_point,
    stiff_strain,tangent_modulus,toughness,temp, press, dt, angular_position,
    sine_angular_position,digland_number] # list of results desired to be
    imported to csv file

    with open('26012017.csv','ab') as fp:
        a=csv.writer(fp, delimiter=',')
        a.writerows([lst])
    fp.close()
#_____________________________________________________________________
```

D.3.9 Design Matrix

```
#_____________________________________________________________________________
import math

def design_m(value):

    gland_number=value
    mid_temp=280
    mid_press=6
    mid_dt=4.5

    temp_range=320-240
    press_range=7-5
    dt_range=6-3

    star_temp=63.8179
    star_press=1.595448
    star_dt=2.393172
#_____________________________________________________________________________
#_____________ Center Composite Design + Face Centered Deign _______________

    a=[-1,1,1,1,-1,-1,0,1,0,-1,0,-math.sqrt(2),0,0,0,math.sqrt(2)
    ,0,0,-1,1,0,0,0,0]
    b=[1,1,1,-1,-1,1,0,-1,0,-1,0,0,0,0,0,0,-math.sqrt(2),math.sqrt(2)
    ,0,0,-1,1,0,0]
    c=[1,1,-1,-1,1,-1,0,1,0,-1,0,0,0,-math.sqrt(2),math.sqrt(2)
    ,0,0,0,0.8,0.8,0.8,0.8,-1,1]

    if a[int(gland_number)-1]==-1:
        A=mid_temp-0.5*temp_range

    elif a[int(gland_number)-1]==0:
        A=mid_temp

    elif a[int(gland_number)-1]==1:
        A=mid_temp+0.5* temp_range

    elif a[int(gland_number)-1]==-math.sqrt(2):
        A=mid_temp-star_temp

    elif a[int(gland_number)-1]==math.sqrt(2):
        A=mid_temp+star_temp


    if b[int(gland_number)-1]==-1:
        B=mid_press-0.5*press_range

    elif b[int(gland_number)-1]==0:
        B=mid_press

    elif b[int(gland_number)-1]==1:
        B=mid_press+0.5* press_range

    elif b[int(gland_number)-1]==-math.sqrt(2):
        B=mid_press-star_press

    elif b[int(gland_number)-1]==math.sqrt(2):
        B=mid_press+star_press


    if c[int(gland_number)-1]==-1:
        C=mid_dt-0.5*dt_range

    elif c[int(gland_number)-1]==0:
        C=mid_dt
```

```
62
63      elif c[int(gland_number)-1]==1:
64          C=mid_dt+0.5* dt_range
65
66      elif c[int(gland_number)-1]==-math.sqrt(2):
67          C=mid_dt-star_dt
68
69      elif c[int(gland_number)-1]==math.sqrt(2):
70          C=mid_dt+star_dt
71
72      elif c[int(gland_number)-1]==0.8:
73          C=4.5
74
75      return(A,B,C)
76#_____________________________________________________________________________
```

List of References

Annadurai, G. and Sheeja, R. (1998). Use of box-behnken design of experiments for the adsorption of verofix red using biopolymer. *Bioprocess and Biosystems Engineering*, vol. 18, no. 6, pp. 463–466.

Aslan, N. and Cebeci, Y. (2007). Application of box–behnken design and response surface methodology for modeling of some turkish coals. *Fuel*, vol. 86, no. 1, pp. 90–97.

Chiang, R. and Flory, P. (1961). Equilibrium between crystalline and amorphous phases in polyethylene1. *Journal of the American Chemical Society*, vol. 83, no. 13, pp. 2857–2862.

Jardret, V. and Morel, P. (2003). Viscoelastic effects on the scratch resistance of polymers: relationship between mechanical properties and scratch properties at various temperatures. *Progress in organic coatings*, vol. 48, no. 2, pp. 322–331.

Kretschmer, W.P., Meetsma, A., Hessen, B., Schmalz, T., Qayyum, S. and Kempe, R. (2006). Reversible chain transfer between organoyttrium cations and aluminum: Synthesis of aluminum-terminated polyethylene with extremely narrow molecular-weight distribution. *Chemistry–A European Journal*, vol. 12, no. 35, pp. 8969–8978.

Landel, R. and Nielsen, L. (1993). *Mechanical Properties of Polymers and Composites, Second Edition*. Mechanical Engineering. Taylor & Francis. ISBN 9780824789640.
Available at: `https://books.google.co.za/books?id=Q-d50ibrGiUC`

Mason, R., Gunst, R. and Hess, J. (1989). *Statistical design and analysis of experiments: with applications to engineering and science*. Wiley series in probability and mathematical statistics: Applied probability and statistics. Wiley. ISBN 9780471853640.
Available at: `https://books.google.co.za/books?id=gvVQAAAAMAAJ`

Myers, R., Montgomery, D. and Anderson-Cook, C. (2011). *Response Surface Methodology: Process and Product Optimization Using Designed Experiments*. Wiley Series in Probability and Statistics. Wiley. ISBN 9781118210475.
Available at: `https://books.google.co.za/books?id=F6MJeRe2POUC`

Raumann, G. and Saunders, D. (1961). The anisotropy of young's modulus in drawn polyethylene. *Proceedings of the Physical Society*, vol. 77, no. 5, p. 1028.

Richeton, J., Ahzi, S., Vecchio, K., Jiang, F. and Adharapurapu, R. (2006). Influence of temperature and strain rate on the mechanical behavior of three amorphous polymers: characterization and modeling of the compressive yield stress. *International journal of solids and structures*, vol. 43, no. 7, pp. 2318–2335.

SASOL (2017). Chemicals: Polymers. `http://www.sasol.com/products/chemicals`. Accessed: 25-10-2017.

Schwarz, G. *et al.* (1978). Estimating the dimension of a model. *The annals of statistics*, vol. 6, no. 2, pp. 461–464.

Seki, Y., Seyhan, S. and Yurdakoc, M. (2006). Removal of boron from aqueous solution by adsorption on al 2 o 3 based materials using full factorial design. *Journal of hazardous materials*, vol. 138, no. 1, pp. 60–66.

Siracusa, V. (2012). Food Packaging Permeability Behaviour : A Report. vol. 2012, no. i.

Sperling, L.H. (2005). *Introduction to physical polymer science*. John Wiley & Sons.

Tashiro, K., Kobayashi, M. and Tadokoro, H. (1978). Calculation of three-dimensional elastic constants of polymer crystals. 2. application to orthorhombic polyethylene and poly (vinyl alcohol). *Macromolecules*, vol. 11, no. 5, pp. 914–918.

Terezo, A. and Pereira, E. (2000). Fractional factorial design applied to investigate properties of ti/iro 2–nb 2 o 5 electrodes. *Electrochimica Acta*, vol. 45, no. 25, pp. 4351–4358.

Vicente, G., Coteron, A., Martinez, M. and Aracil, J. (1998). Application of the factorial design of experiments and response surface methodology to optimize biodiesel production. *Industrial crops and products*, vol. 8, no. 1, pp. 29–35.

Ward, I.M. and Hadley, D.W. (1993). *An introduction to the mechanical properties of solid polymers*. John Wiley & Sons Ltd.; John Wiley & Sons, Inc.